

Argand-plane mappings induced by complex scalar wavefields

A thesis submitted for the degree of

Doctor of Philosophy

by

Freda Werdiger

B.Sc.(Hons), Monash University

School of Physics and Astronomy

Monash University

Australia

August 25, 2016

Contents

Abstract	vii
Acknowledgements	ix
Declaration	ix
1 Introduction	1
1.1 The field concept in physics	1
1.2 Mathematics as a language for quantitatively studying fields	7
1.3 Argand-plane representation of complex numbers	12
2 Argand-plane representation of optical vortices in a two-dimensional complex scalar wavefield	19
2.1 Introduction and background theory	19
2.2 Duality between phase vortices and Argand-plane caustics	27
3 A study of Argand-plane vorticity singularities using optical speckle	39
3.1 Introduction and background theory	39
3.2 Argand-plane vorticity singularities in complex scalar optical fields: An experimental study using optical speckle	46
4 A study of generalised Cornu spirals using hard x-rays	63
4.1 Introduction and background theory	64
4.2 Generalised Cornu spirals: An experimental study using hard x-rays	75
5 Future work	91
6 Conclusion	93

Copyright notice

© Freda Werdiger (2016). Except as provided in the Copyright Act 1968, this thesis may not be reproduced in any form without written permission of the author.

Abstract

In this thesis, an analysis of two-dimensional complex scalar wavefields associated with electromagnetic radiation is presented. The particular tool of analysis is the Argand-plane mappings that are induced by such wavefields. The analysis is carried out over three distinct but interconnected studies, each accompanied by a published body of work. The first study involves the simulation of a visible-light speckle field that is littered with vortices. The Argand-plane mappings induced by this field reveal caustic-like structures that are singularities of the mapping. It is found that these singularities, called vorticity singularities, are induced by lines of zero vorticity in the physical wavefield, and their connection to vortices is investigated. The second body of work contains an experimental realisation of vorticity singularities, done by generating a speckle field using visible light. Various vorticity singularities - the fold, cusp, and elliptic umbilic - are reconstructed using experimental data, and the lines of zero vorticity that induce them are observed.

The third study moves from the domain of visible light into x-ray radiation. Here, the Argand-plane is used as a tool for investigating x-ray diffraction. Three objects, having been illuminated by hard x-rays, are imaged using propagation-based phase contrast imaging; a straight edge, cylinder and a sphere embedded within a cylinder. The full information of the propagated wavefield is recovered using a combination of phase retrieval and virtual optics. The associated Argand-plane mappings reveal structures known as generalised Cornu spirals that are induced by the diffraction of the incident radiation around the object in question. Each object is associated with a particular generalised Cornu spiral that is explained using the Geometrical Theory of Diffraction.

The body of work constituting the present thesis indicates that the Argand plane is an interesting tool for the analysis of the complex scalar wavefield associated with optical

fields, possessing features that are singularities of the mapping to the Argand plane that can be used to study various phenomena in the physical field. The applications for Argand-plane analysis may be numerous, going beyond the context of optical fields.

Acknowledgements

I would like to acknowledge the help and support of my family and friends during my candidature. The support and encouragement of my supervisors, Professor David M. Paganin and Dr. Marcus J. Kitchen, and other members of the school, Mrs Jean Pettigrew in particular, has been invaluable in allowing my candidature to come to completion. Finally, I wish to acknowledge funding from the Dean's Scholarship scheme for financial support during this time.

This thesis is dedicated to E.

Declaration

I hereby declare that this thesis contains no material which has been accepted for the award of any other degree or diploma at any university or equivalent institution and that, to the best of my knowledge and belief, this thesis contains no material previously published or written by another person, except where due reference is made in the text of the thesis.

This thesis includes three original papers published in peer reviewed journals. The core theme of the thesis is Argand-plane mappings induced by optical fields. The ideas, development and writing up of all the papers in the thesis were the principal responsibility of myself, the student, working within the School of Physics and Astronomy under the supervision of Professor David M. Paganin and co-supervision of Dr. Marcus J. Kitchen.

(The inclusion of co-authors reflects the fact that the work came from active collaboration between researchers and acknowledges input into team-based research.)

In the case of Chapters 2-4 my contribution to the work involved the following:
The majority of all analytic work and computer simulations and, in all cases, writing the publications. The collection of experimental data for Chapter 3 was done with my direct involvement and my being responsible for data analysis and image processing. For data used in Chapter 4, I was not present for data collection but oversaw the experimental particulars and was responsible for data analysis and image processing.

Thesis Chapter	Publication Title	Status <i>(published, in press, accepted or returned for revision)</i>	Nature and % of student contribution	Co-author name(s) Nature and % of Co-author's contribution*	Co-author(s), Monash student Y/N*
2	Duality between phase vortices and Argand-plane caustics	Published	90% of work incl. theoretical and computational work and writing of paper.	Prof. David M. Paganin; contributions to theoretical, analytical and computational work, and writing. Dr. Marcus J. Kitchen; contributions to theoretical work, computational work and writing Dr. Helen M. L.. Faulkner; contributions to theoretical work.	N
3	Argand-plane vorticity singularities in complex scalar optical fields: An experimental study	Published	90% of work incl. data collection and analysis, image processing, theoretical work and writing of paper.	Prof. David M. Paganin; contributions to theoretical, analytical and computational work and writing Dr. Alexis I. Bishop; contributions to experimental work Dr. Marcus J. Kitchen; contributions to data	N

	using optical speckle			analysis, theoretical work and writing	
4	Generalised Cornu spirals: An experimental study using hard x-rays	Published	90% of work incl. theoretical and analytical work, image processing and data analysis.	Prof. David M. Paganin; contributions to theory, analytical, computational work and writing Dr. Marcus J. Kitchen; contributions to experimental work, data analysis, theory and writing.	N

**If no co-authors, leave fields blank*

I have / have not renumbered sections of submitted or published papers in order to generate a consistent presentation within the thesis.

Student signature:



Date: 09/05/2016

The undersigned hereby certify that the above declaration correctly reflects the nature and extent of the student's and co-authors' contributions to this work. In instances where I am not the responsible author I have consulted with the responsible author to agree on the respective contributions of the authors.

Main Supervisor signature:



Date: 9/05/2016

Chapter 1

Introduction

In this thesis, the complex scalar representation of free electromagnetic fields is studied, with particular attention being paid to the Argand-plane mapping induced by such wavefields. The Argand plane, also known as the complex plane, presents itself as an interesting environment with which to study aspects of electromagnetic fields, as exemplified by the work featured in the following chapters. Before presenting the main body of work, it is necessary to lay down some background information of the theory of fields. This includes the history of its development, some features of fields that are key to this thesis and, briefly, the emergence of quantum field theory. Further, it is necessary to provide the mathematical underpinning of classical field theory, as it is evoked throughout this work. Finally, an introduction to the general theory of mappings, and Argand-plane mappings in particular, is given.

1.1 The field concept in physics

1.1.1 History and development of the field concept

The first recorded use of the word ‘field’ as a technical term in physics was by Thomson (1851). He defined a ‘field of magnetic force’ as any space for which every point within it possesses a finite magnetic force. The general idea of a field is that, when present, a body has an area of influence around it and at a distance from it. This technical definition,

however, has been debated and discussed among philosophers and scientists long before the mid-nineteenth century.

An idea that had early philosophers in almost total agreement was that there existed a principle that excluded the possibility of ‘action from a distance’. That is, action can only be transmitted between bodies through contact. Of course, various physical phenomena, such as a magnet causing a distant piece of iron to move, begs further analysis. Can contact be restored through some transmission across the intervening space between the magnet and the piece of iron? Gilbert (1600) referred to this transmission as an ‘orb of virtue’ that expands in all directions. The motion of celestial bodies and the ebb and flow of tides are also phenomena indicating causal action at a distance. Newton’s theory of gravitation, which links mass, force and acceleration, is arguably a field theory in that it provides a function that is defined for every point in space surrounding a gravitating body, prescribing how a second body would behave. However, by Newton’s own assertion (Newton, 1962), his theory considers forces mathematically and does not define the manner by which the force is exerted; Newton’s theory of gravitation is a calculation device which does not provide an explanation that excludes action from a distance. Faraday (1852), in his landmark work ‘On the physical character of the lines of magnetic force’, made the distinction between this theory of gravitation and fields such as light radiation, electrical induction and magnetic force, which have a continuous physical action across space. Fields are a space wherein continuous action is occurring. Maxwell (1890) cemented the idea of the assignment of a physical character to lines of force with his Electromagnetic theory, describing the physical field produced by electrically charged objects. This theory went beyond a mathematical construct to suggest that the calculated field possesses a physicality that interacts locally with other objects.

1.1.2 Types of fields

Fields can be defined in terms of scalar, vector or tensorial quantities. Since a tensor is the most general of these, the other three parameters can also be described using the notation of tensors.

If a field is defined by a number at each point in space then it is a scalar field, or a tensor field of rank zero. The density of a fluid as a function of position is an example of a scalar field. A vector field, also called a first rank tensor field, is more general than a scalar field in that it defines the direction of the field at each point in a one-dimensional array. Each component of the direction is a scalar. More general still is the tensor field, which can be defined to all orders/ranks. This type of field is used in differential geometry, algebraic geometry and in the analysis of stress and strain in materials. The tensors that define all points in a tensor field represent physical properties that are too complex to be handled by a vector. Einstein's theory of General Relativity, for example, employs a fourth-order tensor known as the Riemann curvature tensor to describe the curvature of spacetime, which is a four-dimensional object. Maxwell's formulation of the electromagnetic field, while defined by a pair of vector fields, that is, the electric field \mathbf{E} and magnetic field \mathbf{B} , is described in the tensorial formulation of classical dynamics by a second-order antisymmetric tensor F , called the Faraday tensor.

There are other mathematical entities in physics that can consist of multi-dimensional arrays of numbers but are not characterized as tensors. One example is the spinor, which differs from a tensor in that it does not transform as a tensor does under a coordinate change. Thus, a field that has a spinor at each point is called a spinor field. A $(2s + 1)$ -dimensional spinor field is used in particle physics to describe particles with spin s , where s is an integer or a half-integer. Fermions are described by a spinor field and bosons by a tensor field.

Within each of the categories described above, a field can be defined as either a classical or a quantum field.

1.1.3 Quantum and classical description of fields

The theory of electromagnetism as founded by Faraday and Maxwell is a classical field theory. From this perspective, the electromagnetic field can be seen as a smooth and continuous field that propagates in a wave-like manner. Faraday found that the electric and magnetic fields \mathbf{E} and \mathbf{B} are not only force fields that dictate motion but carry energy as well. In the absence of any charge, and under a suitable choice of gauge function,

electromagnetic waves in free space are a function of the magnetic vector potential, which is defined at every point in space.

In the presence of charged particles, Maxwell's equations describe the interaction between the electromagnetic field and moving charges. This so-called electrodynamic field is the result of the existence of both the magnetic vector and electric scalar potentials, the latter being the potential energy per unit charge, and is an anti-symmetric second-order tensor field in space-time. Other cases of the electromagnetic field are the electrostatic field, defined by a scalar potential at every point in space, therefore a scalar field, and the magnetostatic field, which is defined by a vector potential and is therefore a vector field.

If one wishes to look at a certain limit of a field theory, it is possible to make approximations so that the more general, rigorous field theory is reduced to a simpler model. Optical fields, characterized by very high temporal frequencies, are a sub-category of electromagnetic fields, where a single scalar quantity can be used to describe the electric field of the light wave, rather than a more rigorous vector model. This description of light is known as 'scalar physical optics'. Within scalar physical optics, there are particular definitions for the regions of electromagnetic radiation around an object. An object can transmit electromagnetic radiation directly, as with a transmitting antenna, or indirectly, by scattering incident radiation. We can approximate the fields close to the objects under 'near field' conditions and similarly for the regions that lie at greater distances, under 'far-field' conditions. These approximations underly a lot of the work presented in this thesis are therefore treated in detail throughout.

At the turn of the nineteenth century the quantum theory of electromagnetic fields began to form. In 1900, Planck stipulated an explanation for blackbody radiation whereby absorption and emission of radiation by atoms occurs discontinuously in quanta. Einstein expanded on this through his work on the photoelectric effect, concluding that the electromagnetic field itself was quantized, with photons defined as the quanta of this field. The first formalism for the quantum theory of electromagnetic fields was laid down by Dirac in 1927 in his paper 'Quantum theory of the emission and absorption of radiation'. The distinction between how a classical field and a quantum field are treated mathematically is with the use of a number or quantum operators, respectively. Like with

classical fields, quantum fields can be approached mathematically as solutions to their governing equations. Thus, quantum electrodynamics (QED) is a quantized recasting of classical electrodynamics, characterized by quantum mechanics, and has been extremely successful in showing agreement between theory and experiment (e.g. Donati et al., 1973).

Regarding the development of QED, the form of the interaction is well known from the classical theory. There are other interactions for which there is not a corresponding classical theory to draw from. Quantum chromodynamics (QCD) and the electroweak theory are examples of such quantum fields. However, QCD and the electroweak theory were deeply influenced by the successes of classical electromagnetic theory as embodied by its tensorial formulation and its quantum generalization in QED. These will not be expanded on here as this thesis is restricted mostly to electromagnetic fields but comprehensive descriptions can be found in Mandl and Shaw (2010).

Many are of the opinion that quantum mechanics should underly all physical phenomena, requiring a recast of all classical theory in terms of quantum mechanics. The quantization of electromagnetic fields laid down the groundwork for the quantization of any classical field, where the quanta of a field are particles with well-defined properties ¹.

As the theory which forms the foundation for the work in this thesis is derived from a classical perspective of electromagnetic fields, it is not necessary to go into more detail on quantum field theory. For a valuable resource on quantum field theory, see the previously-cited text by Mandl and Shaw (2010).

The following two subsections will lay down some facts about fields that are relevant for the remainder of the thesis before continuing on to mathematical treatment of fields in Sec. 1.2.

1.1.4 Free fields

Every field theory possess a description of the scenario in which the field is absent of any charges or scatterers. This scenario is known as the ‘free-field’. The formalism that corresponds to the free-field describes the behaviour of a field in a vacuum.

¹An exception to this is the incompatibility of General Relativity with quantum mechanics, which is a topic of much ongoing research (see e.g. Serway et al., 2004).

There are numerous techniques for creating a free field. The emission of vacuum electromagnetic waves, for example, may be brought about through the acceleration and deceleration of an electric charge. Charges that are oscillating are continuously accelerating and decelerating, making an oscillating charge a useful source of free electromagnetic waves. This approach is adopted in the use of an FM-receiving radio antenna and a set-top TV antenna. Another source of a free-field beam is the laser, which is used extensively in visible-light optics. Lasers produce such a beam via the process of stimulated emission.

One can also describe the movement of a particle beam in a vacuum. The emission of an electron beam in free space can be brought about using an electron gun, which heats a metal plate so that the electrons are free to move. Placing an anode nearby to attract the electrons towards it creates an electron beam (e.g. by Crewe et al., 1968). A similar mechanism is used in an x-ray tube for the production of characteristic x-rays. Electrons, having been emitted using thermal emission, are accelerated by a high voltage to collide with a metal target. The deceleration of high-speed electrons that slam into a metal target produces x-rays. These x-rays are typically used in medical diagnostic procedures (see e.g. Ng et al., 2012).

1.1.5 Scattering and diffraction

When regarding the evolution of a field in space, it is necessary to consider the interactions of the field in question with various media. Scattering is the term used to describe the general process whereby radiation, such as light or a beam of charged particles, deviates from its trajectory by collisions with particles or other localised non-uniformities in the medium through which it traverses. There are many different forms of scattering, such as the scattering of an electron wavefield by a crystal or the scattering of neutrinos by nuclei. An electromagnetic field can be scattered by various media such as lenses and other optical elements, together with any distribution of matter. For example, sunlight is scattered by particles in the atmosphere such as air molecules, aerosols and ice crystals producing various phenomena. One such phenomenon is Rayleigh scattering, which preferentially scatters blue light from the sun, turning the sky blue (Rayleigh, 1871).

In the domain of electromagnetic radiation, the phenomena of transmission, reflection and refraction, which are consequences the description of light as rays, are macroscopic manifestations of scattering which occurs at a submicroscopic level.

In the description of electromagnetic radiation as waves, the phenomenon of diffraction emerges, defined as the bending of light around edges and smooth objects. It is also well-known that matter exhibits wave-like behaviour, a phenomenon first exhibited using electrons in the Davisson–Germer experiment (Davisson and Germer, 1928) and subsequently with neutral atoms (Doak et al., 1999; Kouznetsov and Oberst, 2005), which has been used to demonstrate atomic holography (Shimizu and Fujita, 2002) as well as to explain the quantum Zeno effect (Kouznetsov and Oberst, 2005). The effects of diffraction on an electromagnetic wavefield can be predicted by the angular spectrum formalism, which will be treated in greater detail in Chapter 2. The Geometrical Theory of Diffraction, which provides a means of predicting diffracted fields using a ray formalism, is treated in detail in Chapter 4 and provides much of the basis for the work done in Sec. 4.2.

1.2 Mathematics as a language for quantitatively studying fields

This section describes the mathematical means of evaluating electromagnetic fields that is adopted throughout this entire thesis. The general principle known as the ‘principle of least action’ is first described, as it is from this that many of the known physical laws can be deduced. Adopting this formalism, the relevant governing equation of motion for the Maxwell electromagnetic free field is subsequently derived using classical Lagrangian field theory. Finally, the complex scalar representation of the free electromagnetic field is described, as it is this particular representation that facilitates calculations of optical fields, which are the category of electromagnetic fields investigated here.

1.2.1 Principle of least action

There is one principle from which the vast majority of known physical laws can be derived; the principle of least action. This includes electromagnetism, thermodynamics and Newton’s laws of gravity. To demonstrate, the last-mentioned in this list can be framed

in terms of the principle of least action, by stating: the average kinetic energy (KE) less the average potential energy (PE) is as small as possible for an object traveling a path from one point to another. For every possible path that the object can travel, there is assigned an ‘action’, denoted by S . For the motion of a point particle, the action is given by

$$S = \int_{t_1}^{t_2} (KE - PE)dt, \quad (1.2.1)$$

where KE and PE are functions of time. For every possible path there is a different value for the action. The principle of least action requires that we find the path for which that number is a minimum.

Fermat’s principle, also known as the ‘principle of least time’, is associated with the principle of least action in that it defines the path taken by a ray traveling between two points to be the path that takes the least amount of time. The same logic which underlies the principle of least action underlies Fermat’s principle, despite the fact that the former involves the motion of particles and the latter the path traveled by rays. This principle underpins the Geometrical Theory of Diffraction, and is invoked in both Sec. 4.1.1 and in the publication in Sec. 4.2 to calculated diffracted rays.

1.2.2 Classical Lagrangian field theory

Transitioning from point-particle mechanics to field theory, we can switch to relativistic notation to describe a system with a number of degrees of freedom that tends towards infinity. Such a system requires one or more fields $\phi_r(x), r = 1, \dots, N$ to specify it. The state of the system is defined by the ‘Lagrangian density’, given by $\mathcal{L}(\phi_r, \partial^\mu \phi_r)$. The ‘Lagrangian’ L is found by integrating the Lagrangian density over all of the space occupied by the field $\phi_r(x)$,

$$L = \int \mathcal{L}(\phi_r, \partial^\mu \phi_r) dV, \quad (1.2.2)$$

describing the Lagrangian of the system at time t , where $\partial^\mu = \frac{\partial}{\partial x_\mu}$. The evolution of the state of the system in time is given by Hamiltonian’s variational system, defining the action S as

$$S = \int_{t_1}^{t_2} L dt = \int \mathcal{L}(\phi_r, \partial^\mu \phi_r) d^4x, \quad (1.2.3)$$

where $d^4x = dt dV$. The Euler-Lagrange equation of motion, deduced by applying the variation principle $\delta S = 0$, is given by (see Mandl and Shaw, 2010, p. 28)

$$\partial_\mu \left(\frac{\partial \mathcal{L}}{\partial (\partial_\mu \phi_r)} \right) - \frac{\partial \mathcal{L}}{\partial \phi_r} = 0. \quad (1.2.4)$$

The Euler–Lagrange equation can be applied to both classical and quantum mechanics.

We can apply Lagrangian mechanics to find the equation of motion governing the Maxwell electromagnetic field expressed in covariant form. Consider the free-field four-vector potential $A^\mu(x) = (\phi, \mathbf{A})$, where \mathbf{A} is the aforementioned vector potential associated with an electromagnetic field, with an associated Lagrangian density

$$\mathcal{L} = -\frac{1}{16\pi} F^{\mu\nu} F_{\mu\nu}, \quad (1.2.5)$$

where the antisymmetric field tensor $F^{\mu\nu}$ is given by $F^{\mu\nu} = \partial^\mu A^\nu - \partial^\nu A^\mu$. The functional derivatives are given by

$$\frac{\partial \mathcal{L}}{\partial (\partial_\mu A_\nu)} = -\frac{1}{4\pi} F^{\mu\nu} \quad \text{and} \quad \frac{\partial \mathcal{L}}{\partial A_\nu} = 0, \quad (1.2.6)$$

and the equation of motion is the equation of motion for the free Maxwell field,

$$\partial_\mu F^{\mu\nu} = 0, \quad (1.2.7)$$

from which the free-space Maxwell equations for the magnetic and electric fields can be derived. This equation of motion underpins all the theory presented in this body of work.

We close this section by noting that, under a suitable choice of gauge function, Eq. 1.2.7 implies that both the electric and magnetic fields \mathbf{E} and \mathbf{B} obey the d'Alembert wave equations in a vacuum:

$$\left(\frac{1}{c^2} \frac{\partial^2}{\partial t^2} - \nabla^2 \right) \mathbf{E} = \mathbf{0} \quad \text{and} \quad \left(\frac{1}{c^2} \frac{\partial^2}{\partial t^2} - \nabla^2 \right) \mathbf{B} = \mathbf{0}, \quad (1.2.8)$$

where c is the speed of light in a vacuum and ∇^2 is the Laplace operator. This so-called electromagnetic wave equation describes the propagation of electromagnetic waves through a medium.

1.2.3 Scalar representation of electromagnetic waves

Maxwell's field equations in a vacuum provide the basic equations governing electromagnetic fields, using the vector potential \mathbf{A} to derive two vector fields, the electric field and the magnetic field, to specify the dynamics of an electromagnetic field according to Eq. 1.2.7. In many optical problems, however, it is often not important to know the behaviour of a field vector. Rather, we wish to know the average energy of an optical field. Therefore a simplification of the vector representation of optical fields is convenient.

In most optics scenarios, we can employ a single, generally complex, scalar wave function $\Psi(\mathbf{r}, t)$ called the disturbance or the complex amplitude, whose square modulus is equal to the light intensity. This wave function obeys the d'Alembert equation in a vacuum,

$$\left(\frac{1}{c^2} \frac{\partial^2}{\partial t^2} - \nabla^2\right)\Psi(\mathbf{r}, t) = 0, \quad (1.2.9)$$

where $\mathbf{r} = (x, y, z)$. The transition from a vector theory to a scalar theory of electromagnetic optics is treated by Green and Wolf (1953) and Wolf (1959), as well as by Roman (1959) for a field in the presence of charges and currents.

We can decompose the wavefunction $\Psi(\mathbf{r}, t)$ into a superposition of monochromatic fields using the Fourier integral:

$$\Psi(\mathbf{r}, t) = \frac{1}{\sqrt{2\pi}} \int_0^\infty \psi_\omega(\mathbf{r}) e^{-i\omega t} d\omega, \quad (1.2.10)$$

where each monochromatic component is a product of the spatial wavefunction $\psi_\omega(\mathbf{r})$ and harmonic time factor $e^{-i\omega t}$, where ω denotes the angular frequency. The decomposition above does not include any negative values for ω , allowing for analyticity in the complex-analysis sense of the term, and is therefore called the 'analytic signal' associated with the scalar representation of an electromagnetic field. The real and imaginary parts of the

analytic function are related to each other via the Hilbert transform. The actual waveform, however, is only the real part; the actual signal is substituted by the analytic signal for the purposes of analysis, providing a convenient and compact notation. The magnitude and the phase of the complex analytic signal mathematically define an envelope and phase for the waveform. More detail on the analytic signal can be found in words by Born and Wolf (1999), Gabor (1946) and Bedrosian (1962).

The analytic signal may be visualised via a ‘phasor’, which is a concept frequently used in circuit analysis to represent a complex number. Phasor diagrams, a tool for visualising phasors, will be discussed as part of the next section, as they form a significant part of this thesis.

Before concluding this section on the mathematical theory for electromagnetic fields, it is useful to write down the time-independent differential equation that governs the evolution of the spatial wavefunction $\psi_\omega(\mathbf{r})$ associated with Eq. 1.2.10. Substituting Eq. 1.2.10 into the d’Alembert equation results in

$$\int_0^\infty \left[\left(\nabla^2 + \frac{\omega^2}{c^2} \right) \psi_\omega(x, y, z) \right] \exp(-i\omega t) d\omega = 0. \quad (1.2.11)$$

From this equation it can be deduced that the quantity in square brackets vanishes, arriving at the Helmholtz equation:

$$\left(\nabla^2 + k^2 \right) \psi_\omega(x, y, z) = 0, \quad (1.2.12)$$

which describes the evolution of the spatial wavefunction associated with a given monochromatic component of Eqn. 1.2.10. It is a key equation of scalar diffraction theory and, as this theory concerns itself with constructing various solutions to the Helmholtz equation, underlies a significant portion of the work in the present thesis. It is important to note that the Helmholtz equation is identical to the time-independent free-space Schrödinger equation for spinless non-relativistic particles. As this thesis is concerned with electromagnetic radiation, it is not necessary to define a quantum-mechanical theory for evaluating the optics of particles, which can be found in a standard text on quantum mechanics, such as that by Messiah (1961).

1.3 Argand-plane representation of complex numbers

1.3.1 Basic theory of mappings

In linear algebra a ‘function’ is a rule f that associates each element in a set A with one and only one element in a set B . If f associates an element a with an element b , then $b = f(a)$, and it can be said that b is the ‘image’ of a under f . The set A is defined as the ‘domain’ and B is the ‘codomain’ of f . The subset of B with all possible values for f as a varies over A is called the ‘range’. Commonly, A and B are sets of real numbers, in which case f is a ‘real-valued function of a real variable’. In other cases, B is a set of real numbers and A is a set of vectors in R^n , where n is the number of variables.

If the domain of a function is R^n , and the codomain is R^m , then f is called a ‘map’ from R^n to R^m , and is a generalisation of a function. This is denoted by:

$$f : R^n \rightarrow R^m. \quad (1.3.1)$$

In the case where $m = n$, f is called an ‘operator’ on R^n . For a detailed overview of the properties of maps and transformation, see the text by Howard and Rorres (2005). Here it is only necessary to define a few relevant properties.

A map is considered ‘one-to-one’ if it maps distinct vectors, or points, in R^n into distinct vectors, or points, in R^m . It follows that for each vector \mathbf{w} in the range of a one-to-one mapping, there is exactly one vector \mathbf{x} such that $f(\mathbf{x})=\mathbf{w}$. A mapping that is one-to-one is ‘invertible’ owing to the fact that distinctness has been preserved.

A mapping which may, but not necessarily, associate a given member of its range with more than one member of its domain is known as a ‘many-to-one’ mapping. To give a simple example in terms of a function f which is a mapping from R to R , consider a trigonometric function such as $\sin x$. Given that $\sin x = \sin(2\pi + x) = \sin(4\pi + x)\dots$, the function $f = \sin x$ is called many-to-one. As distinctness is not preserved under these circumstances, the mapping is not considered invertible.

The Jacobian matrix is a matrix consisting of all first-order partial derivatives of a vector-valued function f . For a function defined generally by 1.3.1, which takes the vector $\mathbf{x} \in \mathbb{R}^n$ as the input and outputs the vector $\mathbf{f}(\mathbf{x}) \in \mathbb{R}^m$, the Jacobian matrix is an $m \times n$ matrix defined by

$$\mathbf{J} = \begin{bmatrix} \frac{\partial f_1}{\partial x_1} & \cdots & \frac{\partial f_1}{\partial x_n} \\ \vdots & \ddots & \vdots \\ \frac{\partial f_m}{\partial x_1} & \cdots & \frac{\partial f_m}{\partial x_n} \end{bmatrix}. \quad (1.3.2)$$

If $m = n$ then the matrix is a square matrix. The determinant of the Jacobian, simply called the ‘Jacobian’, provides important local information about the mapping, for example, regarding whether a many-to-one mapping is evident. The Jacobian determinant is evoked extensively throughout Chapter 3, particular in the publication inserted into Sec. 3.2.

The work in this thesis is largely concerned with the utility of a particular kind of mapping, a mapping to the Argand plane. A two-dimensional differentiable continuous single-valued complex function $\Psi(x, y)$ induces a mapping $M : \mathbb{R}^2 \rightarrow \mathbb{C}$ to the Argand (complex) plane, given by

$$M(\Psi(x, y)) \rightarrow [Re\Psi, Im\Psi], \quad (1.3.3)$$

where $Re\Psi$ and $Im\Psi$ denote the real and imaginary parts of $\Psi(x, y)$, respectively.

The Argand plane provides a visual representation of the kind of complex functions used to represent optical fields and is a topic that is treated in detail throughout this thesis. There exists precedents where an Argand mapping is used to visually represent some complex function to aid in the analysis of a real-world problem. Below are some practical applications for the use of Argand plane as a graphical aid.

1.3.2 Practical use of Argand-plane representation

The complex number z has the form

$$z = x + iy, \quad (1.3.4)$$

and can be expressed in polar coordinates (r, θ) , as

$$z = r \cos \theta + ir \sin \theta, \quad \text{where } x = r \cos \theta, \quad y = r \sin \theta. \quad (1.3.5)$$

Furthermore, due to the Euler formula, z can be represented as

$$z = re^{i\theta}. \quad (1.3.6)$$

The complex number z can be represented in the Argand plane as shown in Fig. 1.1.

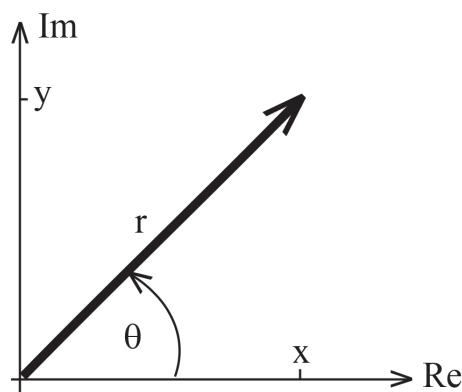


Figure 1.1: Argand-plane representation of the complex number $z = x + iy$.

As previously stated in Sec. 1.2.3, in the analysis of waves, the complex-number representation offers a description that is mathematically simpler to process in the form of the complex analytic signal. A harmonic waveform can be taken to be the real part of the analytic signal $\psi(x, t) = Ae^{i\omega t}$, where A is the amplitude and ω is the angular frequency. For a traveling waveform, the angle in Fig. 1.1 becomes ωt , suggesting that the arrow rotates at a frequency ω . This rotating arrow and its associated phase angle constitute a phasor.

In AC circuit theory, two sinusoidal waveforms of the same angular frequency ω can have a phase difference between them. To indicate the relationship between the amplitude and phase of the waveform, terms such as ‘lag’ and ‘lead’, as well as ‘in-phase’ and ‘out-of-phase’ are employed. Represented in the time-domain form, the generalised sinusoidal

expression is given by $A_t = A_m \sin(\omega t \pm \phi)$. The phase difference ϕ can be visualised by employing what is known as ‘phasor diagrams’.

To demonstrate, consider the diagram in Fig. 1.2, showing two sinusoidal waveforms, whereby one (the current i) is lagging behind the other (voltage v) by 45 degrees, or $\pi/2$ radians.

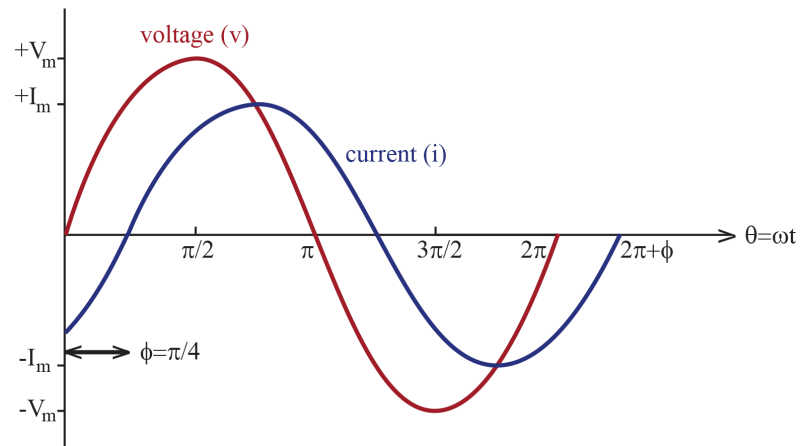


Figure 1.2: Two sinusoidal waveforms representing the voltage (red) and current (blue). The current i is lagging behind the voltage v by $\phi = \pi/4$ radians.

The phasor diagram, lying in the Argand plane where the real part of the waveform is displaced along the x-axis and the imaginary part along the y-axis, is shown in Fig. 1.3.

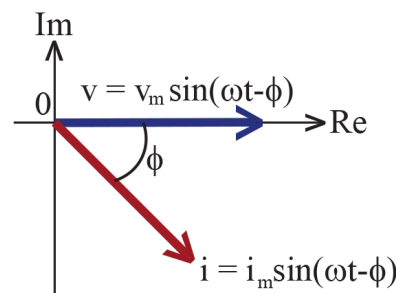


Figure 1.3: Phasor diagram representing the phase difference between the two waveforms illustrated in Fig. 1.2.

Next, we look at the application of Argand-plane analysis in engineering. In the analysis of control systems, the ‘root locus analysis’ is a method used to determine all the roots of the differential equations governing the system. The roots are desired as they describe the natural response of the unit. This method was developed by Evans (1948) and uses a graphical plot in the complex plane to explore how the roots of the system change with the variation of some system parameter. This is a way to determine the stability of a system.

For further reading, see the book by Kuo (1987, pp. 329–388) as well as articles by Evans (1948; 1950) and Williamson (1969).

Finally, we can find an example of Argand-plane graphical analysis in optics. Fresnel diffraction is a paraxial version of the angular spectrum formalism and is treated in detail in the next chapter. The Fresnel integrals arise in the description of Fresnel diffraction and are defined as

$$S(u) = \int_0^u \sin(\tau^2) d\tau, \quad C(u) = \int_0^u \cos(\tau^2) d\tau, \quad (1.3.7)$$

where u is an arbitrary variable which characterizes the Fresnel integrals.

The simultaneous parametric plot of $S(u)$ and $C(u)$ results in the Cornu spiral, shown in Fig. 1.4.

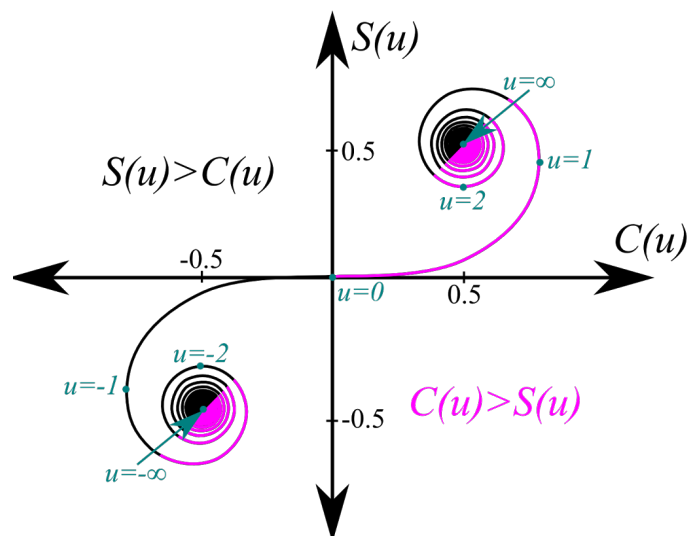


Figure 1.4: The parametric plot of Fresnel integrals $S(u)$ and $C(u)$, resulting in the Cornu spiral (from Morgan, 2011, with permission).

The Cornu spiral can be seen as an Argand plane mapping of the points $B(u) = S(u) + iC(u)$ and represents diffraction from the edge of a half plane. Morgan et al. (2010) generalized the Cornu spiral by describing the Argand-plane image corresponding to diffraction from a cylindrical edge. The generalisation of the Cornu spiral is a topic that is explored throughout the following chapters.

The remainder of this thesis is comprised of three published bodies of first-author work concerning the Argand-plane mappings induced by complex scalar wavefields, each with

a foreword. Chapter 2 focuses on the utility of the Argand plane in the analysis of vortical fields and introduces singularities of the mapping to the Argand plane, called vorticity singularities. The duality between these singularities and singularities of the phase of the complex scalar wavefield, vortices, is explored. Chapter 3 features an experimental realisation of the theory outlined in Chapter 2, including experimentally constructed vorticity singularities, utilising visible light. Chapter 4 moves away from visible light and into the region of hard x-rays. The generalisation of the Cornu spiral for objects with increasingly complex geometry is explored. The generalised Cornu spiral of these objects is experimentally realised using hard x-rays. Finally, Chapter 5 discusses future work and possible applications of the work presented here. Chapter 6 concludes the thesis.

Chapter 2

Argand-plane representation of optical vortices in a two-dimensional complex scalar wavefield

In this chapter, the Argand-plane mappings induced by a two-dimensional optical speckle field is studied, with particular attention to the Argand-plane representation of the optical vortices that may be associated with such a speckle field. Preceding the as-published body of work is some background theory of singularities of wave and ray theory, namely vortices and caustics, as well as a discussion on various approaches toward the simulation or generation of optical vortices. The vortices simulated here are calculated by forward-propagating an optical speckle field, and as such, the derivation of the formalism used to do so, known as the angular spectrum formalism, is derived.

2.1 Introduction and background theory

2.1.1 Singularities of wave theory and ray theory

Many mathematical theories possess singularities, which manifest themselves on different length scales. A singularity can be interpreted as any point at which the predictions of

that theory break down. When a theory does exhibit this so-called singular behaviour, it is sometimes necessary to go a higher, or more general theory to account for the singularity. In the shortwave limit of an optical wavefield, we can neglect the finiteness of the wavelength and adopt a ray approach for solving optical problems. This approach, known as Geometrical Optics, forms the basis of the work presented in Chapter 4 of this thesis, and is therefore described in detail in Sec. 4.1.1. This ray theory of optical fields predicts, under focusing conditions, regions of infinite intensity known as caustics. Caustics are singularities of ray theory. The formation of one such region, called a point caustic, via a perfect lens is shown in Fig. 2.1. There, it can be seen that neighbouring rays intersect at the site of a caustic. The cross-sectional area of the associated tube of rays is zero, and consequently, an infinite amplitude is predicted at the point of intersection (Keller, 1962). The point caustic requires infinitely many rays to pass through a single point and is therefore not stable with respect to perturbation (Thom, 1975).

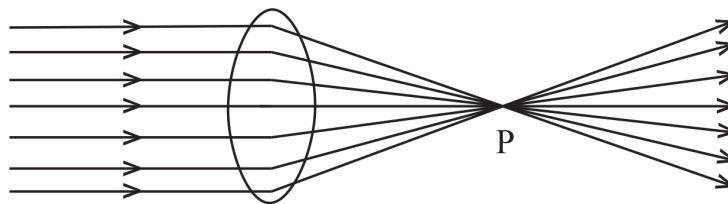


Figure 2.1: *Light rays indicated by arrows, upon traveling through a perfect lens, are focused onto a single point P, forming a point caustic.*

For a ray caustic that is stable, one can look to the surface caustic, wherein a family of rays form an envelope (Thom, 1975). Examples of surface caustics are the cusp, commonly seen at the surface of a cup of coffee, and the fold. Higher order caustics include the elliptic umbilic and hyperbolic umbilic. The mathematics of caustics is dictated by catastrophe theory, the study of singularities and gradient mappings, which predicts an infinite hierarchy of caustics. For an in-depth treatment of catastrophe theory, see the seminal book by Nye (1999).

The geometric description of light, while being enormously successful in evaluating light fields under a plethora of circumstances, predicts these caustic regions of infinite density, which are a physical absurdity. It is therefore necessary to pass to the wave theory of optical fields, where light is regarded as possessing a finite wavelength.

The wave theory of optics possess its own singularities, known as phase vortices. These are singularities of the phase of the wavefield and are classified as screw-type singularities (Berry, 1981). They are characterized by regions of zero intensity, being a consequence of the wave nature of an optical field, of which destructive interference is a feature. They are entirely complementary to ray caustics; where caustics possess an infinite intensity, destructive interference of waves results in a zero intensity at the core of the vortex. However, in moving from ray theory to wave theory, caustic surfaces of infinite intensity are softened to peaks that often form a skeleton decorated with phase vortices. An example of this is the vortices present in the vicinity of caustics that are formed in the focal volumes of coherently illuminated aberrated lenses (Allen et al., 2001b).

We can write the equation for a simple polynomial vortex. Up to a continuous deformation, a phase vortex at (x_0, y_0) is locally given by

$$\psi_{\pm} = (x - x_0) \pm i(y - y_0), \quad (2.1.1)$$

for $\text{Re}\psi = 0$ and $\text{Im}\psi = 0$. Here, ψ_+ denotes a vortex, around which the phase winds in an anti-clockwise direction, and ψ_- an anti-vortex, with a clockwise phase-winding.

In Sec. 2.2, vortices and caustics are described in detail, as is the nature of their complementarity. There, it is shown that the Argand plane can be used in the analysis of phase vortices present in an optical field. This paper also predicts singularities of the Argand-plane mapping induced by complex scalar wavefields, known as vorticity singularities, or Argand-plane caustics in the sense that they appear to possess the same structure and hierarchy as ray caustics despite not being a representation of a physical gradient mapping. The connection between the caustic-like singularities of the Argand-plane mapping and singularities of the phase of the physical wavefield is explored in detail.

Further reading on the vortex–caustic duality can be found in Berry (1981).

2.1.2 Methods for vortex generation

For the analysis carried out in this chapter, it was necessary to find a method to generate optical vortices. There are many methods of vortex generation for optical fields. One

method involves the use of diffractive optics to transform a spatially coherent flat phase beam into beams with optical vortices. Bazhenov et al. (1990) created a vortex beam by modifying a diffraction grating to include a dislocation at its centre. The modified device is called a 'fork' hologram. More recent examples of the use of a fork hologram in the creation of a vortex beam can be found by Bekshaev et al. (2010) and Bekshaev et al. (2014).

In 1992, Allen et al. made the important discovery that beams with optical vortices carry orbital angular momentum. They adopted a method using cylindrical lenses to convert a Hermite-Gauss mode, a beam with zero angular momentum, into a Laguerre-Gaussian mode, a beam carrying a well-defined angular momentum. The same method was adopted by Lin et al. (2011) and Yu et al. (2015).

Another optical element that can be used in the generation of optical vortex beams is the spiral phase plate (SPP), a method pioneered by Beijersbergen et al. (1993; 1994). These are discs with refractive index n , and an optical thickness Δt that increases with azimuthal angle. When a plane wave passes through the spiral phase plate it incurs a phase shift determined by n and Δt . Upon transmission, the beam has a vortex. More recently Xin et al. (2014) have adopted this method, combining quarter-wave plates and spatially-variable half wave plates to construct a SPP for generating optical vortices, and Janicijevic and Topuzoski (2016) have generated optical vortices using a helical lens, which is a combination of the SPP and a thin lens. Similarly, Peele et al. (2002) have used a SPP to generate an x-ray vortex, that is, an optical vortex in a field consisting of x-ray photons. Despite all other methods that have been developed, several of which are mentioned above, none match the performance of computer-generated holograms for generating vortex beams (Heckenberg et al., 1992; Dennis et al., 2009). The availability of spatial light modulators (SLMs), devices that have to ability to modulate amplitude, phase or polarization of light, has made computer-generated holograms popular due to their flexibility and performance. In phase modulation mode, an SLM is able to imprint a phase component directly onto a beam. Examples of recent work adopting SLMs to generate vortices are found in Rickenstorff and Ostrovsky (2013), Huang et al. (2014), Gao et al. (2015) and Kapoor et al. (2016). Vyas and Senthilkumaran (2010) have used a SLM

integrated into a Mach-Zehnder interferometer to generate a vortex beam, as shown in Fig. 2.2. There, a laser emits linearly polarized light, which is then spatially filtered and collimated. A beam splitter (BS1) splits the beam into two arms. One arm passes through an SLM which uses a computer-generated phase mask to impart linear phase variations on the beam. The beam diffracted from the SLM is then made to interfere with the other arm of the Mach-Zehnder interferometer using BS2, and the resulting ‘interferogram’ is captured by the CCD. The interferogram, which is a series of distorted fringes containing phase information as a result of the superpositioning of the two beams, is used to detect the presence of vortices. A neutral density filter (NDF) is used to make the amplitude of the reference beam equal to that of the vortex beam, which has the effect of enhancing the quality of the fringes. More detail on interferograms is found ahead in Sec. 3.1.2.

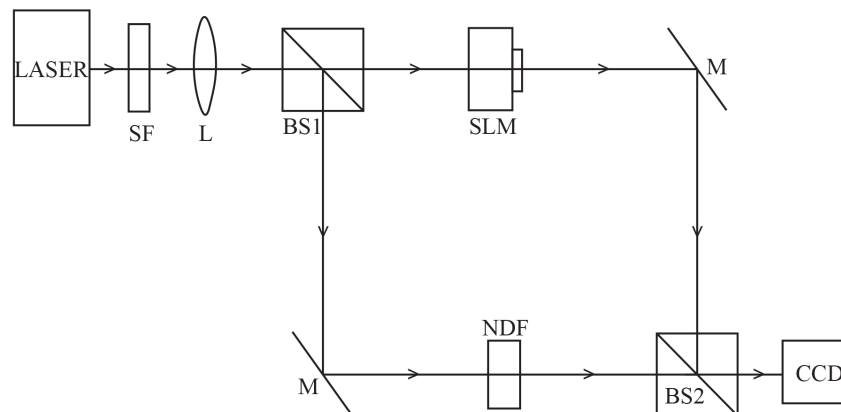


Figure 2.2: Depiction of the use of an SLM to generate a vortex beam, after Vyas and Senthil Kumar (2010). A laser (L) emits light which is then spatially filtered (SF) and collimated via a lens (L). A beamsplitter (BS1) splits the beam into two arms. The top arm passes through an SLM and interferes with the second arm via a mirror (M). The second arm is directed, using a mirror, to pass through a neutral density filter (NDF) to adjust the amplitude. The resulting interferogram exits BS2 and is received by the detector.

The published work in Sec. 2.2 adopts a method for numerically generating optical vortices that involves the spatial filtering of two-dimensional complex optical white noise. This creates a speckled pattern of dark and light spots that results from interference effects, known as a speckle field. The speckle field is then allowed to forward-propagate, which has the effect of generating propagation-induced vortices. The numerical method is explained in detail in Sec. 2.2. This is a similar technique to that explored by Staliunas et al. (1995), who generate a random optical field with Gaussian statistics, which was then allowed to propagate in order to induce vortices.

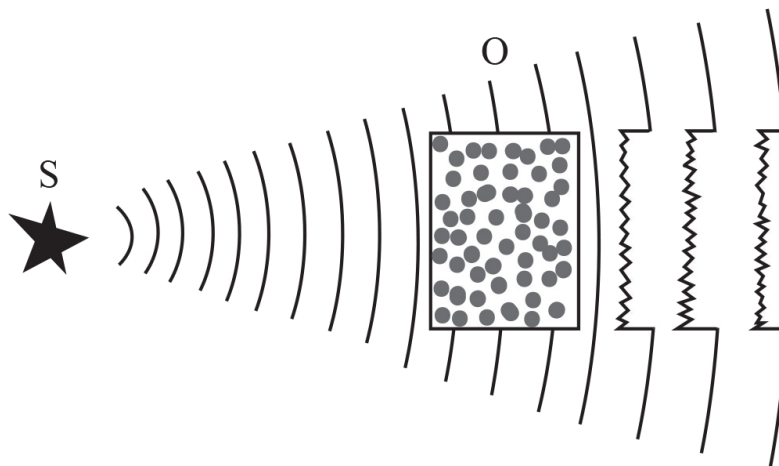


Figure 2.3: *Generation of x-ray speckle, after Kitchen et al. (2015). X-rays are emitted from a source S and pass through a random phase object O, resulting in a speckle field.*

Before continuing to describe the process used for computationally propagating the speckle field through space, namely the angular spectrum formalism, note that optical speckle has previously been associated with propagation-based phase vortices. For example, Kitchen et al. (2004) indicated the presence of optical vortices in the speckle field revealed by the phase contrast x-ray imaging of animal lungs. They noted that the speckle field is a result of the focusing effect of the individual alveoli, each one behaving as an aberrated refractive lens. The presence of vortices in a speckle field at length scales comparable to the wavelength had previously been noted by Bobrov (1991), Shvartsman and Freund (1994), Staliunas et al. (1995), and Aksenov et al. (1998). Figure 2.3 demonstrates x-ray speckle generation as per Kitchen et al. (2015). Relating to this are the aforementioned vortices noted by Allen et al. (2001b) in the focal volumes of aberrated lenses, which is an effect first noted by Boivin et al. (1967) in the focal region of an ‘aplanatic system’. At length-scales that are large compared to the wavelength, surface caustics were observed in the same focal volumes, owing to refraction of the optical field due to the lens aberration. This is an example in the literature where the complementarity between ray caustics and phase vortices is realised.

The study of speckle fields is an important area of physics, necessary to solve problems in various areas of study. Some examples are the areas of adaptive optics, star speckle interferometry and image reconstruction, where the reduction of wavefront distortion is important (see Aksenov et al., 1998, and references therein).

The experimental generation and analysis of optical speckle constitutes a significant part of the next chapter.

2.1.3 Angular spectrum of plane waves

It is necessary to describe the method for evaluating a propagated field downstream of a disturbance, known as the angular spectrum. This technique is used throughout the work included later in this chapter and in subsequent chapters. For a complete derivation, see Paganin, 2006.

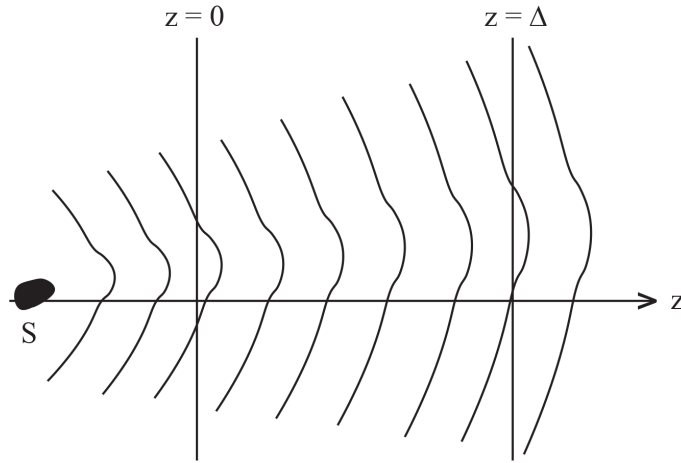


Figure 2.4: A source S radiating an electromagnetic field which then propagates into the half space $z \geq 0$.

Figure 2.4 shows a source S which radiates a scalar electromagnetic wave, denoted by the monochromatic wavefield ψ_ω , from within the half space $z < 0$, propagating forward into the half-space $z \geq 0$ which is free from sources and charges. Assuming that ψ_ω propagates strictly from left-to-right, the angular spectrum formalism can be used to construct an operator that can be applied to wavefield evaluated over the plane $z = 0$ to give the propagated wavefield evaluated over a plane $z = \Delta$ lying downstream of the initial disturbance.

Given a Cartesian coordinate system (x, y, z) with the positive z -axis acting as the optical axis, the wavefield evaluated over the plane lying at $z = \Delta$, where $\Delta \geq 0$, is given by

$$\psi_\omega(x, y, z = \Delta) = \frac{1}{2\pi} \int \int \hat{\psi}_\omega(k_x, k_y, z = 0) \exp\left[i\Delta\sqrt{k^2 - k_x^2 - k_y^2}\right] \times \exp\left[i(k_x x + k_y y)\right] dk_x dk_y, \quad (2.1.2)$$

where $\hat{\psi}_\omega(k_x, k_y, z=0)$ is the Fourier transform of $\psi(x, y, z=0)$ with respect to x and y , and k_x and k_y are the corresponding Fourier-space variables. The wavevector \mathbf{k} has a magnitude $k = 2\pi/\lambda$ for wavelength λ . Note that this formalism provides an exact solution to the Helmholtz equation, Eq. 1.2.12, for forward-propagating monochromatic scalar electromagnetic beams.

We can express the angular spectrum formalism using an operator \mathcal{D}_Δ which describes the act of free-space propagation. Thus:

$$\psi_\omega(x, y, z = \Delta) = \mathcal{D}_\Delta \psi_\omega(x, y, z = 0), \quad \Delta \geq 0, \quad (2.1.3)$$

where the ‘diffraction operator’ is defined as

$$\mathcal{D}_\Delta = \mathcal{F}^{-1} \exp \left[i\Delta \sqrt{k^2 - k_x^2 - k_y^2} \right] \mathcal{F}, \quad (2.1.4)$$

with the operators acting from right to left. \mathcal{F} denotes the Fourier transform operator and \mathcal{F}^{-1} the inverse direction.

If the plane-wave components of the forward-propagating field ψ_ω make a small angle with the optical axis, it is said to be paraxial. As previously mentioned, Fresnel diffraction is a paraxial version of the angular spectrum formalism. Under these circumstances the x - and y - components of the wavevector \mathbf{k} , k_x and k_y , will have a magnitude much less than that of k_z . Therefore,

$$\sqrt{k^2 - k_x^2 - k_y^2} \approx k - \frac{k_x^2 + k_y^2}{2k}, \quad (2.1.5)$$

so 2.1.4 becomes, omitting an irrelevant phase factor,

$$\mathcal{D}_\Delta^{(F)} = \mathcal{F}^{-1} \exp \left[\frac{-i\Delta(k_x^2 + k_y^2)}{2k} \right] \mathcal{F}, \quad (2.1.6)$$

where $\mathcal{D}_\Delta^{(F)}$ is the diffraction operator corresponding to Fresnel diffraction (Paganin, 2006). In contrast with Eq. 2.1.2, this is an approximate solution to the Helmholtz equation.

The forward and inverse Fourier transforms in the operator form of the angular spectrum formalism can be evaluated numerically using the fast Fourier transform (FFT), which is an efficient method of calculating a Fourier transform (see Press et al. (1992)). The propagation distance Δ can vary from zero through to the near-field and intermediate field. The ‘Fresnel number’, denoted by N_F , provides an approximation to the near-, intermediate- and far-field definitions. It is given by,

$$N_F = \frac{l^2}{\lambda\Delta}, \quad (2.1.7)$$

where l is the size of the smallest transverse feature, essentially specifying the resolution and λ is the wavelength of the beam. For a value of Δ such that $N_F \gg 1$ the beam is in the near-field. For $N_F \approx 1$, the beam is in the intermediate field and $N_F \ll 1$ indicates the far-field. As one makes the transition to the far-field, the phase of the angular spectrum propagator, $\Delta\sqrt{k^2 - k_x^2 - k_y^2}$, becomes under-sampled and the angular spectrum formalism breaks down in Fourier space. It can then be replaced with a one-FFT form of the Fresnel diffraction operator, which will allow one to numerically propagate to the far-field. This approximation has the form of a paraxial modulated spherical wave emanating from the plane of the unpropagated disturbance (see Paganin, 2006 for more detail). The angular spectrum formalism and Fresnel diffraction integral are used extensively throughout the work in this thesis.

2.2 Duality between phase vortices and Argand-plane caustics

On the following pages is inserted the as-published form of the first of three first-author papers arising from this thesis. The paper has been published as:

F. Rothschild, M. J. Kitchen, H. M. L. Faulkner, and D. M. Paganin, ‘Duality between phase vortices and Argand-plane caustics’, *Opt. Commun.* **285**, pp 4141–4151 (2012).



Duality between phase vortices and Argand-plane caustics

Freda Rothschild*, Marcus J. Kitchen, Helen M.L. Faulkner, David M. Paganin

School of Physics, Monash University, Victoria 3800, Australia

ARTICLE INFO

Article history:
Received 20 December 2011
Accepted 9 June 2012
Available online 4 July 2012

Keywords:
Optical vortices
Optical caustics
Argand mappings
Catastrophe theory
Vortex generation

ABSTRACT

Singularities in the mappings of complex two-dimensional vortical wavefields to Argand space are used here to investigate the duality between vortices in the physical field and caustic-like structures in the Argand plane. Such map singularities are exemplified via a method of optical vortex generation based on low-pass filtering of two-dimensional noise. The presence of Argand-plane fold caustics crossing the Argand-plane origin is tied to changes in vortex numbers in the physical wavefield. Increasing the low-pass filter cutoff leads to higher-order Argand-plane caustic singularities, such as the hyperbolic umbilic catastrophe. This work presents a duality between vortices and caustics, explores the Argand plane as a tool in analysing optical wavefields, and provides a new environment for studying catastrophes.

© 2012 Elsevier B.V. All rights reserved.

1. A brief introduction to singularities

Singularities are a feature of many physical models. A theory can possess singularities of different categories, manifesting themselves on different spatial scales. Certain theories, such as the wavefunction in Schrödinger's wave mechanics and the complex analytic signal of scalar electromagnetic wave optics, describe waves using complex scalar functions of position and time. These complex functions may possess screw-type phase singularities, namely wavefront dislocations [1], that exhibit vortical behaviour. In the short-wave limit, however, singularities of ray/particle theory, called caustics [2], are manifest. A certain complementarity between caustic and vortex singularities is developed in this paper. Specifically, we demonstrate a link between the presence of vortices in a complex two-dimensional coherent wavefield (such as a monochromatic scalar electromagnetic wave) and associated caustics in the mapping from real-space to the Argand plane that is induced by such a vortical field.

Vortices are ubiquitous, in the sense that they are present in most non-trivial complex scalar wavefields [3]. They appear in macroscopic systems including plumes of smoke, hurricanes and optical speckle, and in microscopic systems such as the angular momentum eigenstates of the hydrogen atom, in superfluids and in turbulent Bose–Einstein condensates (BECs). Caustics, too, are found ubiquitously, in macroscopic systems such as filaments in the large-scale structure of the universe, optical caustics in cups of coffee and swimming pools, and in microscopic systems such as the focal volume of coherently illuminated aberrated lenses.

Focussing attention on scalar wave optics, a single Cartesian component of linearly polarised light can be represented by a complex analytic signal $\psi(\vec{r}, t)$ with intensity $I(\vec{r}, t) = |\psi(\vec{r}, t)|^2$ and phase $\varphi(\vec{r}, t)$, such that [4,5]

$$\psi(\vec{r}, t) = \sqrt{I(\vec{r}, t)} \exp[i\varphi(\vec{r}, t)], \quad (1)$$

here \vec{r} is the position vector in Cartesian coordinates and t is the time [6]. The surfaces of constant phase are identified with wavefronts. Screw-type and edge-type singularities are important features of such wavefronts, corresponding to topological defects of $\varphi(\vec{r}, t)$ [2]. We restrict attention to screw-type phase singularities since, unlike edge dislocations, these are stable with respect to perturbation [2].

The nature of these screw-type phase singularities can be studied using a topological argument which takes as a starting point the smoothness and single-valuedness of the complex scalar wavefield $\psi(\vec{r}, t)$. Single-valuedness implies that over a simple smooth positively traversed closed circuit Γ , over every point of which the intensity of the wavefield is strictly positive, the phase $\varphi(\vec{r}, t)$ may only change by an integer multiple m of 2π [1,6]. Hence

$$\int_{\Gamma} d\varphi = \int_{\Gamma} \nabla\varphi \cdot \hat{\mathbf{u}} \, ds = 2\pi m, \quad (2)$$

where $\hat{\mathbf{u}}$ is the unit vector tangent to Γ and ds is the differential element of arc length along Γ .

If m is non-zero, at least one vortex-type singularity pierces the two-dimensional surface spanning Γ . Here, we consider only first-order vortices ($m = \pm 1$) that are structurally stable and disregard higher-order vortices ($m = \pm 2, \pm 3, \dots$), which are not stable with respect to perturbations [7]. Note that $m=0$ can also correspond to the presence of an equal number of vortices and antivortices; $m=2, 3, \dots$ to several vortices being present; $m = -2,$

* Corresponding author.
E-mail address: freda.r@monash.edu (F. Rothschild).

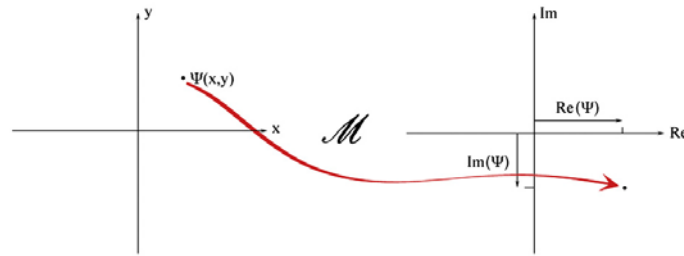


Fig. 1. The Argand mapping of a complex number $\Psi(x,y)$ at a point (x,y) .

–3... to several antivortices being present. The smoothness of the wavefield implies that a vortex can only occur when $\psi = 0$ over at least one point of a two-dimensional surface possessing Γ as a boundary, that is, where the phase φ is undefined. This requires two conditions: that $\text{Re } \psi = 0$ and $\text{Im } \psi = 0$; this implies that phase singularities are lines in space or points on a plane [2]. Nye and Berry [8] refer to these as “wavefront dislocations”, using terminology evocative of crystal dislocations [9]. An important property of vortices is the structural stability with respect to perturbation of the nodal lines which thread them, which may be compared to the stability of certain caustics under perturbation.

Phase singularities in complex scalar fields occur on spatial scales comparable to the wavelength. When the wave is sampled over length scales that are very large when compared to the wavelength, corresponding to the short-wave limit, waves become rays and a different class of singularities arise. As rays have the ability to focus, concentrating their energy onto a point or surface, ray theory predicts regions of infinite intensity known as caustics [2]. These caustic regions can be categorized into various types. For structural stability, one can look to the surface caustic, wherein a family of rays form an envelope, rather than having infinitely many rays passing through a single point. A hierarchy of surface caustics is stable with respect to perturbations and may be classified into a series of equivalence classes known as catastrophes [10]. The mathematical tool needed to explain these phenomena is catastrophe theory, the study of singularities and gradient mappings [2,10]. Examples of caustics are the cusp and the fold. Higher order caustics include the swallowtail and the elliptic umbilic. All of these are stable focal structures generically formed without any need for deliberate optical focussing, hence named ‘natural focusing’ by Hannay, as reported in Nye’s text [11].

In passing from the ray to the wave theory, the caustic surfaces of infinite intensity are softened to peaks. Such softened caustics often form a skeleton that is decorated with phase vortices [2]. A good example of this is the presence of phase vortices in the vicinity of the caustic surfaces predicted by ray theory in the focal volumes of coherently illuminated aberrated lenses [12].

The most obvious complementarity between vortices and caustics is at the level of intensity. On a caustic in a coherent field, there is infinite intensity according to ray theory, whereas on a vortex core, the intensity is zero according to wave theory [2]. These two classes of singularities are not simultaneously observable since they manifest at mutually exclusive length scales [2]. Over length scales that are large compared to the wavelength, singularities of ray theory dominate as the effects of the finite wavelength can be ignored. At this scale, vortices are unresolved. When magnified to a point where effects of a non-zero wavelength are significant and vortices can be seen, the caustic singularities are “smoothed away” by diffraction. In this sense, the measurement of one prevents the measurement of the other.

Such complementarity is present in the concept of wave-particle duality, whereby the wave and particle natures of light are similarly not simultaneously observable. Berry [2, pp. 479–480] draws comparisons on this point, stating that the complementarity of vortices and caustics “must surely embody a deep aspect of the wave-particle duality but I do not know how to exploit it”. This beautiful and deep question, while not directly addressed here, has inspired the work of the present paper.

We close this introduction with an outline of the remainder of the paper. Section 2 introduces the mapping of complex functions, from a two-dimensional plane in space to the Argand plane, which is induced by a two-dimensional complex scalar optical wavefield. This section also describes the condition for formation of an Argand-plane caustic, by such a map. Section 3.1 outlines a method of optical vortex generation, which is based on the filtering of white noise, together with its associated Argand-plane mapping. The resulting coherent speckle fields are used for the numerical simulations in the remainder of the paper. Section 3.2 concentrates on the mapping of vortices in such wavefields to the Argand plane, with Section 3.3 treating the singularities that arise from this mapping, confirming their connection to vortices. The key result of these sections is a certain complementarity between optical vortices in the wavefield and caustics in the Argand-plane map induced by the wavefield: (i) the existence of Argand-plane caustics is a consequence of the existence at least one vortex-antivortex pair in the field; (ii) the number of optical vortices changes when the associated Argand-plane map possesses a caustic which crosses the Argand origin.

2. Singularities of Argand-plane mappings

An arbitrary two-dimensional differentiable continuous single-valued complex function $\Psi(x,y)$ can be considered to induce a map $\mathcal{M} : \mathbb{R}^2 \rightarrow \mathbb{C}$ from two-dimensional real space to the complex plane, given by

$$\mathcal{M}(\Psi(x,y)) \rightarrow \{\text{Re } \Psi, \text{Im } \Psi\}, \quad (3)$$

where $\Psi(x,y)$ represents the boundary value of the spatial part of a forward-propagating monochromatic scalar three-dimensional wavefield over a given planar surface. Note also that coherent scalar fields are assumed in this paper, with harmonic time dependence being suppressed.

Fig. 1 demonstrates the mapping \mathcal{M} of a complex number $\Psi(x,y)$ associated with a single point (x,y) in real space, to a point on the Argand plane. Note that the mapping induced by Ψ , in Eq. (3), can be placed into direct correspondence with a complex scalar function of a complex variable (Fig. 2).

Up to continuous deformation, and to first order in x and y , a vortex at (x_0, y_0) is given by [13]

$$\Psi_{\pm} = (x - x_0) \pm i(y - y_0), \quad (4)$$

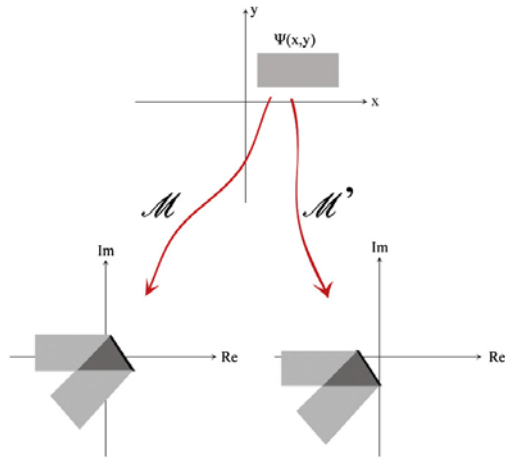


Fig. 2. A complex scalar two-dimensional “patch” $\Psi(x,y)$ transforms under the mapping \mathcal{M} to fold and produce a caustic in the Argand plane, indicated by the dark line. $\Psi(x,y)$ transforms under mapping $\mathcal{M}' = \mathcal{M} + C$, where C is a complex constant that shifts the Argand plane mapping \mathcal{M} such that the caustic crosses the origin.

where an infinitesimal patch at (x_0, y_0) maps under \mathcal{M} to cover the Argand-plane origin, at which $\text{Re } \Psi = 0$ and $\text{Im } \Psi = 0$. Ψ_+ denotes a vortex, with an anti-clockwise phase winding and Ψ_- an antivortex with a clockwise phase winding. The Argand-mapping of such a patch is shown in Fig. 2. The infinitesimal patch at (x_0, y_0) in Ψ_+ maps directly onto the Argand-plane origin; in Ψ_- it must be “flipped” in order to map to the Argand-plane origin. This implies a fold under the mapping \mathcal{M} to the Argand plane, as when there are two vortices of opposite helicity over a simply connected region in the field, the corresponding patches of space will both map to the origin, with one patch flipped relative to one another.

The mapping \mathcal{M} applied to $\Psi(x,y)$ is such that the darker region in Fig. 2 lies across the Argand-plane origin, i.e. two sheets connected by a fold caustic α are covering the origin, implying the presence of two vortices of opposite helicity. The constant C is chosen so that α has crossed over the Argand-plane origin and there are no sheets covering it, and therefore, no vortices or antivortices in the field.

Given that complex wavefield zeroes are generally structurally stable only if they coincide with screw-type phase dislocations, we are led to conclude that the presence of an Argand-plane caustic crossing the origin in the image of \mathcal{M}' will be associated with a change in the number of vortical phase singularities in the wavefield $\Psi(x,y)$ inducing the Argand-plane map. The number of Riemann sheets of $\mathcal{M}(\Psi(x,y))$, at the complex-plane origin, gives the total number of vortices plus antivortices in the phase of $\Psi(x,y)$. Hence when the number of Riemann sheets at the complex-plane origin changes as a caustic (such as a fold) crosses this point, the number of vortical phase discontinuities in $\Psi(x,y)$ will change abruptly.

As a demonstration, let us take the simple example

$$\Psi_1(x,y) = -x^2 + iy, \tag{5}$$

which induces a many-to-one mapping \mathcal{M} . The Argand-mapping of this function results in a fold in the real direction as it is independent of the sign of x . As a result of the requirement that the optical field $\Psi_1(x,y)$ be continuous, a fold caustic will result. In order to control the position of the Argand-plane caustic, a real

constant A is introduced such that

$$\Psi_1(x,y) = A^2 - x^2 + iy; \tag{6}$$

physically, A^2 represents a coherent background signal, namely a plane wave with amplitude A^2 propagating perpendicular to the xy -plane. The Argand-plane mapping corresponding to Eq. (6), as applied to the region $|x| < 10, |y| < 10$, is plotted in Fig. 3a for $A=5$. The phase of this function, determined by the equation

$$\phi = \text{atan}(\text{Im } \Psi_1 / \text{Re } \Psi_1), \tag{7}$$

where $\text{Re } \Psi$ and $\text{Im } \Psi$ denote the real and imaginary parts of Eq. (6), respectively, is shown in Fig. 3b. There, a vortex-antivortex pair is present. The position of these vortices, determined by the fulfilment of the requirement that $\text{Re } \Psi_1 = 0$ and $\text{Im } \Psi_1 = 0$, is also controlled by the parameter A . As $A \rightarrow 0$, the vortices at $(\pm A, 0)$ move closer together, ultimately annihilating one another when $A=0$.

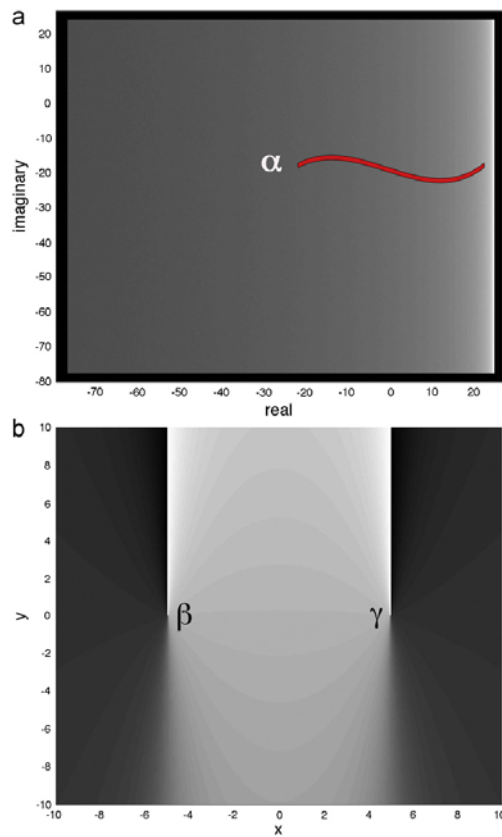


Fig. 3. (a) A histogram of the Argand-plane mapping of the many-to-one function $\Psi_1(x,y) = A^2 - x^2 + iy$ for $|x| < 10, |y| < 10$ and $A=5$. Eq. (6) transforms as a 2D array under \mathcal{M} to result in a fold caustic α located at $\text{Re } \Psi_1 = 25$. The histogram is generated using a Monte Carlo method, where points from the wavefield are sampled and placed in “bins” in the Argand plane. In figure (b) a greyscale image of the phase of the function is shown, where a vortex-antivortex dipole is seen at points β and γ . The positions of these vortices are $(5,0)$ and $(-5,0)$. As A tends to 0, the two vortices will move towards each other, annihilating when $A=0$.

The fold caustic seen in Fig. 3a is a consequence of the two vortices present in $\Psi_1(x,y)$ (seen in Fig. 3b), as was described earlier in relation to Eq. (4) where it was stated that a field that contains a vortex and an antivortex within a simply connected region must fold under the mapping \mathcal{M} to the Argand plane.

Increasing in complexity, we take a second function

$$\Psi_2(x,y) = A^2 - x^2 + i(B^2 - y^2), \quad (8)$$

where A and B are real constants. Solving for $\text{Re } \Psi_2 = 0$ and $\text{Im } \Psi_2 = 0$, we find solutions for vortices at positions (A,B) , $(A,-B)$, $(-A,B)$ and $(-A,-B)$. The Argand mapping for Eq. (8) is shown in Fig. 4a for $A=B=5$. In Fig. 4b, the vortex quadrupole associated with the phase of Eq. (8) as defined by Eq. (7) is shown.

In Fig. 3, it was seen that the x^2 term and the subsequent presence of a vortex–antivortex dipole result in a fold in the real direction when the wavefunction is mapped to the Argand-plane. Therefore, Ψ_2 must have a fold in both the real and imaginary directions, as four Riemann sheets (two corresponding to positive Jacobian, see Eq. (9), and two to negative Jacobian) must cover the

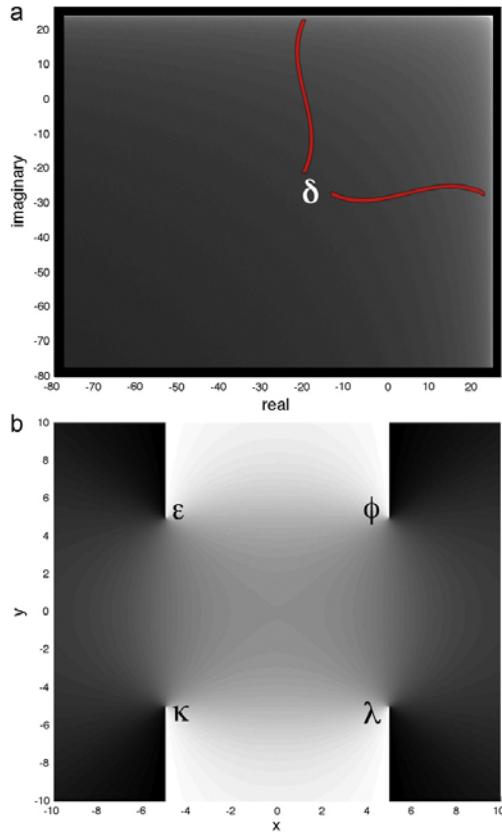


Fig. 4. (a) A histogram of the Argand mapping of the function $\Psi_2(x,y) = A^2 - x^2 + i(B^2 - y^2)$ applied to the region $|x| < 10$, $|y| < 10$ for $A, B = 5$. The presence of a fold caustic is indicated by δ . (b) A grayscale image of the phase map for Ψ_2 , where a vortex quadrupole is seen. The four vortices ϵ , ϕ , κ , λ are $(-5,5)$, $(5,5)$, $(-5,-5)$ and $(5,-5)$, respectively. As $A, B \rightarrow 0$, the vortices will move closer together, ultimately annihilating one another.

Argand-plane origin. In order to view Fig. 4a in a more revealing and structurally stable form, perturbing terms can be added to Ψ_2 to “unfold” the Argand mapping. By adding a y term to the real part Ψ_2 , the Argand-mapping is unfolded in the x direction (Fig. 5a). An additional x term in the imaginary part of Ψ_2 unfolds the Argand-mapping in the y direction (Fig. 5b).

Both Ψ_1 and Ψ_2 are examples wherein a function can be transformed under \mathcal{M} to bring about *Argand-plane singularities*. These Argand-plane caustics are intimately linked to the presence of vortices of opposite helicities in $\Psi(x,y)$, since (i) the existence of vortices of opposite helicities in $\Psi(x,y)$ implies that $\mathcal{M}(\Psi(x,y))$ must cover the Argand-plane origin at least twice, with one image patch at the Argand-plane origin being flipped with respect to at least one other patch mapped to the origin; (ii) the continuity of $\Psi(x,y)$ then implies the inevitable existence of at least once caustic in $\mathcal{M}(\Psi(x,y))$. These points will be explained in more detail in Sections 3.2 and 3.3.

The Jacobian determinant (Jacobian) of the mapping \mathcal{M} is given by

$$J(x,y) = \begin{vmatrix} \partial \text{Re } \Psi(x,y) / \partial x & \partial \text{Re } \Psi(x,y) / \partial y \\ \partial \text{Im } \Psi(x,y) / \partial x & \partial \text{Im } \Psi(x,y) / \partial y \end{vmatrix}. \quad (9)$$

The Jacobian at a point provides important information of Ψ near there. The absolute value of the Jacobian at (x_p, y_p) gives the factor by which Ψ expands or shrinks infinitesimal patches at p , while the sign of J indicates whether or not the image of the patch is flipped ($J < 0$) or not ($J > 0$). A value of $J=0$ indicates that patch areas have “disappeared”, that is, a patch in the xy plane has been collapsed into a single point and a singularity has formed in $\mathcal{M}(\Psi(x,y))$. The Argand-plane singularity can be located by letting $J=0$ and solving for (x_p, y_p) . For the example plotted in Fig. 5b, Eq. (8), with the additional y term in the real part and x term in the imaginary part, is substituted into Eq. (9) and, setting $J(x,y)=0$, gives $y = 1/4x$ for $J=0$. Substituted back into $\Psi_2 + y + ix$, we obtain

$$\Psi_2(x,y = 1/4x) = A^2 - x^2 + 1/4x + i(B^2 - 1/16x^2 + x), \quad (10)$$

which is mapped to the Argand plane in Fig. 5c. The lines correlate with the caustics seen in Fig. 5b.

As every patch of space containing a vortex is required to be mapped to a sheet which lies over the Argand-plane origin, it is evident that the number of sheets lying over the Argand-plane origin as a result of the mapping \mathcal{M} of some complex scalar wavefield corresponds to the number of vortices in the wavefield. The appearance of the fold caustic in the Argand-plane mapping is an inevitability arising from the mapping of a pair of opposite-helicity vortices to the Argand-plane. It is now understood what is special about Argand-plane caustics, such that when $A=0$ for $\Psi_1(x,y)$, causing the fold caustic in Fig. 3a, the vortex–antivortex pair is annihilated: a single fold caustic crossing the origin will result in a change in the number of vortices by two, as the “sheet count” over the Argand-plane origin has changed by two.

The remainder of this paper is a study of the connection between vortices in $\Psi(x,y)$ and associated Argand-plane caustics in $\mathcal{M}(\Psi(x,y))$, exemplified via the spatially random two-dimensional vortical coherent speckle fields arising from spatial filtering of two-dimensional noise. The existence of at least one caustic in $\mathcal{M}(\Psi(x,y))$ will be seen to follow from the existence of at least one vortex–antivortex pair in $\Psi(x,y)$. We shall see that a change in the number of real-space vortices may be associated with a caustic in the corresponding Argand-plane image, when the said caustic approaches the origin of coordinates in the Argand plane. We will see that the locus of (x,y) points with $J=0$ will partition this space into cells containing either vortices of one given helicity or no

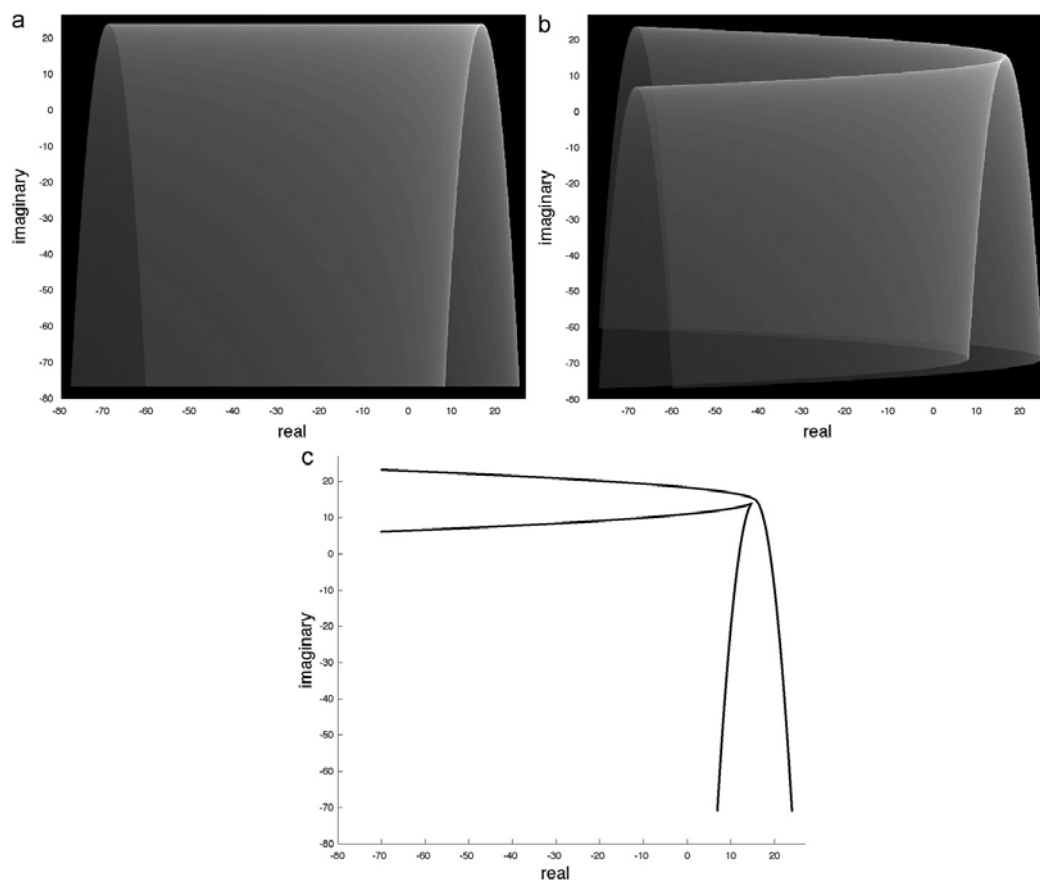


Fig. 5. (a) The Argand-mapping of $\Psi_2(x,y)+y$. The addition of the y term “unfolds” the Argand-mapping of $\Psi_2(x,y)$ in the x -direction, revealing some structure hidden in Fig. 4a. (b) The Argand-mapping of $\Psi_2(x,y)+y+ix$. Now the Argand-mapping is unfolded in both directions. It can be seen that the region $|x| < 10$, $|y| < 10$ has been twice folded. (c) The locations of the caustics in Fig. 5b. This was determined by solving Eq. (9) for $j=0$ and substituting the result back into $\Psi_2(x,y)+y+ix$ to give Eq. (10).

vortices at all, with the interior of each such cell being mapped to the interior of a caustic in the Argand plane. This locus of points with $j=0$, which are mapped to Argand-plane caustics, corresponds to lines of zero vorticity in the field (see Section 3.2 for further information).

3. Duality between vortices in a two-dimensional coherent scalar field, and caustics in the associated Argand-plane map

Several well-known methods exist for vortex generation. He et al., for example, have used a diffractive optical element to produce vortices [14]. Nicholls and Nye [15] as well as Masajada and Dubik [16] have shown that a lattice of phase vortices may result from the interference of three plane waves. This concept has been extended upon using Young’s three-pinhole interferometer [17] and more recently in works that use the interference of a Bose–Einstein condensate (BEC) to generate vortices [18–20]. The three-pinhole interferometer also provides an example of spontaneous vortex generation, where one can superpose a small

number of non-vortical fields (in this case, three spherical waves) to induce vortices instead of having to explicitly “stir” the beam, e.g. with the use of a spiral phase plate [21].

As another method for generating optical vortices, one may scatter coherent plane waves from a spatially random sample, with the resulting speckle field containing a random set of vortices and antivortices [22,23]. We restrict our attention to such vortex-laden random optical speckle fields. Section 3.1 describes a simple method of vortical speckle-field generation that uses spatial filtering of two-dimensional noise. Section 3.2 discusses the relationship between vortices and the Argand-plane mapping \mathcal{M} of the random two-dimensional complex scalar wavefield, in the context of the previously described “noise filtering” method for vortex generation. Section 3.3 looks at the caustic-like structures that are generated as the wavefield is transformed under \mathcal{M} , as certain control parameters in the noise filtering method of vortex generation are varied. This section also discusses the duality between vortices in a two-dimensional coherent scalar field, and caustics in the associated Argand-plane map.

3.1. Method for generating vortices via noise-filtering

One particular method for vortex generation involves the filtering of two-dimensional delta-correlated complex white noise. This may be achieved using visible light by passing a coherent plane wave through a static ground glass plate and then spatially filtering the resulting exit-surface wavefield using a circular Fourier-plane filter in the back focal plane of an imaging system placed downstream of the glass plate. A schematic of an optical experiment which could be used to implement this is shown in Fig. 6.

To computationally model this process, a random two-dimensional complex scalar wavefield, $\Psi_{noise}(x,y)$, was simulated over a Cartesian grid. Uniformly randomly generated intensity $I(x,y)$ and phase $\phi(x,y)$ values were created at each pixel in this grid, combined using

$$\Psi_{noise}(x,y) = \sqrt{I(x,y)} \exp[i\phi(x,y)], \quad (11)$$

with random deviates for both the intensity and phase being drawn from a uniform probability distribution with $0 \leq I(x,y) \leq 1$ and $0 \leq \phi(x,y) \leq \pi$.

The two-dimensional fast Fourier transform (FFT) of the simulated wavefield, denoted $\tilde{\Psi}_{noise}(k_x, k_y)$ was truncated using a low-pass filter $\mu(k_x, k_y)$ with cutoff κ

$$\mu(k_x, k_y) = \begin{cases} 1 & \text{for } \sqrt{k_x^2 + k_y^2} \leq \kappa, \\ 0 & \text{elsewhere,} \end{cases} \quad (12)$$

where (k_x, k_y) are Fourier coordinates corresponding to (x,y) . The

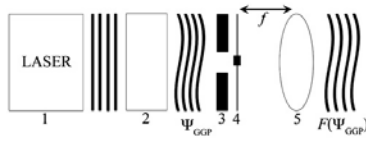


Fig. 6. Schematic of experiment to generate vortices using noise filtering. Coherent light is produced using a laser (1), propagating through a ground glass plate (2), with the emerging complex field denoted Ψ_{GGP} . The wavefunction Ψ_{GGP} then passes through a circular iris with varying radius r (3). To filter out the zero-frequency component, a plate of glass with a darkened spot at the centre is placed in front of the circular iris (4). The filtered wavefunction that emerges from the glass passes through a lens with focal length f (5).

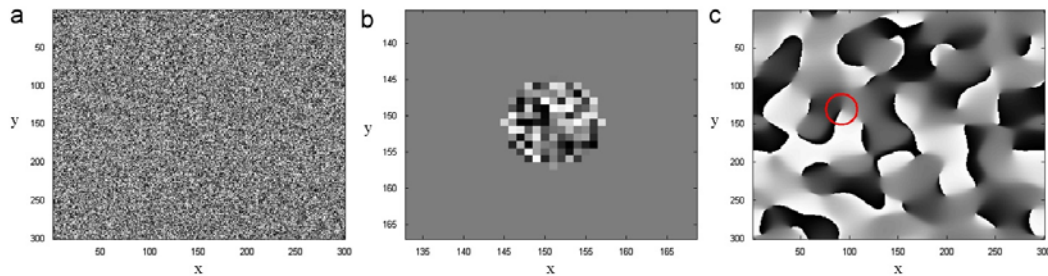


Fig. 7. Filtering two-dimensional complex white noise to generate phase vortices: (a) grid of 300×300 pseudo-random numbers uniformly generated between 0 and π , representing the phase of a two-dimensional complex scalar wavefield. A phase of $-\pi$ is indicated by black, π by white. A similar “white noise” map of intensity values (not shown) was also generated. These were combined using Eq. (11) in Fourier space to give a complex wavefield which is then multiplied by a circular mask of radius $\kappa = 6$ pixels with a value of 0 outside and 1 inside the mask. The effect of the mask is shown in the zoomed-in phase map image in (b). By implementing an inverse Fourier transform, filtering the DC component by a factor of $\tau = 0$, the resulting complex field, whose phase is given in (c), becomes littered with phase vortices with average separation scaling as $1/\kappa$. One antivortex is circled in (c).

above filter was augmented by the mask:

$$\mathcal{A}(k_x, k_y) = \begin{cases} 1 & \text{for } \sqrt{k_x^2 + k_y^2} > \kappa_{small}, \\ \tau & \text{elsewhere,} \end{cases} \quad (13)$$

where $\kappa_{small} < \kappa$ is the radius of the small absorbing disc with real transmission coefficient τ that is centered over the Fourier-space origin. This second mask corresponds to a form of dark-field imaging in which the lowest Fourier components of the imaged wavefield were suppressed by a factor of τ . The complete expression for the method for generating vortices via noise filtering is therefore

$$\mathcal{F}^{-1}[A(k_x, k_y)\mu(k_x, k_y)\tilde{\Psi}_{noise}(k_x, k_y)], \quad (14)$$

where \mathcal{F}^{-1} denotes inverse two-dimensional Fourier transformation.

A simulation of the filtering process is shown in Fig. 7 (see caption for associated numerical parameters). We have chosen κ_{small} to represent the filtering of a single pixel located at the Fourier-space origin, i.e. the zero-spatial-frequency component (DC frequency component).

3.2. Mapping of vortices to the Argand plane

When the real and imaginary parts of the spatially random wavefield in Fig. 7c are mapped to the Argand plane under \mathcal{M} , as shown in Fig. 8, the resulting image of the mapping contains a series of caustic structures. These are much like Fig. 5b, but are more complicated here due to the increased complexity of the field $\Psi(x,y)$ that is being transformed. Fig. 8 demonstrates the dependency of the vortex density and caustic-structure of the Argand plane on the parameter κ in the Fourier-filtering process. The larger the cutoff radius κ of the circular mask, the smaller the characteristic length scale $1/\kappa$ of the resulting random speckle field and hence the more phase vortices are likely to be present. As a result of this, the more richly structured will be the image of the mapping \mathcal{M} of the wavefunction in the Argand plane. The low-pass filter cutoff κ is a parameter whose increased value may lead to higher-order singularities in the Argand plane. We see that the number of vortices increases with κ , as shown in column (ii) of Fig. 8. Via dimensional reasoning, the relationship between the maximum vortex density ρ_{max} and the low-pass cutoff filter κ is given by $\rho_{max} = \kappa^2$.

On the other hand, the dark-field attenuation parameter τ , while also affecting the number of vortices in the two-dimensional wavefield, does not change the form of the image of the map in the Argand plane in the same way that κ does, but

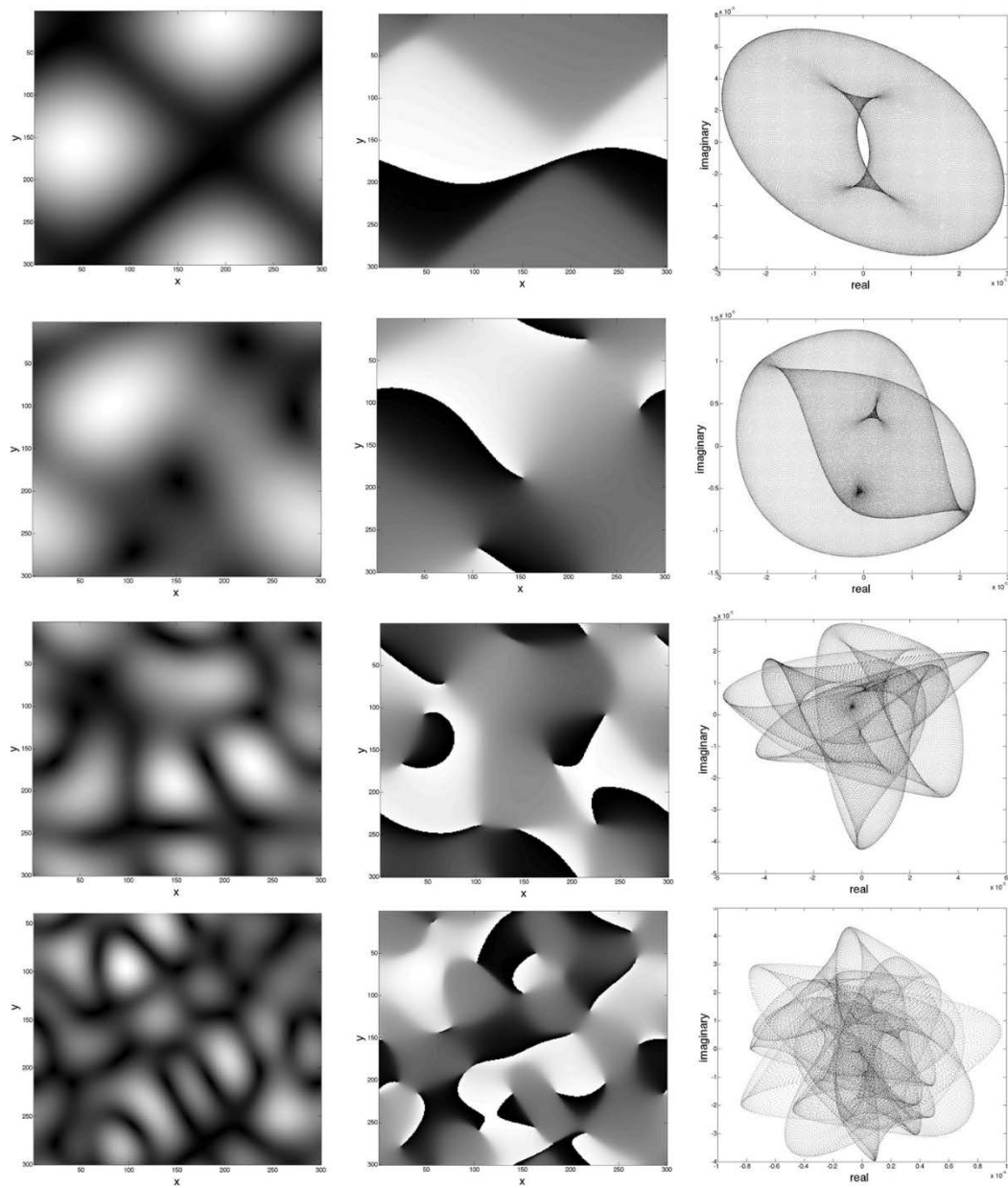


Fig. 8. Columns (i), (ii) and (iii) show the intensity, phase and Argand-plane mapping of a vortical two-dimensional complex scalar speckle wavefield for $\tau = 0$ and grid size of 300×300 pixels, respectively. Successive rows show how the images evolve as the maximum filtering frequency κ is increased. The values for κ are (a) 1.5, (b) 2, (c) 8 and (d) 16. The Argand-plane caustics that appear in (iii) and the vortices present in (ii) increase in complexity as κ is increased.

only displaces its position in the Argand plane (provided that the non-negative real number κ_{small} is sufficiently small). This Argand-plane translation is shown in Fig. 9.

Although the change in the Argand plane is trivial, τ , as mentioned, has an effect on the number of vortices. For all the simulations performed, when $\tau = 1$, no vortices are present in the

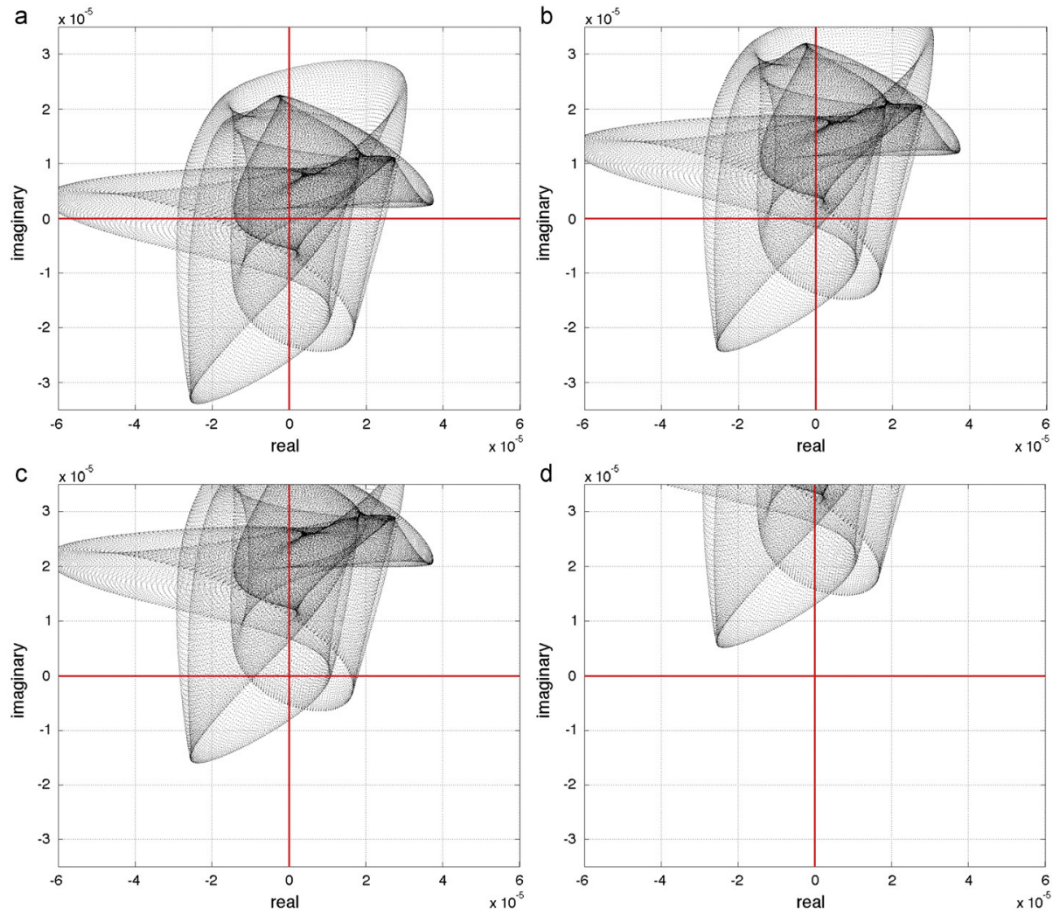


Fig. 9. (a) through (d) show the mappings of a vortical two-dimensional complex scalar wavefield in the Argand plane for a mask size of $\kappa = 6$ pixels on a grid of 300×300 pixels. The parameter τ is increased: 0.003 in (a), 0.012 in (b), 0.02 in (c) and 0.04 in (d), each time shifting the mapping by a complex constant until the mapping is completely off the origin, which is marked by red lines. (For interpretation of the references to colour in this figure caption, the reader is referred to the web version of this article.)

field and when the DC component is completely removed, i.e. when $\tau = 0$, vortices are present.

Knowing now that the effect of the addition of a constant complex number, which comes about via the filtering of the DC by a factor of τ , is to shift the Argand mapping of the wavefield, we can explain the dependency of vortex density on τ . Filtering the zero-frequency component by some factor adds a constant complex number to the wavefield which subsequently shifts its mapping \mathcal{M} in the Argand plane. As mentioned in Section 2, for every vortex in the wavefield, there will be a corresponding “sheet” lying over the Argand-plane origin; the number of Riemann sheets covering the Argand-plane origin, in each panel of column (iii) in Fig. 8, therefore gives the total number of vortices plus antivortices.

To illustrate this, in Fig. 10a we plot the number of vortices N embedded in a complex two-dimensional wavefield versus τ (see caption of Fig. 10 for associated numerical parameters). A vortex can be detected by searching for points that satisfy the

requirement that $|\Psi_R|, |\Psi_I| < \epsilon$, where the tolerance ϵ is 10^{-7} . Additionally, we must maintain that the phase changes by a multiple of 2π around this point as described by Eq. (2). The result is a plot consisting of highly singular peaks (Fig. 10a).

The presence of peaks, corresponding to a change in the number of zeros, is entirely consistent with the claim in Section 2, which stated that a caustic fold singularity crossing the origin in the Argand plane will result in a change in the number of vortices by two. That is, two sheets will disappear from or appear at the origin, depending on the direction that the Argand-plane mapping is travelling as τ changes.

To obtain an ensemble average of Fig. 10a, the previously fixed random seed was allowed to vary randomly. 3000 random realizations of a two-dimensional complex scalar wavefield were generated, and the ensemble average of N for each value of τ was calculated. A plot of the average number of vortices versus τ is shown in Fig. 10b. The shape of the plot in Fig. 10b was fitted to a

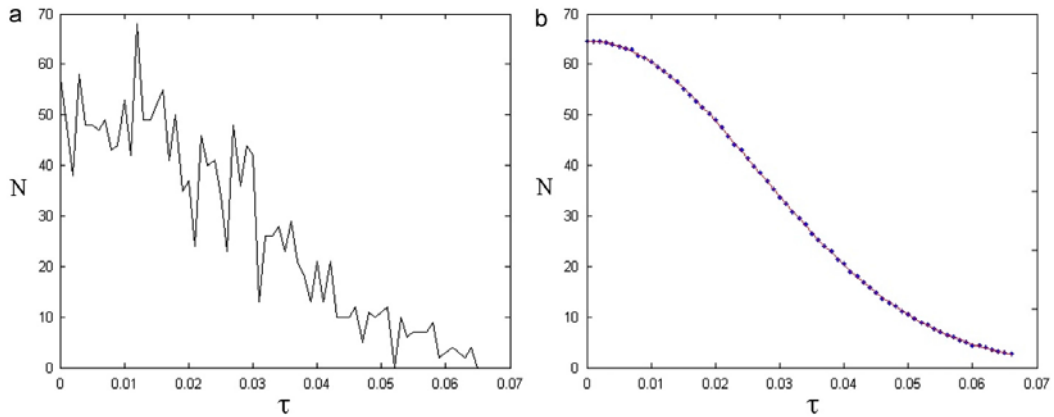


Fig. 10. The number of vortices N in a 484×484 two-dimensional complex scalar wavefield versus τ for $\kappa = 80$. τ was varied between 0 and 0.067 in increments of 0.0001. Shown is (a) a single realization; (b) an ensemble average of 3000 realizations. Certain values of τ result in peaks in the number of vortices in (a) that correspond to one or more fold caustics crossing the origin. Although a single realization appears highly structured, the sum of 3000 is relatively structureless, monotonically decreasing and Gaussian. The set of points is fitted to a Gaussian curve (red) with $\chi^2 = 0.9607$. (For interpretation of the references to colour in this figure caption, the reader is referred to the web version of this article.)

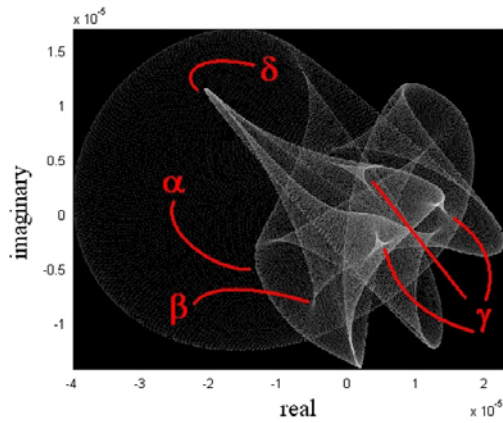


Fig. 11. Argand mapping of a randomly generated wavefield with a grid of 400×400 and parameters $\tau = 0$, $\kappa = 6$, 400×400 bins. A rich variety of structurally stable caustics is observed. The presence of a fold caustic, denoted α and a cusp, β , is indicated as well as higher-order singularities, the elliptic umbilics, γ , and hyperbolic umbilic, δ [26,11].

Gaussian curve that appears as a red line, with goodness-of-fit $\chi^2 = 0.9607$. This result is consistent with the analysis by Goodman [24, Section 4.8.4].

3.3. Structure of Argand-plane caustics associated with a coherent vortex-field

Consider the plot in Fig. 11, which shows the mapping of a random vortex-laden speckle field (produced using the method described in Section 3.1) to the Argand-plane, with the said speckle field generated using the parameters specified in the caption. Note that, unlike the mappings in both the right column of Fig. 8 and in all panels of Fig. 9, the map in Fig. 11 is plotted using a histogram with logarithmic scaling, to better reveal the rich variety of

caustics present there. The structurally stable caustics in this mapping include the fold α , the cusp β , the elliptic umbilics γ and the hyperbolic umbilic δ .

In Section 2 we argued that for a vortex–antivortex pair, the infinitesimal patches of space surrounding the vortex and antivortex will be respectively mapped to cover the Argand-plane origin, with the respective image patches being flipped with respect to one another. Intuitively, this implies the existence of at least one caustic in the Argand-plane image of any simply connected region, which contains at least one vortex and at least one antivortex. The proof of this statement is as follows: (i) consider a simply connected region Ω in (x,y) space which contains at least one distinct vortex and antivortex. Let any one vortex be located at A , and let an antivortex be located at B . (ii) The associated Jacobian J (see Eq. (9)) for the induced Argand-plane map will be positive at the location of the vortex, and negative at the location of the antivortex. (iii) Now connect A to B with a continuous line Γ , each point of which lies within Ω . The possibility of this construction is guaranteed by the simply connected nature of Ω . (iv) Under the assumption that both $\Psi(x,y)$ and its first partial derivatives are continuous, which will automatically be satisfied for coherent scalar waves in free space obeying a second-order differential field equation, J will be a continuous function of position along Γ . Since J varies continuously as one moves from A to B along Γ , and since J changes sign in moving from A to B , the intermediate-value theorem of mathematical analysis implies that J will be zero for at least one point on Γ . This point of zero Jacobian will be mapped to a caustic in the Argand plane. Hence we have proved the required result: at least one caustic exists in the Argand-plane image of any simply connected region which contains both at least one vortex and at least one antivortex. Note also that, if Ω is never infinitely thin at any point, then the set of points where $J=0$ must form at least a one-dimensional manifold which cuts Ω into disconnected pieces, one of which contains A and the other of which contains B . This latter point is readily proved by considering the set of all possible contours Γ in the above argument.

Note that the locus of points for which $J=0$ [25], in the xy plane, will partition the space into a connected set of cells, each of which will either contain no vortices or only vortices of a given

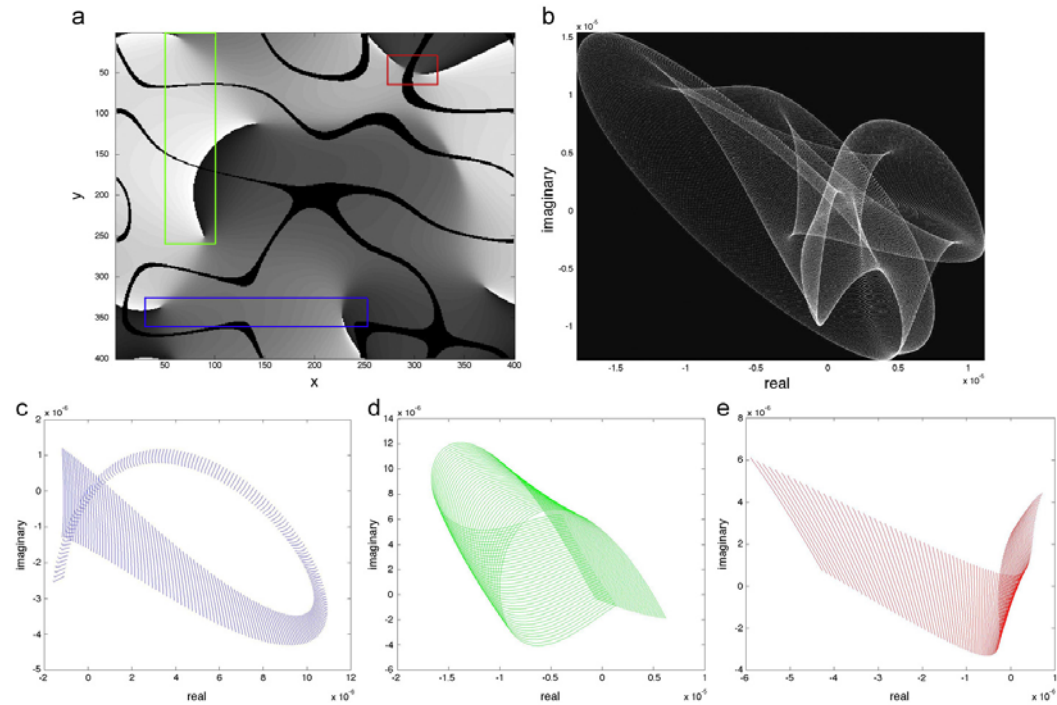


Fig. 12. (a) A 200×200 pixel grayscale image of the phase of a randomly generated wavefield for $\tau = 0$ and $\kappa = 4$. The black lines represent points where the magnitude of the Jacobian (see Eq. (9)) is smaller than a specified tolerance $\epsilon = 0.5 \times 10^{-9}$. (b) A 400×400 -bin logarithmic histogram of the Argand-plane mapping of the same field; (c), (d) and (e) are Argand mappings of the regions bound by the blue, green and red loops in (a), respectively. (For interpretation of the references to colour in this figure caption, the reader is referred to the web version of this article.)

helicity. Moreover, the manifold of xy points with zero Jacobian will be mapped to Argand-plane caustics, with the interior of each such cell being mapped to a region bounded by the caustic image of its “perimeter” (i.e. the set of points with $J=0$ which bounds a given cell). To give physical meaning to the set of points for which $J=0$, note that these correspond to points of vanishing vorticity, since the Jacobian in Eq. (9) is proportional to the z -component of the curl of the Poynting vector $k(\partial\varphi/\partial x, \partial\varphi/\partial y)$.

To illustrate the above points, consider the simulation in Fig. 12, derived from a speckle field obtained using the method of Section 3.1, with parameters as specified in the caption. The grayscale component of Fig. 12a shows the phase of the resulting speckle field (folded modulo 2π), with several vortices and antivortices evident as branch points in the phase function. Overlaid on this are black pixels, which represent areas where $|J| < \epsilon = 0.5 \times 10^{-9}$, as determined via a first-order symmetric finite difference approximation to Eq. (9). As previously stated, the regions where $J=0$ are regions of the field that are mapped to caustics in the Argand plane, as shown in Fig. 12b. The “zero-Jacobian” lines in Fig. 12a segregate vortices of different-sign charges, allowing the image under \mathcal{M} to fold (or exhibit other caustic morphologies, as appropriate) so that the infinitesimal patch containing each vortex is mapped to the origin of the Argand plane with the correct orientation.

The areas enclosed within the blue, green and red strips in Fig. 12a are mapped to the Argand-plane images shown in Fig. 12c, d and e, respectively. (i) The blue rectangle encloses two vortices of the same

charge, with no points of zero Jacobian contained within this region. Hence there are no caustics in the Argand-plane map shown in Fig. 12c, which loops from the origin and back, such that the image of the patch surrounding each vortex contributes one “sheet” covering the origin. (ii) The green rectangle in Fig. 12a encloses two antivortices of the same charge, with two zero-Jacobian lines lying between them. This pair of zero-Jacobian lines is mapped to a pair of fold caustics in Fig. 12d, across each of which the orientation of the map reverses. Two reversals of the sense of the mapping, one at each fold, allows the Argand plane image to cover the origin twice, as it must for two antivortices. (iii) The red rectangle encloses a vortex-antivortex pair and predictably folds when mapped to the Argand plane, as shown in Fig. 12e. Examples (ii) and (iii) manifest a form of vortex-caustic duality, in the sense that the presence of vortex structures is directly tied to the presence of associated Argand-plane caustics. From a physical perspective, this corresponds to the inevitable presence of zero-vorticity points, in a complex scalar wavefield $\Psi(x,y)$, contained within a simply connected region, which contains both vortices and antivortices.

Let us return to a point made in the third paragraph of this subsection, that a two-dimensional cell bounded by a line of zero Jacobian may contain no vortices. An illustration of this is given in Fig. 13(a), which shows a map of the phase of a random two-dimensional coherent scalar wavefield, generated for $\kappa = 4$ and $\tau = 0$. The corresponding zero-Jacobian regions enclosing no vortices are seen in three places, one of which is bounded by a blue rectangle. The Argand-plane map, of the region bounded by this blue rectangle, is

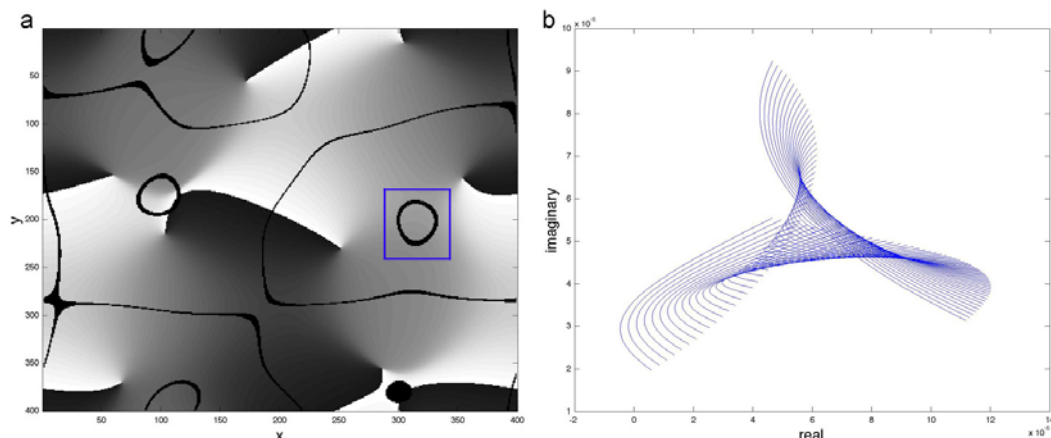


Fig. 13. (a) A 200×200 pixel greyscale image of the phase map of a randomly generated two-dimensional wavefield for $\kappa = 4$ and $\tau = 0$. The black lines represent points where the magnitude of the Jacobian (see Eq. (9)) is smaller than a specified tolerance $\epsilon = 0.5 \times 10^{-9}$. The blue rectangle encloses a ‘‘Jacobian circle’’ and is mapped to the Argand plane in (b) to form an elliptic umbilic catastrophe. (For interpretation of the references to colour in this figure caption, the reader is referred to the web version of this article.)

shown in Fig. 13(b). This shows that, for this example, the ‘‘Jacobian circle’’, which bounds a cell containing neither vortices nor antivortices, is mapped to an elliptic umbilic catastrophe.

4. Conclusion

We have studied the Argand-plane maps induced by vortical two-dimensional complex scalar fields defined over a simply connected region. When such a field contains at least one distinct vortex and antivortex, the associated Argand-plane map will contain at least one caustic. The locus of real space points with Jacobian $J=0$, which corresponds to lines of zero vorticity, will partition the space into cells that contain either no vortices or only vortices of a given helicity. The boundary of each such cell is mapped to a caustic, and the number of patches covering the Argand-plane origin gives the total number of vortices plus antivortices. This investigation on the utility of the Argand plane in analysing vortical optical wavefields provides (i) an interesting new environment for studying catastrophes, and (ii) an interesting connection between vortices in an optical field, and caustics in the induced Argand-plane map.

Note added in proof

There are many extensions of the basic ideas presented in this article to other systems. Examples include the mapping of the gradient of the intensity onto its dx - and dy - components. Additionally, the extension of such mapping to higher dimensions as well as to other manifolds may lead to new connections between Morse theory and catastrophe theory. The authors are grateful to the anonymous reviewer for these suggestions, and will explore these connections in a future publication.

Acknowledgements

FR acknowledges assistance from Dr Gary Ruben and thanks Professor Sir Michael Berry for his interest in the concepts

discussed in this paper and for interesting discussions. FR also acknowledges funding from the Monash University Faculty of Science Dean’s Scholarship scheme. DMP and MJK acknowledge financial support from the Australian Research Council. MJK is an Australian Research Fellow.

References

- [1] P.A.M. Dirac, Proceedings of the Royal Society of London. Series A 133 (1931) 60.
- [2] M.V. Berry, Singularities in waves, in: R. Balian, M. Kléman, J.P. Poirier (Eds.), Les Houches Lecture Series Session XXXV, North-Holland, Amsterdam, 1981, pp. 453–543.
- [3] L. Allen, H. Faulkner, M. Oxley, D. Paganin, Ultramicroscopy 88 (2001) 85.
- [4] H.S. Green, E. Wolf, Proceedings of the Physical Society A 66 (1953) 1129.
- [5] M. Nieto-Vesperinas, Scattering and Diffraction in Physical Optics, Wiley, New York, 1991.
- [6] D.M. Paganin, Coherent X-Ray Optics, Oxford University Press, Oxford, 2006.
- [7] I. Freund, Optics Communications 159 (1999) 99.
- [8] J.F. Nye, M.V. Berry, Proceedings of the Royal Society of London. Series A 336 (1974) 165.
- [9] C. Kittel, Introduction to Solid State Physics, 8th edition, Wiley, Berkeley, 2005.
- [10] R. Thom, Structural Stability and Morphogenesis: An Outline of a General Theory of Models, W.A. Benjamin, Oxford, 1975.
- [11] J.F. Nye, Natural Focusing and Fine Structure of Light, Institute of Physics, London, 1999.
- [12] A. Boivin, J. Dow, E. Wolf, Journal of the Optical Society of America 57 (1967) 1171.
- [13] M.R. Dennis, K. O’Holleran, M.J. Padgett, Progress in Optics 53 (2009) 293.
- [14] H. He, M.R. Heckenberg, H. Rubinsztein-Dunlop, Journal of Modern Optics 42 (1995) 217.
- [15] K.W. Nicholls, J.F. Nye, Journal of Physics A: Mathematical and General 20 (1987) 4673.
- [16] J. Masajada, B. Dubik, Optics Communications 198 (2001) 21.
- [17] G. Ruben, D.M. Paganin, Physical Review E 75 (2007) 066613.
- [18] G. Ruben, D.M. Paganin, M.J. Morgan, Physical Review A 78 (2008) 013631.
- [19] D.R. Scherer, C.N. Weiler, T.W. Neely, B.P. Anderson, Physical Review Letters 98 (2007) 110402.
- [20] G. Ruben, M.J. Morgan, D.M. Paganin, Physical Review Letters 105 (2010) 220402.
- [21] M.W. Beijersbergen, R.P.C. Coerwinkel, M. Kristensen, J.P. Woerdman, Optics Communications 112 (1994) 321.
- [22] M.V. Berry, Journal of Physics A: Mathematical and General 11 (1978) 27.
- [23] M.J. Kitchen, D.M. Paganin, R.A. Lewis, N. Yagi, K. Uesugi, S.T. Mudie, Physics in Medicine and Biology 49 (2004) 4335.
- [24] J.W. Goodman, Speckle Phenomena in Optics: Theory and Applications, Roberts and Co., CO, 2007.
- [25] M.V. Berry, Journal of Optics A: Pure and Applied Optics 11 (2009) 094001.
- [26] M.V. Berry, Personal correspondence, September 2009.

Chapter 3

A study of Argand-plane vorticity singularities using optical speckle

3.1 Introduction and background theory

3.1.1 The generation and manipulation of optical speckle

In the paper presented in Sec. 2.2, optical speckle was simulated with the goal of studying the resulting vortex population and its connection to Argand-plane vorticity singularities. Here, optical speckle is generated experimentally for the same purpose. There are many methods that can be used to generate optical speckle so that it can be studied. Aksenov et al. (1998), for example, generated a speckle field by passing an optical beam through an inhomogeneous medium. A method of generating speckle might incorporate a means of precisely controlling the size and/or position of the speckle so that we could better study it. Pascucci et al. (2016) generated a speckle pattern by passing a beam through a random phase mask and used the handedness of a circular polarizer to change the position of the dark speckle.

An example of a simulated speckle field is shown in Fig. 3.1. Figure 3.1(a) shows a representation of lungs, comprised of 23,600 air-filled spheres with a mean diameter of $60.0 \mu\text{m}$. The diameter of each sphere is randomly generated using Poisson statistics; the position is randomly generated using a uniform distribution, with a limit on the maximum

number of spheres allowed in the projection owing to the thickness of the sample (11.3 mm). Using the angular spectrum formalism, the sample is numerically ‘illuminated’ by 34 keV x-rays, which are then allowed to propagate. One metre from the sample, a speckle pattern is visible, as seen in Fig. 3.1(b).

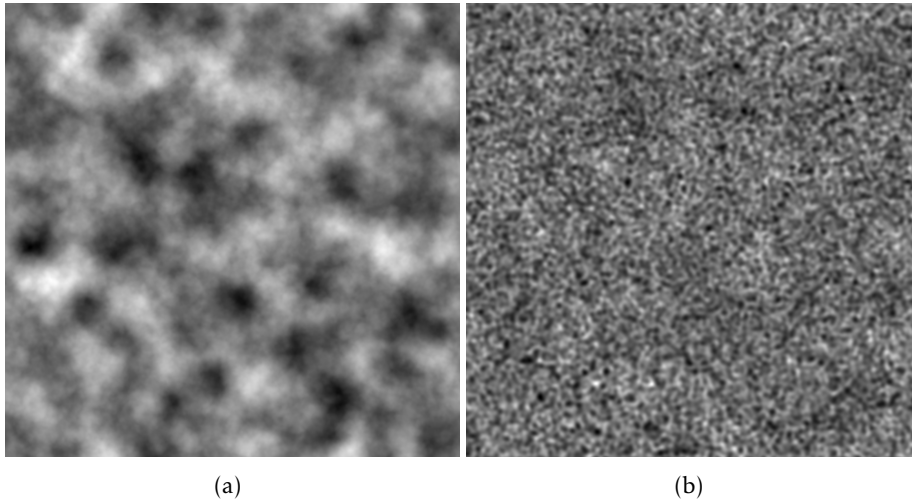


Figure 3.1: Following Kitchen et al. (2004); (a) a simulated contact image of the exit surface of a 11.3 mm-thick lung sample containing 23,600 air sacs with a mean diameter of 60.0 μm illuminated by 34 keV x-rays, and (b) a numerically simulated speckle field obtain by propagating the image in (a) by 1.0 m using the angular spectrum formalism shown in Sec. 2.1.3.

The method used to generate speckles experimentally in Sec. 3.2 involved adapting the numerical approach used in Sec. 2.2. There, white noise underwent a Fourier transform so that higher frequencies could be filtered out from the noisy wavefield. This had the effect of producing larger speckles upon the implementation of an inverse Fourier transform. The size of the speckle was seen to be inversely proportional to the size of the mask placed on the power spectrum of the noisy field.

A detailed schematic corresponding to the experimental set-up used to produce the speckle field is given in Sec. 3.2. There, a collimated optical beam was propagated through a ground-glass screen, a method which has the effect of introducing amplitude fluctuations into a beam that we call noise. In the interest of limiting the number of optical elements used in the experimental implementation of the numerical method of Sec. 2.2, it was noted that as white noise has within it an equal power distribution of all frequencies, the Fourier transform of white noise will be white noise. This noisy beam, which is essentially the two-dimensional spatial frequency spectrum of white noise, was then incident on

a circular iris. In passing through this aperture, the radius of which can be precisely controlled, higher spatial frequencies were removed. An inverse Fourier transform was then implemented with the use of a lens, invoking the Fourier transform properties of lenses, which tells us that if the transmissive object, in this case the circular iris, is placed one focal length in front of a lens of focal length f , then its Fourier transform will form one focal length behind the lens (Goodman, 2005). The resulting speckle field was received by a detector. The diameter of the circular iris was inversely proportional to the size of the individual speckle. If the speckles are associated with vortices, then the circular iris is a means by which to control the number of vortices.

Generally speaking, the number of vortices in an optical beam can be varied by adjusting some external parameter that the wave depends on. As mentioned earlier, Sec. 2.2 investigates the connection between the presence of vortices in a simulated wavefield and the singularities induced by its Argand-plane mapping, and the publication in Sec. 3.2 explores this experimentally. Coming back to Eq. 1.3.2 of Chapter 1, singularities are formed along lines where the Jacobian is equal to zero¹. Knowing this, we can divide the external parameters that can adjust the vortex population into two categories: trivial and non-trivial parameters. A trivial parameter is designed to change the number of vortices while only rigidly shifting the positions of the singularity lines, and a non-trivial parameter changes their overall form. When a wave depends on a non-trivial external parameter, higher-order vorticity singularities can occur. This effect was demonstrated numerically through Fig. 8 of the publication inserted into Sec. 2.2.

An example of a parameter that adjusts the singularity lines in a non-trivial fashion is the propagation distance. In the experimental scheme devised in Sec. 3.2 and described above, the size of the circular iris represents a non-trivial external parameter with regards to the singularity lines. Rather than simply rigidly shifting the speckle pattern, changing the size of the iris changes the size of the speckle itself and consequently the number of speckles within the region of interest, altering the field in a non-trivial fashion. This device can therefore be used to induce higher-order vorticity singularities.

¹Physically, these lines correspond to lines of zero vorticity, a point discussed further in Sec. 3.2. Berry demonstrates such lines in Fig. 2 of his 2009 paper.

An arbitrary complex constant that could be imparted onto the wave, rigidly shifting it while changing only the position of the singularity lines, would suffice as a trivial parameter. In the experiment, this is done by using a Mach-Zehnder interferometer to add a phase term onto the vortex beam, the details of which are explained fully in Sec. 3.2. As with the Mach-Zehnder set up of Fig. 2.2, a reference beam was split off from the main beam. Incorporated into the reference beam were optical elements designed to introduce phase shifts before recombining the two arms of the interferometer.

The detector that is situated at the end of the vortex beam enabled a measurement of intensity only. In order to reconstruct the entire wavefield, it was necessary to measure the phase of the beam as well as the intensity.

3.1.2 The phase problem

In the field of imaging, there is often a loss of information that occurs when making a physical measurement regarding the phase. Detectors, like the CCD camera used in the experiment described in Sec. 3.2, are only able to measure the intensity of light, which is related to its magnitude. This is not a complete measurement of the information contained in the beam; light has also a phase which carries with it important information e.g. about an object which it has passed through. Due to the rapidly oscillating nature of the wavefield at higher frequencies, the phase can not be directly measured (at lower temporal frequencies, microwaves for instance, modern technology can directly measure the phase). There are several, largely uncomplicated techniques that exist for the interferometric recovery of phase with visible-light optics due to the ease with which one can obtain a coherent visible light source and the abundance of optical elements suitable for visible light, such as mirrors and lenses. The problem is far more difficult in x-ray physics as x-ray lasers and optical elements suitable for use with x-ray radiation are difficult to come by, and in some cases do not yet exist. Solutions to the phase problem for these higher temporal frequencies will be discussed in the following chapter.

The phase problem falls under the category of an ‘inverse problem’. Generally speaking, a forward, or direct problem, seeks to determine the effect from a given cause, while an inverse problem attempts to deduce the cause from a given effect. In the context

of imaging, a forward problem takes as its input the model of an object, returning the imaging data that results from the object model and its interaction with a source and detector. This class of problem forms the basis of the results of the publication in Sec. 2.2, where the appropriate mathematical method is used to map the given model, in this case white optical noise, to the desired data. Additionally, solutions to forward problems feature throughout the remainder of this thesis, largely as a means to extrapolate data beyond the general capabilities of the experimental hardware.

An inverse problem involves the determination of information about an object from its imaging data. As the map from the data to the model does not necessarily exist, it is in general a far more difficult problem than its associated forward problem. In order to construct an algorithm for an inverse problem, one must possess a detailed knowledge of the associated forward problem and consider the existence and uniqueness of a solution as well as the stability of the retrieved information with respect to perturbations of the input data (Paganin, 2006).

Hadamard (1923) suggested that a mathematical model of a physical phenomenon should be such that a solution exists that is unique and changes continuously with the initial conditions. If an inverse problem possesses such a solution, it is considered ‘well-posed’, in the sense of Hadamard. Otherwise, it is considered ‘ill-posed’. A problem can be ill-posed because no solution exists or because non-unique solutions exist which cannot be distinguished from one another. In order to proceed and render the problem well-posed, extra data and/or *a priori* knowledge is required. Alternatively, one can approach an ill-posed problem statistically, using the ‘Bayesian’ class of methods. There, a statistical probability is assigned to each possible solution, and the solution with the highest probability of being correct is chosen, within a given model. For more detail see Paganin (2006) and references therein. More on solutions to ill-posed inverse problems is included in the next chapter, in the context of phase retrieval for x-ray imaging.

Given that the detector in an imaging system is only able to record intensity, one solution to the phase problem in this context is to deliberately introduce phase shifts into the beam that are visible as intensity variations. The most famous method of doing so is known as ‘interferometry’, a family of techniques whereby waves are superimposed to obtain

information about them. The result of the superposition is an interferogram, described previously in Sec. 2.1.2.

Interferometers can be categorized as either ‘double path’ or ‘common path’. For a double-path interferometer, the reference beam travels along a path that is separated from the sample. The Mach-Zehnder (Masi et al., 2012) set-up is an example of this, as is the Michelson (Hettwer et al., 2000) interferometer and the Twyan-Green interferometer (Novak et al., 2005). Common-path interferometers have both beams traveling along the same path. The Sagnac interferometer (Lo et al., 2005) and the fibre-optic gyroscope (Lefevre and M. Turpin, 1990) are examples of this. A double path interferometer was implemented into the experimental set-up described in Sec. 3.2 as it allowed the introduction of phase shifts into the reference beam for the purpose of both phase-stepping interferometry and trivial manipulation of vortex numbers.

Phase-shifting, or phase-stepping interferometry (PSI) is a highly efficient method of phase recovery for visible light that is adopted in the work of Sec. 3.2. The integration of computers into the measurement of optical hardware has allowed PSI to be optimised and mainstreamed. This is not just a hardware configuration, but a method in data collection and analysis, making deliberate phase shifts to produce several interferograms that are then combined in an algorithm to recover the phase of the original beam. The advantage of PSI is that it is not dependent on finding fringe centres. Additionally, it is not sensitive to variations in spatial intensity or detector sensitivity. This stands in contrast to methods that involve the analysis of single static interferograms. While these methods have also improved with the use of computers, it requires the locating of fringe centres. Additionally, as data is only collected as fringe centres, there is low spatial sampling. These problems are eliminated with PSI. There are many different methods of phase-shifting interferometry (see e.g. Schreiber and Bruning, 2006). The method used in Sec. 3.2 is a four-step algorithm described by Schreiber and Bruning (2006), and derived below.

To find an expression for the interferograms that are used to recover the phase, consider the two arms of the Mach-Zehnder interferometer, the test beam and the reference beam,

denoted by ψ_t and ψ_r , respectively. We can assign a wavefunction to each, given by

$$\psi_t(x, y) = a_t(x, y)e^{i\phi_t(x, y)} \quad \text{and} \quad \psi_r(x, y) = a_{r,i}(x, y)e^{i[\phi_r(x, y) - \delta_i]}, \quad (3.1.1)$$

where $a_t(x, y)$, $a_r(x, y)$ are the amplitudes and $\phi_t(x, y)$, $\phi_r(x, y)$ are the phases of the two beams. The reference beam has an introduced phase shift δ_i which, in the case of this four-step algorithm, takes on four discrete values, each separated by $\pi/2$:

$$\delta_i = 0, \pi/2, \pi, 3\pi/2; \quad i = 1, 2, 3, 4. \quad (3.1.2)$$

The resulting interferogram, $I_i(x, y)$ is given by

$$\begin{aligned} I_i(x, y) &= |\psi_t(x, y) + \psi_{r,i}(x, y)|^2 \\ &= a_t^2(x, y) + a_r^2(x, y) \\ &\quad + 2a_t(x, y)a_r(x, y)\cos[\phi_t(x, y) - \phi_r(x, y) + \delta_i], \end{aligned} \quad (3.1.3)$$

which leads to the fundamental PSI equation (Schreiber and Bruning, 2006),

$$I_i(x, y) = I'(x, y) + I''(x, y)\cos[\phi(x, y) + \delta_i], \quad i = 1, 2, 3, 4 \quad (3.1.4)$$

where the intensity pattern for $I_i(x, y, t)$ is a sum of the average intensity $I'(x, y) = a_t^2(x, y) + a_r^2(x, y)$ and the intensity modulation $I''(x, y) = 2a_t(x, y)a_r(x, y)$, which depends on the wavefront phase difference $\phi(x, y) = \phi_t(x, y) - \phi_r(x, y)$ between the reference and test beams, and the introduced phase shift δ_i . The four-step method requires the recording of four separate interferograms, each separated by $\pi/2$ in phase, according to Eq. 3.1.2. Using Eq. 3.1.4 together with trigonometric identities, the interferograms can be written as

$$\begin{aligned}
 I_0(x, y) &= I'(x, y) + I''(x, y) \cos [\phi(x, y)] \\
 I_1(x, y) &= I'(x, y) - I''(x, y) \sin [\phi(x, y)] \\
 I_2(x, y) &= I'(x, y) - I''(x, y) \cos [\phi(x, y)] \\
 I_3(x, y) &= I'(x, y) + I''(x, y) \sin [\phi(x, y)].
 \end{aligned} \tag{3.1.5}$$

The terms that are constant can be eliminated by combining the four interferograms, as follows:

$$\frac{I_3 - I_1}{I_0 - I_2} = \frac{\sin [\phi(x, y)]}{\cos [\phi(x, y)]}. \tag{3.1.6}$$

Arriving at the final result, the phase can be recovered using

$$\phi(x, y) = \text{atan} \left[\frac{I_3 - I_1}{I_0 - I_2} \right]. \tag{3.1.7}$$

3.2 Argand-plane vorticity singularities in complex scalar optical fields: An experimental study using optical speckle

On the following pages is inserted the as-published form of the second of three first-author papers arising from this thesis. The paper has been published as:

F. Rothschild, A. I. Bishop, M. J. Kitchen, and D. M. Paganin, ‘Argand-plane vorticity singularities in complex scalar optical fields: An experimental study using optical speckle’, *Opt. Exp.* 22, pp 6495–6510 (2014).

Note that, due to a printing error, the last two sentences of the caption of Fig. 8 in this publication are obscured. These state: “The location of vortices are indicated by circles: dark fill for vortices and light fill for antivortices. The field-of-view measures 1.48 mm × 1.11 mm. The Argand mapping is shown in e), now with much finer sampling, allowing a clear image of vorticity singularities.”

Argand-plane vorticity singularities in complex scalar optical fields: An experimental study using optical speckle

Freda Rothschild,^{*} Alexis I. Bishop, Marcus J. Kitchen,
and David M. Paganin

School of Physics, Monash University, Victoria 3800, Australia

Abstract: The Cornu spiral is, in essence, the image resulting from an Argand-plane map associated with monochromatic complex scalar plane waves diffracting from an infinite edge. Argand-plane maps can be useful in the analysis of more general optical fields. We experimentally study particular features of Argand-plane mappings known as “vorticity singularities” that are associated with mapping continuous single-valued complex scalar speckle fields to the Argand plane. Vorticity singularities possess a hierarchy of Argand-plane catastrophes including the fold, cusp and elliptic umbilic. We also confirm their connection to vortices in two-dimensional complex scalar waves. The study of vorticity singularities may also have implications for higher-dimensional fields such as coherence functions and multi-component fields such as vector and spinor fields.

© 2014 Optical Society of America

OCIS codes: (030.6140) Speckle; (050.4865) Optical vortices; (070.2580) Paraxial wave optics; (110.3175) Interferometric imaging; (110.4153) Motion estimation and optical flow; (120.5050) Phase measurement; (260.6042) Singular optics; (350.6980) Transforms.

References and links

1. M. Born and E. Wolf, *Principles of Optics*, 7th ed. (Cambridge University, 1999).
2. J. B. Keller, “Geometrical theory of diffraction,” *J. Opt. Soc. Am.* **52**, 116–130 (1962).
3. K. S. Morgan, K. K. W. Siu, and D. M. Paganin, “The projection approximation and edge contrast for x-ray propagation-based phase contrast imaging of a cylindrical edge,” *Opt. Express* **18**, 9865–9878 (2010).
4. F. Rothschild, M. J. Kitchen, H. M. L. Faulkner, and D. M. Paganin, “Duality between phase vortices and Argand-plane caustics,” *Opt. Commun.* **285**, 4141–4151 (2012).
5. K. O’Holleran, M. R. Dennis, F. Flossman, and M. J. Padgett, “Fractality of light’s darkness,” *Phys. Rev. Lett.* **100**, 053902 (2008).
6. K. O’Holleran, F. Flossman, M. R. Dennis, and M. J. Padgett, “Methodology for imaging the 3D structure of singularities in scalar and vector optical fields,” *J. Opt. A Pure Appl. Opt.* **11**, 094020 (2009).
7. M. V. Berry, “Optical currents,” *J. Opt. A Pure Appl. Opt.* **11**, 094001 (2009).
8. H. S. Green and E. Wolf, “A scalar representation of electromagnetic fields,” *Proc. Phys. Soc. A* **66**, 1129–1137 (1953).
9. I. Kolar, J. Slovak, and P. W. Michor, *Natural Operations in Differential Geometry* (Springer, 1993).
10. M. V. Berry and M. R. Dennis, “Topological events on wave dislocation lines: Birth and death of loops, and reconnection,” *J. Phys. A Math. Theor.* **40**, 65–74 (2007).
11. M. R. Dennis, K. O’Holleran, and M. J. Padgett, “Singular optics: Optical vortices and polarization singularities,” *Prog. Opt.* **53**, 293–363 (2009).
12. H. F. Schouten, G. Gbur, T. D. Visser, and E. Wolf, “Phase singularities of the coherence function in Young’s interference pattern,” *Opt. Lett.* **28**, 968–970 (2003).
13. J. F. Nye, *Natural Focusing and Fine Structure of Light* (Institute of Physics, 1999).

14. H. Schreiber and J. H. Bruning, "Phase shifting interferometry," in *Optical Shop Testing*, D. Malacara, ed. (Wiley, 1992).
15. L. J. Allen, H. M. L. Faulkner, M. P. Oxley, and D. M. Paganin, "Phase retrieval and aberration correction in the presence of vortices in high-resolution transmission electron microscopy," *Ultramicroscopy* **88**, 85–97 (2001).
16. L. J. Allen, H. M. L. Faulkner, K. A. Nugent, M. P. Oxley, and D. M. Paganin, "Phase retrieval from images in the presence of first-order vortices," *Phys. Rev. E* **63**, 037602 (2001).
17. M. J. Kitchen, D. M. Paganin, R. A. Lewis, N. Yagi, K. Uesugi, and S. T. Mudie, "On the origin of speckle in x-ray phase contrast images of lung tissue," *Phys. Med. Biol.* **49**, 4335–4348 (2004).
18. E. A. L. Henn, J. A. Seman, E. R. F. Ramos, M. Caracanhas, P. Castilho, E. P. Olimpio, G. Roati, D. V. Magalhaes, K. M. F. Magalhaes, and V. S. Bagnato, "Observation of vortex formation in an oscillation trapped Bose–Einstein condensate," *Phys. Rev. A* **79**, 043618 (2009).
19. M. R. Matthews, B. P. Anderson, P. C. Haljan, D. S. Hall, C. E. Wieman, and E. A. Cornell, "Vortices in a Bose–Einstein condensate," *Phys. Rev. Lett.* **83**, 2498–2501 (1999).
20. C. Raman, J. R. Abo-Shaeer, J. M. Vogels, K. Xu, and W. Ketterle, "Vortex nucleation in a stirred Bose–Einstein condensate," *Phys. Rev. Lett.* **87**, 210402 (2001).
21. I. Freund, "Critical point explosions in two-dimensional wave fields," *Opt. Commun.* **159**, 99–117 (1999).
22. G. Gbur and T. D. Visser, "Coherence vortices in partially coherent beams," *Opt. Commun.* **222**, 117–125 (2003).
23. M. L. Marasinghe, D. M. Paganin, and M. Prémaratne, "Coherence-vortex lattice formed via Mie scattering of partially coherent light by several dielectric nanospheres," *Opt. Lett.* **36**, 936–938 (2011).
24. P. Liu, H. Yang, J. Rong, G. Wang, and Y. Yan, "Coherence vortex evolution of partially coherent vortex beams in the focal region," *Opt. Laser Technol.* **42**, 99–104 (2010).
25. W. Wang and M. Takeda, "Coherence current, coherence vortex and the conservation law of coherence," *Phys. Rev. Lett.* **69**, 223904 (2006).

1. Introduction

The Cornu spiral is, in essence, the mapping to the Argand plane of the optical field over a plane perpendicular to the optical axis, which results when monochromatic complex scalar plane waves are normally incident upon an infinite edge. This is illustrated in Fig. 1(a), which plots the Argand-plane image of the complex optical field

$$\Psi(s) = C(s) + iS(s) \quad (1)$$

where [1, sec. 8.7.3]

$$C = b \left\{ \left[\frac{1}{2} + \mathcal{C}(s) \right] - \left[\frac{1}{2} + \mathcal{S}(s) \right] \right\} \quad (2)$$

$$S = b \left\{ \left[\frac{1}{2} + \mathcal{C}(s) \right] + \left[\frac{1}{2} + \mathcal{S}(s) \right] \right\} \quad (3)$$

resulting from diffraction of a plane wave by an infinite opaque edge. Here, $\mathcal{C}(s)$ and $\mathcal{S}(s)$ denote the Fresnel integrals, b is a constant and s is a variable and both depend on the position of the point of observation. Adopting the perspective of Keller's geometrical theory of diffraction [2], (i) the bottom-left lobe of the spiral in Fig. 1(a) corresponds to the phasor associated with cylindrical waves scattered from the diffracting edge into the region of geometrical shadow; while (ii) the top right lobe results from the coherent superposition of the incident plane wave phasor with the scattered cylindrical edge wave.

The Cornu spiral can be generalized. Morgan *et al.* [3] found that in the geometrical shadow of an infinitely long uniform dielectric cylinder normally illuminated by monochromatic scalar plane waves, the Cornu spiral turns into a hypocycloid (see Fig. 1(b) [3]) as a result of the distorted plane wave (having travelled through the cylinder) superposing with the wave diffracting from the edge of the cylinder. Morgan *et al.* also found that the magnitudes of the oscillation of the Cornu spiral and the hypocycloid decrease with propagation distance, and wrote down approximate analytical expressions for these fields using the geometric theory of diffraction.

In Rothschild *et al.* [4], we considered the role of the Argand plane as a means to add insight into vortex behaviour in a complex scalar two-dimensional wavefield. We simulated a vortex-laden speckle field by spatially filtering two-dimensional complex white noise. Note that, in

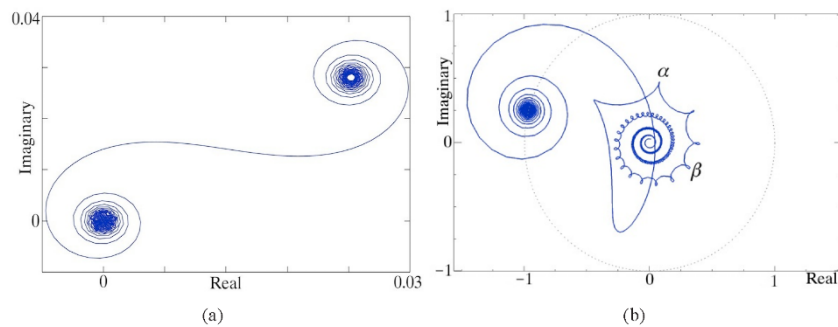


Fig. 1. (a) A Cornu spiral generated by taking the Argand-plane image of the complex field resulting when a plane wave diffracts from an infinite opaque edge upon which it is incident. (b) From Morgan *et al.* [3], the simulated Argand-plane plot for coherent x-ray scalar waves diffracted by a uniform infinitely-long dielectric cylinder. One lobe of the Cornu spiral evolves into a hypocycloid in the geometrical shadow of the cylinder. The dotted circle corresponds to the unscattered plane-wave and has an intensity of 1.

passing from complex fields that vary in only one of the two transverse dimensions to those that vary in both transverse dimensions, the associated Argand-plane map evolves from a line trace (generalized Cornu spiral) into a fully two-dimensional mapping. The appearance of this mapping is typically reminiscent of the caustic-network pattern seen at the bottom of a swimming pool on a bright day. In particular, for such maps we looked at the connection between Argand-plane singularities and quantized phase vortices in the physical field. We described the role of vortices and vorticity in the appearance of singularities of the mapping \mathcal{M} of the complex wavefunction to the Argand plane – namely, the cusp and the fold vorticity singularities. Note that we previously referred to these singularities as “Argand-plane caustics” [4]. However, following advice from Sir M.V. Berry in a private communication to the corresponding author, we herein use the term “vorticity singularities” in recognition of the fact that Argand-plane singularities are not associated with gradient maps and do not correspond to caustics, or a focussing of rays in real space.

In the present paper we experimentally verify the numerical predictions made in Rothschild *et al.* [4] by calculating Argand mappings of coherent two-dimensional complex scalar wavefunctions associated with optical speckle fields. We generate such a speckle field by experimentally recreating the process used for simulations in Rothschild *et al.* [4]. Additionally, we use the Taylor series expansion of the complex wavefunction to present a local means to locate Argand-plane singularities of any order. Vortices in speckle fields have been studied previously (see e.g. [5]) and similar experimental and data smoothing techniques to those adopted here have been used by O’Holleran *et al.* [6]. However, the present work considers the detailed structure of vortices and relates it to the seminal work on “Optical currents” by Berry [7]. We also provide an experimental verification of aspects of the work laid down by Berry [7].

We close this introduction with an outline of the remainder of the paper. Section 2 details the theory of Argand-plane vorticity singularities. Section 3 provides a description of the experimental set-up and execution whereby an optical phase-stepping interferometer is used to measure Argand-plane maps of coherent vortical speckle. Section 4 reports on the results of the experiment and the methods used to analyse the data. Using the results, we confirm our predictions regarding Argand-plane singularities, shown in Sec. 5. We provide a discussion in

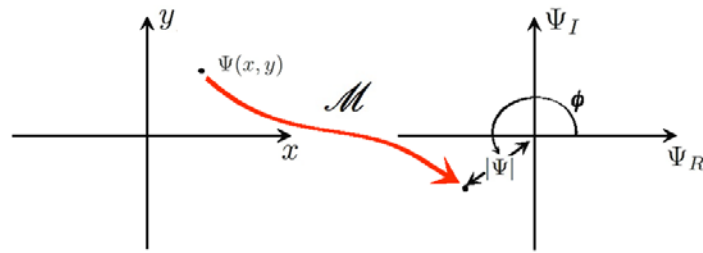


Fig. 2. The Argand mapping of a complex number $\Psi(x, y)$ for a given point (x, y) . The axis in the Argand plane are parameterized by Ψ_R and Ψ_I . The magnitude and phase of the wavefunction $\Psi(x, y)$ are represented by $|\Psi|$ and ϕ , respectively.

Sec. 6, and conclude with Sec. 7.

2. Theory of Argand-plane vorticity singularities

An arbitrary two-dimensional differentiable continuous single-valued complex function $\Psi(x, y)$ induces a mapping $\mathcal{M} : \mathbb{R}^2 \rightarrow \mathbb{C}$ from two-dimensional real space to the Argand plane, given by

$$\mathcal{M}(\Psi(x, y)) \rightarrow \{\Psi_R, \Psi_I\}. \quad (4)$$

Here, Ψ_R and Ψ_I denote the real and imaginary parts of $\Psi(x, y)$, which is the boundary value of the spatial part of a forward-propagating monochromatic scalar three-dimensional wave-field over a given planar surface [8]. In this paper, coherent scalar fields are assumed and harmonic time dependence is suppressed.

Figure 2 shows the Argand mapping of a complex number $\Psi(x, y)$ that is associated with a single Cartesian co-ordinate (x, y) in real space to a point on the Argand plane. The set of all such image points for a given $\Psi(x, y)$ may be viewed as a two-dimensional generalization of the Cornu spiral. This generalization forms the core subject of this paper.

Before proceeding, we recall that $\Psi(x, y)$ is only defined up to a global phase factor $\exp(i\psi_0)$, where ψ_0 is any real number. This freedom, which for time-independent field equations typically arises from the invariance of the said equations with respect to the origin of time, implies that the Argand plane image corresponding to Eq. 4 may only be meaningfully defined modulo an arbitrary rigid rotation about the Argand plane origin. Global phase factors may also be introduced into a two-dimensional complex wavefunction, by, for example, passing the wave through a thin sheet of non-absorbing glass. Such global phase factors effect a rigid Argand-plane rotation, which amounts to a re-coordinatization of the Argand plane, they do not alter the conclusions drawn below.

To locate the singularities induced by the mapping \mathcal{M} corresponding to a specified small patch of (x, y) space, we can perform a jet [9] operation, taking the complex wavefunction $\Psi(x, y)$ and producing a low-order Taylor polynomial at every point of its domain. Truncating at second order about a given fixed point (x_p, y_p) , we have

$$\Psi(x, y) = A + Bx + Cy + Dxy + Ex^2 + Fy^2, \quad (5)$$

where $A \equiv A(x_p, y_p), B \equiv B(x_p, y_p), \dots, F \equiv F(x_p, y_p) \in \mathbb{C}$. The Jacobian determinant ("Jacobian") of the mapping \mathcal{M} to the Argand plane associated with $\Psi(x, y)$ is given by

$$\begin{aligned}
J(x,y) &= \begin{vmatrix} \partial_x \Psi_R & \partial_y \Psi_R \\ \partial_x \Psi_I & \partial_y \Psi_I \end{vmatrix} \\
&= (B_R + D_R Y + 2E_R X)(C_I + D_I X + 2F_I Y) \\
&\quad - (C_R + D_R X + 2F_R Y)(B_I + D_I Y + 2E_I X),
\end{aligned} \tag{6}$$

which is quadratic in x and y for the Taylor expansion to second order, and, when set to zero, provides the location of singularities in the Argand plane for an arbitrary second-order wavefunction. Therefore for a patch of space centered about (x_p, y_p) that is sufficiently small for Eq. (5) to be a good approximation, the locus of points for which $J = 0$ corresponds to a conic section in (x, y) space, that is, a parabola, hyperbola, ellipse or straight line. The Argand-plane image of this locus of points will then correspond to the associated Argand-plane singularity. These conic sections will evolve into more general curves if the Taylor expansion in Eq. (5) is taken to higher than second order, although we note that the method of analysis presented here is readily generalized to such a case.

The Jacobian determinant of \mathcal{M} at a point (x, y) provides important information about the transformation of $\Psi(x, y)$ under the mapping from an infinitesimal two-dimensional patch enclosing this point. The absolute value of the Jacobian J at some point (x_p, y_p) gives the factor by which Ψ expands or contract infinitesimal patches at p upon being mapped from real space to the Argand plane, while the sign of J indicates whether the patch has been flipped ($J < 0$) or not ($J > 0$). A value of $J = 0$ indicates that a patch of space in the xy plane has collapsed into a single point and an Argand-plane singularity has formed for $\mathcal{M}(\Psi(x, y))$.

We can assign a physical meaning to the Jacobian. The vorticity Ω of a three-dimensional complex scalar field $\Psi(x, y, z)$ can be expressed as [10]

$$\Omega = \nabla \times \mathbf{j} = \text{Im}(\nabla \Psi^* \times \nabla \Psi) = \nabla \Psi_R \times \nabla \Psi_I, \tag{7}$$

where ∇ is the gradient operator and $\mathbf{j} = \text{Im} \Psi^* \nabla \Psi$ is the current up to a multiplicative constant which is set to unity here. The vorticity gives the amount of local rotation in the field. The z -component of the local vorticity,

$$\Omega_z = \frac{\partial \Psi_R}{\partial x} \frac{\partial \Psi_I}{\partial y} - \frac{\partial \Psi_I}{\partial x} \frac{\partial \Psi_R}{\partial y}, \tag{8}$$

represents the local current rotation at (x, y) and is equivalent to the Jacobian, as seen from Eq. 6. When the local current rotation of the field changes from clockwise to anti-clockwise, that is, where $\Omega_z = 0$, a singularity will be induced by \mathcal{M} . This fact arises from the continuity of the vorticity, i.e. if Ω_z changes sign as one traverses a given path then the vorticity must vanish for at least one point along the path. As with the Jacobian, points where the vorticity are equal to zero will map to Argand-plane singularities under \mathcal{M} .

The vorticity Ω should not be confused with the local orbital angular momentum density $\mathbf{L} = \mathbf{r} \times \mathbf{j}$. The longitudinal orbital angular momentum density is given by

$$L_z = \text{Im} [\Psi^* (x \partial_y \Psi - y \partial_x \Psi)]. \tag{9}$$

Note the distinction between the local current rotation referred to above, and the quantized phase vortices associated with screw-type singularities which are a regular feature of complex scalar functions such as $\Psi(x, y)$. Such phase vortices are characterized by the vanishing of the real and imaginary part of the wave function at the core of the vortex with a change of phase by an integer multiple of 2π around it. These structures yield interesting features in

the Argand plane. For detailed descriptions of optical vortices, see e.g. the seminal works of [11, 12]. Modulo a continuous deformation, a phase vortex at (x_0, y_0) can be locally given by

$$\Psi_{\pm} = (x - x_0) \pm i(y - y_0), \quad (10)$$

where an infinitesimal patch at (x_0, y_0) maps under \mathcal{M} to cover the Argand-plane origin, at which point $\text{Re}(\Psi) = \text{Im}(\Psi) = 0$. Ψ_+ denotes a vortex (anti-clockwise phase winding) and Ψ_- an anti vortex (clockwise phase winding). In Ψ_+ , the infinitesimal patch in xy space maps directly onto the Argand-plane origin; in Ψ_- it must be “flipped” in order to cover the Argand-plane origin with the correct orientation. Thus, when there are two vortices of opposite helicity within a simply-connected region in the field of $\Psi(x, y)$, the patches of space will map to the Argand plane origin with one patch being flipped relative to the other, implying the presence of an Argand singularity such as a fold that is induced under the mapping \mathcal{M} of the region. The continuity of $\Psi(x, y)$ yields a many-to-one mapping where the fold occurs, thus implying the presence of a singularity. This is an example wherein a function can be transformed under \mathcal{M} to bring about *Argand-plane singularities*, that, in this case, are intimately connected to the presence of vortices of opposite helicity in $\Psi(x, y)$ (see [4] for more detail).

Returning to the main thread of the argument, we can exemplify Eqn. 6 by taking the special case of a second-order complex polynomial, given by

$$\Psi(x, y) = A + x + iy + xy + \frac{i}{2}(x^2 - y^2), \quad A \in \mathbb{C} \quad (11)$$

for which the Jacobian of \mathcal{M} vanishes on the unit circle:

$$J(x, y) = 1 - x^2 - y^2 = 0. \quad (12)$$

To determine the Argand-plane image of the unit circle, under the Argand-plane map \mathcal{M} which is induced by the wavefunction given in Eq. 11, let us parameterize the unit circle via $\theta \in [0, 2\pi)$, as

$$\begin{cases} x(\theta) = \cos \theta, \\ y(\theta) = \sin \theta, \quad 0 \leq \theta \leq 2\pi. \end{cases} \quad (13)$$

Now we can write the Argand-plane coordinates from Eqns. 11 and 13 as

$$\begin{cases} \Psi_R(\theta) = A_R + \cos \theta + \frac{1}{2} \sin 2\theta, \\ \Psi_I(\theta) = A_I + \sin \theta + \frac{1}{2} \cos 2\theta, \quad A \in \mathbb{C}, \quad \theta \in [0, 2\pi]. \end{cases} \quad (14)$$

Visual representations of the magnitude $|\Psi|$, phase ψ , current vorticity $|\Omega_z|$ and orbital angular momentum $|L_z|$ associated with Eqn. 11 are shown in Fig. 3. A plot of Ψ_R against Ψ_I as defined by Eq. 14 is shown in Fig. 3(e) and takes the form of the cross-section of an elliptic umbilic catastrophe [13]. The zeros of $|\Omega_z|$ and $|L_z|$ have no direct association with one another, as predicted by Berry [7].

In the following sections, we will show that Argand mappings containing vorticity singularities can be observed experimentally using an optical speckle field.

We close this theory section with an idea raised by one of the anonymous referees of this paper. Consider a simply-connected two-dimensional region, over which the continuous complex single-valued scalar field $\Psi(x, y)$ is defined. Assume also that the field does not vanish at any point on the boundary, which in turn implies that the phase $\phi(x, y) = \text{Arg}\Psi(x, y)$ is defined at each point of the boundary. Assume that any phase vortices within the boundary will have

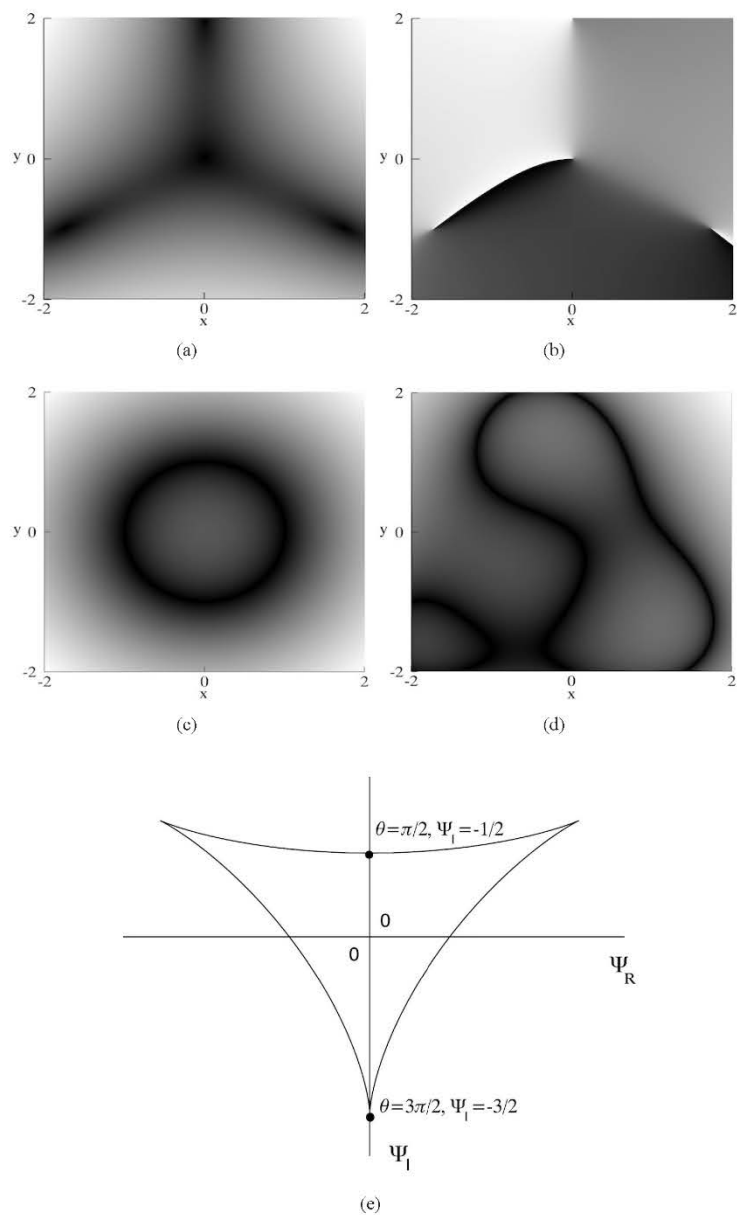


Fig. 3. Various visualizations of $\Psi(x, y)$ in Eqn. 11 evaluated over $-2 \leq x, y \leq 2$. (a) $|\Psi|$; (b) phase ϕ ; (c) a plot of $|\Omega_z|$, which falls to zero over a unit circle, as predicted by Eqn. 12; (d) a plot of $|L_z|$ and (e), the parametric plot of Eqn. 14, which is the image of $\Psi(x, y)$ in the Argand plane and takes the form of the cross-section of an elliptic umbilic catastrophe [13].

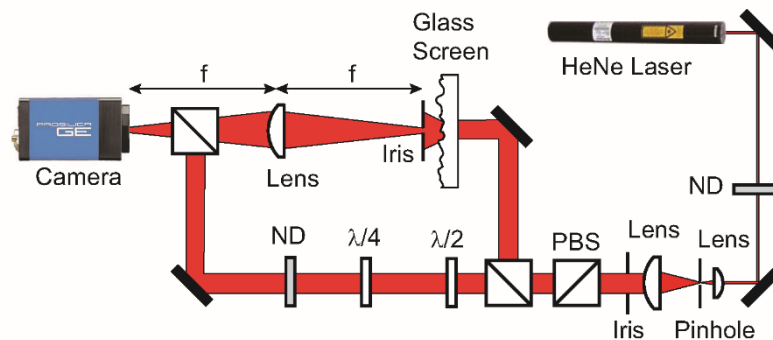


Fig. 4. Schematic of apparatus for creating and identifying optical vortices. The apparatus is a form of Mach-Zehnder interferometer and the waveplates allow the recording of interferograms using a CCD camera with different phase shifts of the reference beam, for analysis using phase-step interferometry. Optical vortices are created by the speckle interference from the ground glass screen and the distribution of vortices is controlled by the size of the downstream iris.

topological charges that have a magnitude of unity, which is typically a good assumption for generic fields on account of the instability of higher-order vortices. Knowledge of the phase over the boundary will then allow one to determine the net topological charge of the field, namely $Q = N(+)-N(-)$, where $N(+)$ and $N(-)$ are the number of positive and negative unit charges, respectively. Also, as pointed out in Ref. [4], the number of Argand-plane sheets covering the Argand origin (cf. Fig. 8) is equal to the total number $N = N(+)+N(-)$ of vortices. Thus knowledge of both Q and N allows $N(+)= (N+Q)/2$ and $N(-)= (N-Q)/2$ to be independently measured without needing to locate each vortex individually or needing to determine the topological charge of each such vortex.

3. Experimental method

In Rothschild *et al.* [4], we computationally generated vortices using the spatial filtering of two-dimensional complex white noise. The Fourier transform of resulting wavefield was truncated using a low-pass filter, resulting in a speckle field once an inverse two-dimensional Fourier transform was applied. The cutoff of the low-pass filter was used to control the size of the speckle.

This process can be achieved in an experiment using a coherent laser, a ground glass screen, a circular iris and a lens, among other apparatus. A schematic of the experiment is shown in Fig. 4.

The output of a linearly-polarised Helium-Neon laser (Thorlabs, 5 mW) was passed through a neutral density filter, and was then spatially filtered by an $f = 18.4$ mm aspheric lens, and a $20 \mu\text{m}$ pinhole located at the focus, followed by an iris downstream set to pass only the zero-order central maxima. The filtered beam was collimated by an $f = 100$ mm plano-convex lens to give a planar, near-Gaussian beam of approximately 6 mm diameter. The collimated beam passed through a polarising beamsplitter cube to ensure that the beam used in the experiment had pure vertical polarisation. The neutral density filter attenuated the beam to eliminate saturation of the camera.

A random phase field containing optical vortices was created by passing the expanded planar

laser beam through a random phase plate, composed of a fine ground glass plate from a film-camera viewing screen. An iris (aperture set to approximately 0.8 mm) immediately after the screen limited the aperture for the system and determined the characteristic size of the speckle interference pattern that propagated towards the CCD camera (Prosilica GE1650).

A plano-convex lens ($f = 300$ mm) located one focal length away from both the iris and the camera ensured that the Fourier transform of the speckle pattern was recorded on the camera. This corresponded to the far-field (Fraunhofer) diffraction of the speckle field present at the iris.

In order to plot the data in the Argand plane, it was necessary to recover the phase information. This was done using phase stepping interferometry [14]. The algorithm we used requires that four separate interferograms are recorded. As shown in Fig. 4, a reference beam was split from the laser beam before it encountered the glass screen, which was then passed through a $\lambda/4$ and a $\lambda/2$ waveplate before being recombined with the random phase field on the camera. Each beam traversed an equal length to the camera and the optical configuration was that of a Mach-Zehnder interferometer. A neutral density filter (OD 1) attenuated the beam intensity to match the intensity of the beam containing the optical vortices. Rotating the waveplates to change the alignment of the optical axis of a waveplate from the slow axis to the fast axis with respect to the beam polarisation introduced the characteristic phase shift retardance of the waveplate without introducing additional phase variations that would be associated with removing the waveplate. Using a combination of waveplate retardances, a 90° optical phase shift was introduced into the reference beam between each sequentially recorded interferogram. These interferograms corresponded to the reference beam being retarded by 0° , 90° , 180° and 270° . The phase $\phi(x,y)$ was calculated using

$$\phi(x,y) = \tan^{-1} \left[\frac{I_4 - I_2}{I_1 - I_3} \right], \quad (15)$$

where I_i is the intensity of the interferogram recorded for phase retardances $\delta_i = 0, \pi/2, \pi, 3\pi/2$, where $i = 1, 2, 3, 4$ [14].

4. Results

The results of the experiment for the reconstructed intensity and phase are shown in Fig. 5. The region of interest (ROI) is outlined by a white broken rectangle and enlarged for both intensity and phase in Fig. 5. This selection lies near the local minimum of the gentle background curvature in the phase, on the order of 10 wavelength per millimetre. Additionally, the size of the ROI is small enough to allow us to clearly see features in the Argand plane. We note the presence of interference fringes in several areas of the ROI, evident as ripples in the phase and intensity, and are due to unwanted scattering by optical elements.

The Argand-plane mapping of the data in Fig. 5 is shown in Fig. 6. It is difficult to see any of the behaviour described in Sec. 2, in particular that of vorticity singularities, due to an overlying high frequency ripple. These Argand-plane ripples are due to the high frequency interference fringes noted in Fig. 5.

To clean up the Argand image of the data and reveal the underlying vorticity singularities, a Gaussian (Fourier) filter was applied at the level of the complex field. This strategy was necessary because one can not directly smooth the branch cuts in the multi-valued phase map. The process is shown in Fig. 7. Looking at the power spectrum in Fig. 7(a), there is a diagonal streaking effect at medium to high spatial frequencies. This is unrelated to the vertical and horizontal cross-shaped streaking, which is due to truncating to a rectangular region of interest. In order to achieve smoother results, we can apodise the power spectrum by a Fourier-space Gaussian filter (Fig. 7(b)) that is small enough to exclude any unwanted features.

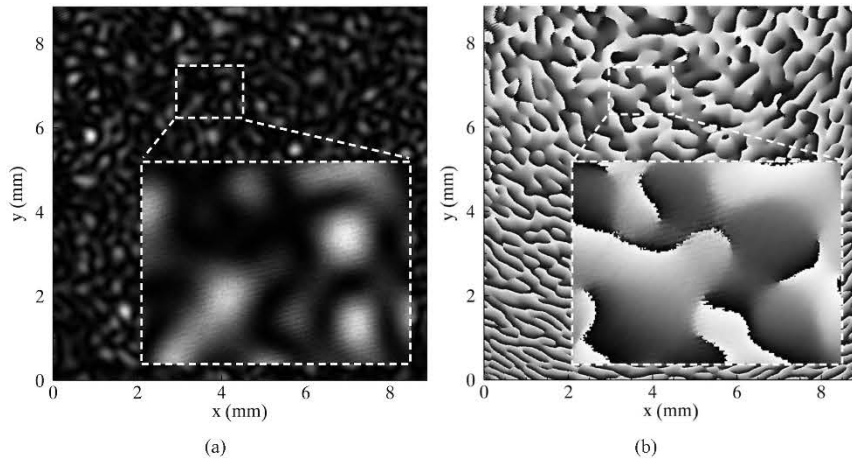


Fig. 5. (a) The intensity and (b) the phase, which were reconstructed using a phase-stepping method applied to the speckle field created by the apparatus in Fig. 4. The broken rectangles indicate the ROI. These areas are enlarged to reveal a greater level of detail.

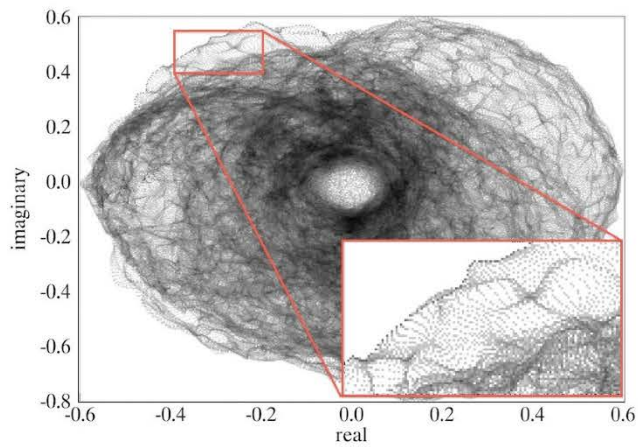


Fig. 6. The Argand-plane mapping of the ROI of the data shown in Fig. 5. The mapping is polluted by a high frequency ripple, an example of which is enlarged.

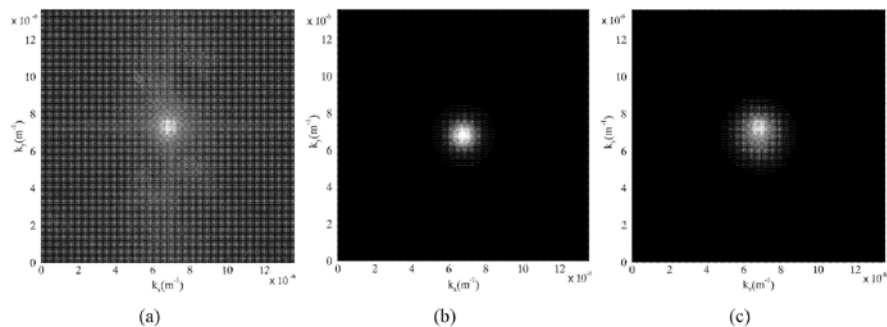


Fig. 7. The application of Fourier-space Gaussian filter to smooth the data in Fig. 5 and eliminate the caustic ripple in Fig. 6 so that the underlying structure of the Argand-mapping of the data can be revealed. (a) The power spectrum of the data in Fig. 5, as a function of the spatial frequencies (k_x, k_y) dual to (x, y) . The diagonal streaking originates from parasitic scattering. This is related to the ripple behaviour seen in Fig. 6; (b) The Fourier-space Gaussian filter and (c) the result of the application of the Gaussian filter on the power spectrum, from where the diagonal streaking has been removed.

Upon smoothing the data, a cubic interpolation was performed to increase the density of points in the ROI by a multiple of 15. Due to the smoothing and interpolation, the interference fringes that were visible in Fig. 5 are not present and the sampling has become finer. The final result is shown in Fig. 8.

Figures 8(c) and 8(d) show the orbital angular momentum density and vorticity calculated corresponding to the indicated region of data, respectively. The position of the vortices in these images is consistent with the work of Berry in his seminal Optical Currents work [7], in which he stated that the location of vortex cores has no special relationship to the vorticity of a wave-field. This is indeed the case in Fig. 8(c). Figure 8(d) shows that each of the vortex cores coincide with a zero in the orbital angular momentum, consistent with the prediction by Berry [7].

5. Analysis

Vorticity singularities were distinguished in the Argand plane and linked to particular behaviours in the wave field. The Jacobian determinant was calculated to obtain a visual indication of the phase winding behavior. Figure 9(a) shows the phase of the first frame of data. The black lines are the regions where the magnitude of the Jacobian is sufficiently close to zero, $|J| < \epsilon = 0.5 \times 10^{-7}$. As explained in Sec. 2, the regions where $J = 0$ possess a two-fold meaning: That a patch of space has induced a many-to-one mapping under \mathcal{M} , forming an Argand-plane singularity and that a region of zero vorticity exists there. We previously predicted that a region of the wave field containing vortices of opposite helicity must fold at least once under \mathcal{M} so that each vortex covers the Argand-plane origin, inducing a fold singularity. The red loop in Fig. 9(a) contains a vortex and an anti-vortex separated by a single “zero Jacobian line”. Therefore we expected that the patch of space will fold once, inducing a fold singularity under \mathcal{M} . Indeed, in Fig. 9(c), the Argand image of the area enclosed by the red loop, confirms this. The green loop encloses two vortices of the same helicity. This would imply that the patch of space that contains these does not have to fold under \mathcal{M} as both vortices must map to the Argand plane origin in the same orientation. Indeed, the corresponding Argand image, shown in Fig. 9(d) does not contain a fold. Rather the patch of space covers the origin for the first vortex and then *loops around* so that the other vortex covers the origin. Hence we have two patches covering the origin, corresponding to two vortices, however, no singularity

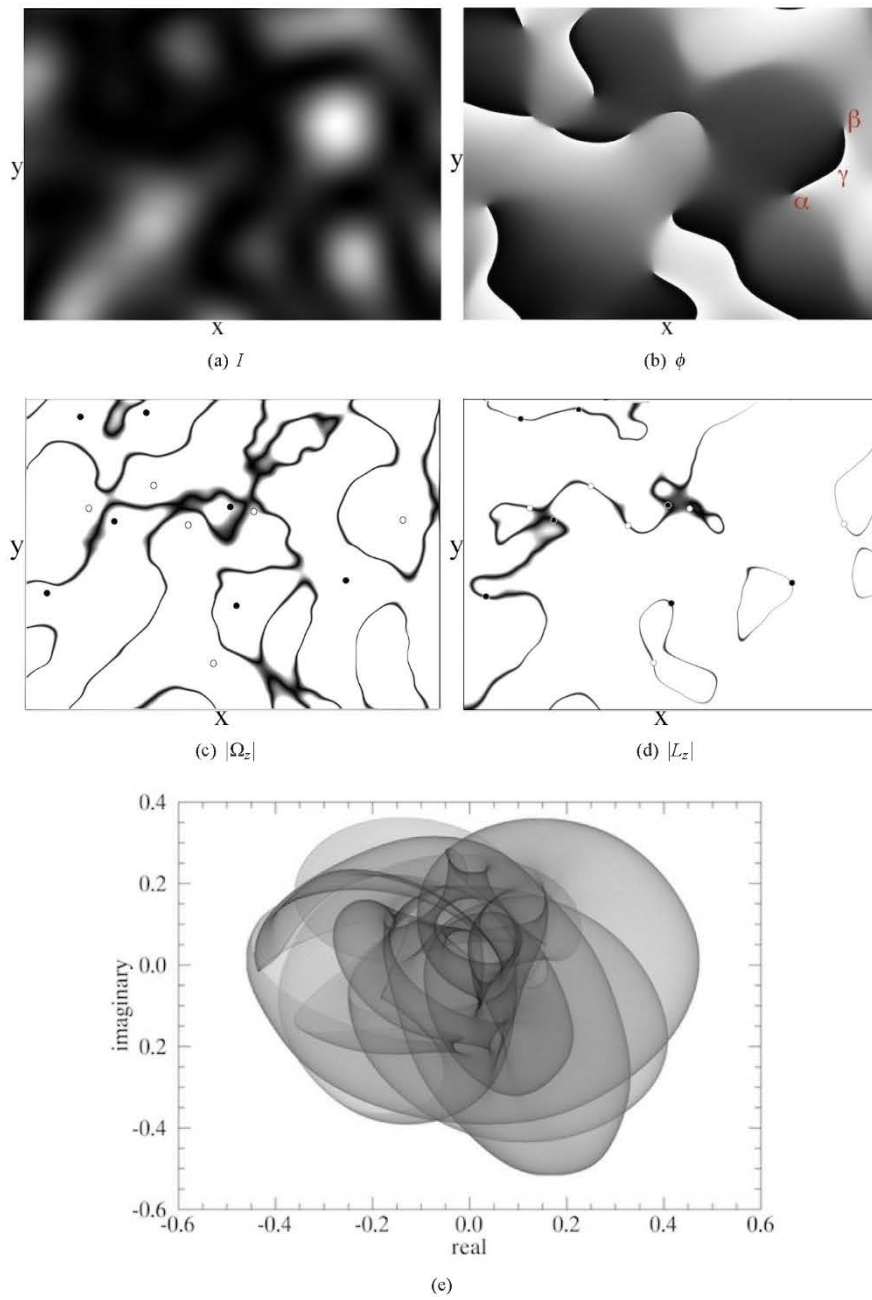


Fig. 8. The result of applying the Gaussian filter of Fig. 7 and expanding the density of points in the region of interest by a multiple of 15 using cubic interpolation. The intensity (a) and phase (b) appear smoother. Minimum values are represented by black, maximum by white. Several features are indicated in the phase: A vortex α , antivortex β and branch cut γ . The vorticity Ω and angular momentum L are also calculated. $|\Omega_z| < 0.5 \times 10^{-7}$ is shown in (c) and $|L_z| < 0.035$ is shown in (d). The locations of vortices are indicated by circles: dark fill for vortices and light fill for antivortices. The field-of-view measures $1.48 \text{ mm} \times 1.11 \text{ mm}$. The Argand mapping is shown in (e), now with much finer sampling allowing a clear image of vorticity singularities.

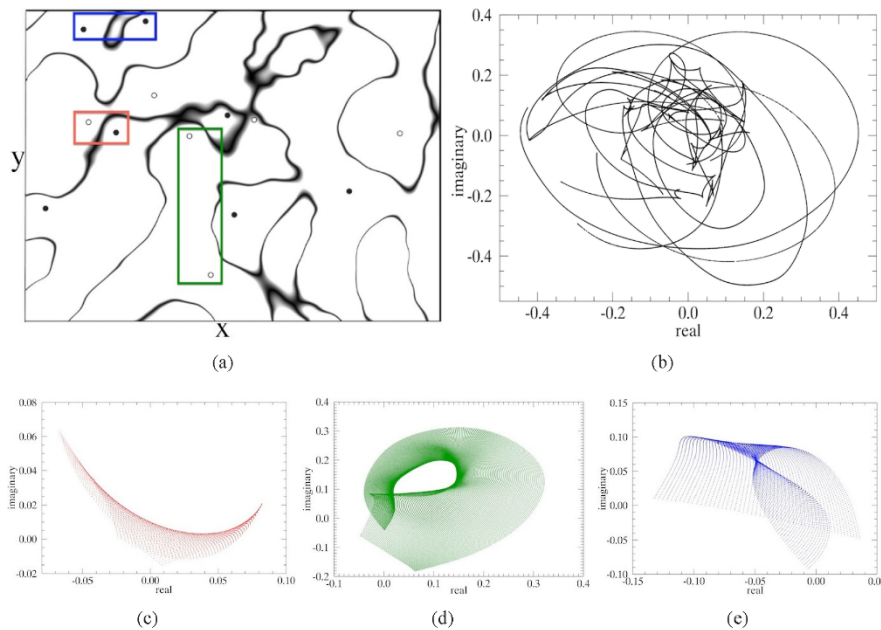


Fig. 9. (a) The zeroes ($|\Omega_z| < 0.5 \times 10^{-7}$) of the vorticity, calculated by evaluating the Jacobian of the mapping \mathcal{M} , as seen in Fig. 8(a). The image measures $1.48 \text{ mm} \times 1.11 \text{ mm}$. The locations of vortices and anti-vortices are indicated by filled and unfilled circles, respectively. The regions where the Jacobian is sufficiently close to zero are mapped to the Argand plane (b) to reveal an image containing singularities only. A vortex-antivortex dipole separated by one ‘Jacobian line’ is indicated by the red loop in (a) and mapped to the Argand plane in (c) to form a fold caustic. Two antivortices that are not separated by any Jacobian lines are indicated by the green loop and mapped to the Argand plane in (d) to reveal a patch of space that loops around but does not fold. Two vortices separated by two Jacobian lines are indicated by the blue loop and are mapped to the Argand plane in (e) to reveal a fold caustic and a cusp.

has been induced as the direction of the phase winding did not change over the area enclosed by the arrow loop. Finally, the blue loop in Fig. 9(a) also contains two vortices of the same helicity. Here, though, there are two Jacobian lines separating the two vortices. According to Rothschild *et al.* [4], this means the enclosed space must induce two singularities under \mathcal{M} . Figure 9(e) indeed contains two singularities – a fold and a cusp – corresponding to instances where the patch of space folded and then twisted around again, mapping both vortices over the Argand plane origin at the same orientation. Thus the cusp singularity is the result of a “twist” in the Argand plane origin, induced by a change in the direction of the phase winding.

It is easy to see from these examples that, with an understanding of both the vortex distribution and phase winding behaviour of the wave field, the presence of vorticity singularities is a natural result of inducing a mapping \mathcal{M} in a complex scalar function.

There are other, higher order, vorticity singularities that can be observed in the Argand plane. Figure 10(c) shows an image of a vorticity singularity that resembles the cross section of the elliptic umbilic catastrophe. This was induced by the mapping of a “Jacobian ellipse”, shown in

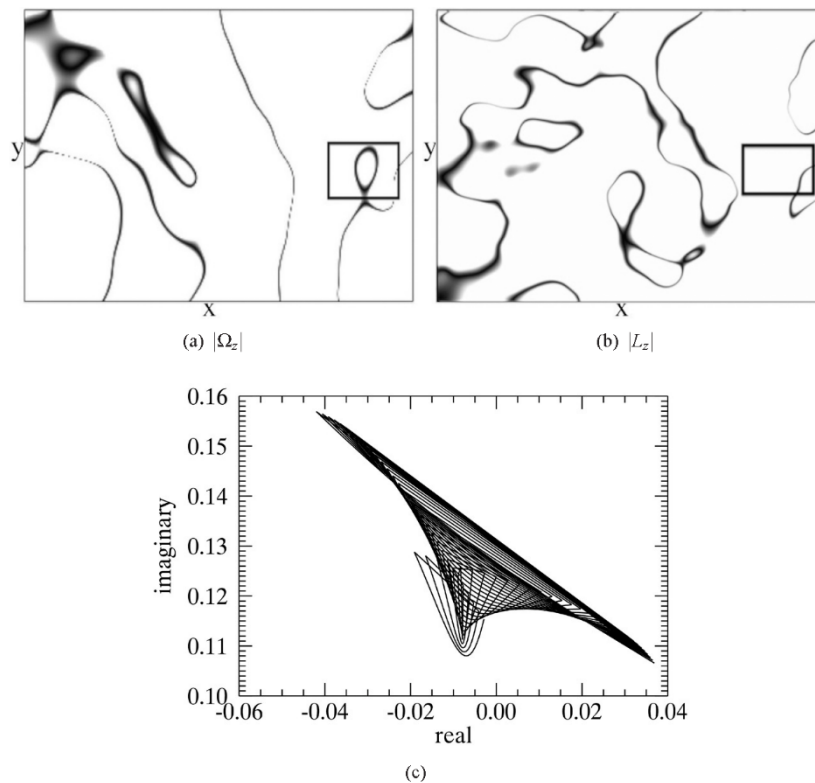


Fig. 10. These data were obtained by shifting the ground glass screen by $10\ \mu\text{m}$. The region of study measures $1.48\ \text{mm} \times 1.11\ \text{mm}$. (a) The zeros of its vorticity, where a “Jacobian ellipse” is indicated by a rectangular loop; (b) the zeroes of the orbital angular momentum, where the area that enclosed the Jacobian ellipse in (a) is shown to be lacking in any equally interesting features of the angular momentum and (c) a vorticity singularity closely resembling the cross-section of an elliptic umbilic catastrophe, induced by the mapping of the Jacobian ellipse to the Argand plane.

Fig. 10(a). This feature was spotted in data that was obtained by transversely shifting the ground glass screen (see Fig. 4) $10\ \mu\text{m}$ from its initial position. The zeros of the angular momentum of this data are shown in Fig. 10(b) and display no direct association with the zeros of the vorticity. This is all consistent with our simulation of the Jacobian ellipse and elliptic umbilic catastrophe in Fig. 3.

We close this Analysis by giving an experimental demonstration of the method outlined in the final paragraph of Sec. 2, which gives a means to determine the total number $N(+)$ of vortices and $N(-)$ of anti-vortices in a simply-connected two-dimensional region, given (i) the knowledge of the phase at each point of the boundary of the region, and (ii) the associated Argand-plane map, under the assumption that (iii) all vortices have topological charges of magnitude unity. By counting the number of black-white and white-black phase wraps along the boundaries of the red loop in Fig. 9(a) one can determine that the net topological charge of the phase map within the loop is $Q = 0$, while zooming in on the Argand-plane origin of the field enclosed in the red loop, shown in Fig. 9(c), shows that there are $N = 2$ sheets covering the

Argand plane origin. Since $Q = N(+)-N(-) = 0$ and $N = N(+)+N(-) = 2$, we calculate that there are $N(+)= (N+Q)/2 = 1$ vortex and $N(-)= (N-Q)/2 = 1$ anti-vortex, which is consistent with the number of black dots (vortices) and the number of white dots (anti-vortices) enclosed in the red loop in Fig. 9(a). The same method can be shown to derive the number of vortices in the blue and green loops in Fig. 9(a). This example shows that the number of vortices, together with the number of anti-vortices, may be determined without needing to locate each individual vortex and anti-vortex.

6. Discussion

Our study of the Argand plane provides a useful complementary method for analysing optical fields. In fact, this device could be used for the study of any complex scalar function, not just optical. Already, the discovery of vorticity singularities that are induced by such a mapping to the Argand plane, and our study of them, has provided us with additional insight into the behaviour of our wavefield. For example, we note the connection between the orbital angular momentum density and vorticity and the significance of vortex locations.

The role of the Argand plane in the analysis of optical fields is an interesting one, and we intend to continue our investigations into its usefulness. An immediate extension of this work is to continue to catalogue vorticity singularities, associating each one with a solution for $J = 0$, as done for the elliptic umbilic in Sec. 2. Other vortical fields such as the focal volumes of aberrated lenses [15–17] and turbulent Bose-Einstein condensates (see [18–20], for instance) and their resulting Argand images under \mathcal{M} could help clarify the connection between phase vortices and vorticity singularities. Berry [7] established that vorticity in an optical field is not associated with the location of vortex cores. It is interesting that we have shown that vorticity singularities are a manifestation of vorticity and are strongly influenced by the location of vortex cores. Further study, such as the extensions described above, could add insight into the work already laid down by Berry.

Further, one could study critical point explosions (see [21]) of high order vortices, and the evolution of its image under \mathcal{M} as an interesting insight into the so-called “vortex-vorticity” duality. Studying the “unfolding” of vorticity singularities with certain parameter changes such as propagation distance or aperture size may also provides insights into the meaning of vorticity singularities.

The investigation into two-dimensional Argand maps is a generalisation of the Cornu spiral mentioned in Sec. 1. We can further generalise Argand maps by looking at vector fields and other multicomponent fields. For example, arbitrary spin matter waves, with spin s , will be described by $2s+1$ complex wave-functions. The mapping of spinor fields to the Bloch, or Poincaré, sphere may possess vorticity singularities. As a generalisation of the two-dimensional complex scalar function, we could look at coherence functions – which are two-point correlation functions and can exist in seven dimensions. In this case, “coherence vortices” become manifest (corresponding to a pair of points in three-dimensional space, together with a time lag or angular frequency [22–24]). The circulating coherence current (see [25]) associated with a coherence vortex is analogous to the current in a complex scalar wavefield. This begs the question: Can the two-point correlation function associated with a partially coherent field littered with coherence vortices induce a mapping to the Argand plane to reveal coherence-current vorticity singularities? If so, what can we learn about the coherence current, and, finally, what is the physical meaning and practical utility of such a construction?

7. Conclusion

We have presented the Argand plane as an interesting tool for the analysis of optical fields. We have verified the existence of vorticity singularities via an experiment involving the spatial

filtering of two-dimensional white noise. We have observed the fold, cusp and elliptic umbilic singularities, and showed them to be consistent with theory. The locations of the zeros of the vorticity and orbital angular momentum density of the field were determined and we observed that their association with the location of vortex cores is consistent with the work of Berry [7]. Finally, we have used the second-order Taylor series expansion of the complex wavefunction to locate vorticity singularities induced by a mapping to the Argand plane. Possible extensions of this work could involve critical point explosions, vector and other multi-component fields and coherence functions.

Acknowledgments

FR thanks Professor Sir Michael Berry for his interest in the concepts discussed in this paper and for interesting discussions. FR also acknowledges funding from the Monash University Faculty of Science Dean's Scholarship scheme. DMP and MIK acknowledge financial support from the Australian Research Council. MIK is an Australian Research Fellow. All authors acknowledge the very useful comments of the referees of this paper, in particular for putting forward the method given in the final paragraph of both Sec. 2 and Sec. 5 of the manuscript.

Chapter 4

A study of generalised Cornu spirals using hard x-rays

In this chapter, the investigation of Argand-plane mappings induced by complex scalar wavefields moves from the domain of visible light to x-rays. In particular, the Argand-plane mappings induced by diffracted x-rays are considered experimentally. Such mappings are shown here to take the form of generalised Cornu spirals. Before presenting the publication that has resulted from my work on this topic, some background theory is included. First, it is necessary to define a theory for predicting the effects of diffraction. In this case, that theory is the Geometrical Theory of Diffraction, which is an extension of Geometrical Optics that accounts for diffraction, despite having abandoned the finite wavelength of light. Following from this is a brief discussion on the existing applications of generalised Cornu spirals for solving diffraction problems or otherwise. Next, it is necessary to describe the techniques used in the experimental reconstruction of generalised Cornu spirals, and so a description of the technique used here to reconstruct the image of an object illuminated by x-rays, namely propagation-based x-ray phase contrast imaging, is provided. As discussed in Chapter 3, imaging with high-frequency radiation presents one with the phase problem, which is more difficult with regards to x-ray imaging, when compared to the case for visible light. Solutions to this problem are discussed here. Finally, methods for the analysis of the reconstructed wavefield that are relevant here, namely virtual optics, are discussed before continuing with the published work itself.

4.1 Introduction and background theory

4.1.1 Geometrical representation of optical fields

In Chapter 1 we saw that an electromagnetic field can be described as a wave propagating through space, obeying the d'Alembert equation. Here we describe an alternate representation of electromagnetic fields at small wavelengths, or in the 'shortwave limit'. The electromagnetic fields associated with the propagation of visible light, called optical fields, are characterized by rapid oscillations which correspond to wavelengths on the order of 10^{-6} m. X-rays, which are smaller still, with a wavelength mostly ranging from 10^{-8} m to 10^{-11} m, are also considered an optical field. For many optical problems, it is adequate to abandon the finiteness of the wavelength and use an alternate description of light which embodies the field of geometrical optics.

Consider the propagation of an optical field from the perspective of its wavefronts, which are surfaces of constant phase, illustrated in both Figs. 2.3 and 2.4, to which the direction of propagation is always perpendicular. The shape of the wavefront, in the absence of any scatterers, depends on the geometry of the source. A point source will emanate spherical wavefronts; a line source, such as from a fluorescent tube or some boundary wave, a cylindrical wavefront. The simplest form is the plane wave, which is an approximation that many waves take in a sufficiently localized region of space. Geometrical optics describes light in terms of rays which are perpendicular to the light's wavefront, traveling locally in the direction of the energy flow. In the case of light traveling as a plane wave, the geometric rays are parallel to one another, as is seen with the incident rays illustrated in Fig. 2.1, which appears in Sec. 2.1.1.

The path of the ray can be calculated using Fermat's principle which, as previously mentioned, is akin to the principle of least action, insofar as it states that the optical path length of a ray between two points will be shorter than along any other curve that joins these points and which lies in a regular neighbourhood of it. A 'regular neighbourhood' is one that is covered by rays in such a way that only one ray passes through each point of it (Born and Wolf, 1999).

Geometrical optics provides an accurate description of the reflection, refraction and absorption of light rays. Being thousands of years old, its applications are vast. For further reading of the numerous applications of geometrical optics, see any standard textbook on optics, such as those written by Born and Wolf (1999) and Hecht (2002). It is relevant to this thesis, though, to mention that geometrical optics can be used to predict behaviour of light in the presence of lenses and other optical elements, with applications such as the determination and correction of lens aberration (Allen et al., 2001a; Allen et al., 2001b; Faulkner et al., 2003).

A limitation of geometrical optics is its failure to predict any field in shadow regions. This is due to its inability to account for the wave-like properties of light in the geometric approximation, namely diffraction and interference. Developed by Joseph Keller (Keller, 1962), the geometrical theory of diffraction (GTD) assumes that light travels in rays, as with geometrical optics, and introduces diffracted rays. These are produced by incident rays which hit or graze edges, corners and vertices of boundary surfaces. Some of these rays will enter the shadow region, accounting for the light there, and others will enter the illuminated regions.

The GTD is sufficient for the analysis of a large number of diffraction scenarios, including diffraction by an aperture in a thin screen (Keller, 1957) and in a hard screen (Karp and Keller, 1961), and diffraction by a smooth object (Levy and Keller, 1959) and a round-ended object (Keller, 1959).

The methods for calculating an optical field using GTD, essentially a systematic generalization of Fermat's principle, is explored in greater details in Chapter 4.

The development of GTD represents a major breakthrough for the evaluation of a wide variety of high-frequency electromagnetic radiation and scattering problems. However, it is limited by the fact that GTD fails at the transition regions adjacent to the geometrical shadow boundaries, called the shadow-boundary (SB) transition region. This is due to the fact that, at these regions, the field departs from purely ray-optical behaviour. GTD, as a purely geometric theory, therefore experiences singular behaviour there (Pathak, 1982).

To overcome the limits of GTD which occur at SB transition regions, a uniform version of the theory was developed, known as the 'uniform geometrical theory of diffraction' (UTD)

(Kouyoumjian et al., 1981). This theory requires that the total high frequency field be continuous at SB regions and removes the restriction that the diffracted field remain ray-optical there. Whereas GTD cannot account from the departure from ray-optical behavior, UTD is allowed to become discontinuous at these problem regions, compensating for the discontinuities experiences by GTD there. This uniform theory reduces to ordinary geometrical optics away from the SB transition regions (Kouyoumjian et al., 1981; Pathak, 1982).

UTD has many applications and has been successful in, for instance, the design of large reflector antennas; the prediction of radiation patterns of antennas on aircraft, ships, missile and satellite configurations; the prediction of radar cross-sections of complex targets; and in the finding of solutions to the problem of discontinuities in waveguides. For further reading on these and other applications of UTD, see (Pathak et al., 2013).

In the publication in Sec. 4.2, it is shown that GTD is useful in predicting diffracted wavefields resulting from hard x-rays being incident upon various objects. The Argand-plane mappings induced by these wavefields take the form of generalised Cornu spirals.

4.1.2 The Cornu spiral in literature

The Cornu spiral was described in Sec. 1.3.2 as a simultaneous parametric plot of the Fresnel integrals and as representing the diffraction from the edge of a half-plane. Historically, it has been used to evaluate Fresnel integrals, but this application is now a curiosity owing to the proficiency of computers at this task. The spiral does, however, provide a visualisation of Fresnel diffraction, and might be used as a complementary visual aid in the analysis of Fresnel diffraction. In generalising the Cornu spiral, it might be possible to use them to study diffraction patterns due to objects that are more complex than the half-plane. Morgan et al. (2010) predicted the generalised Cornu spiral corresponding to diffraction from a cylindrical edge and the publication in Sec. 4.2 goes a step further by addressing diffraction from more complicated objects.

The terms ‘Cornu spiral’ and ‘generalised Cornu spiral’ appear sparsely throughout the literature. Ali et al. (1995; 1999) generalised the curvature profile of the Cornu spiral to form a function of arc length that can be used to facilitate control of the curve. This has

applications for the synthesis of curves with computer-assisted design (CAD) for architects and engineers. Cross and Cripps (2015) facilitated the practical use of generalised Cornu spirals in order to synthesise curves from within CAD.

An example concerning electromagnetic waves can be found with Hitachi (2012), who uses the Cornu spiral to study diffraction effects in ultrasound radiation. Specifically, Hitachi using the Cornu spiral to study ‘Babinet’s principle’, which informs the relationship between a rectangular slit U_1 and a rectangular obstacle U_2 . When the two objects are complementary to each other, i.e. where $U_1 + U_2 = 1$, Babinet’s principle states that the resulting field far downstream of the obstacle is equal to field observed for the complementary object. By drawing phasors onto the Argand plane, Hitachi is able to directly confirm this principle, showing aspects of diffraction that are difficult to observe directly.

4.1.3 Propagation-based x-ray phase contrast imaging

As stated earlier, we make the transition from visible light to x-rays in this chapter. In Sec. 4.2, the Cornu spiral is experimentally constructed using hard x-rays. This is done by imaging x-rays incident upon a straight edge. In addition, the same is done for x-rays incident on a cylinder and on a sphere embedded within a cylinder, with each scenario producing a generalised Cornu spiral in the Argand plane.

X-rays are electromagnetic vibrations similar to visible light but with a much smaller wavelength and a great penetrating power. Various methods of x-ray imaging take advantage of this power, relying on the absorption of x-rays by the object of interest. This absorption of the incident radiation results in a drop in intensity; these intensity variations are converted into a form that is visible. Radiography uses x-ray radiation to view the internal structure of a non-uniform, opaque object. X-rays are passed through the object and are absorbed to various degrees depending on the density and compositions of the object in question. The transmitted rays are then captured by a detector, which provides a two-dimensional representation of the internal structure. Traditional medical film radiography generally relies on simple shadow casting and uses the chemical changes

in the film, that are induced by the incident x-rays, to render the intensity variations visible.

Tomography is a technique whereby the source and the detector are shifted to produce sectional images in such a manner that a 3-D representation is constructed. With the advent of the CT (computed tomography) scanner, tomographic reconstruction is done by computer. This has ensured the prolific use of CT scanners in medical imaging. Sectional imaging of this kind requires a large amount of data to reconstruct a single image and, as such, many algorithms for CT make some compromise between accuracy and reconstruction time (Herman, 2009).

Pertinent to the topic of absorption imaging is the use of contrast agents, which has the function of improving the visibility of soft bodily structures in techniques such as radiography, CT and fluoroscopy. Common contrast agents include iodine and barium. Iodine, which is commonly administered intravenously, is used for arterial and venous investigations, for example. Barium is mostly used to image the gastrointestinal tract.

However, for samples with low x-ray absorption, such as soft biological tissue, these techniques do not suffice. There are other imaging techniques used to overcome this, such as magnetic resonance imaging (e.g. Watson et al., 2016; Silva et al., 2016) and positron emission tomography (e.g. Lucas et al., 1999; Schuetze et al., 2005). There are also several x-ray imaging techniques for objects with low absorption that fall into the category of ‘phase-contrast imaging’, in that they employ methods to render the phase variations imparted on the radiation by the object of interest visible as variations in intensity.

The technique of Zernike phase contrast, in its simplest incarnation, uses a non-absorbing thin film of uniform distribution in the back focal plane, which has a phase-shifting non-absorbing dot at its centre, to impose a phase shift on the beam that is passing through it (Zernike, 1942). This has the effect of adding a complex constant to every point in the input disturbance. The phase variations imposed on the input plane are seen as intensity variations at the output plane. Experimental implementation of x-ray Zernike phase contrast was first accomplished by Schmahl et al. (1991) and Schmahl et al. (1994), followed by numerous other implementations, such as by Neuhäusler et al. (2003).

Another method of introducing phase contrast involves the use of analyser crystals to yield phase contrast, known as ‘analyser-based phase contrast’. This technique involves placing a monochromator, usually a crystal, in front of the sample to be imaged, the function of which is to select a small frequency band from the incident radiation. The monochromated beam then strikes an analyser crystal that is positioned between the sample and the detector, yielding the desired phase contrast. This method was first demonstrated by Förster et al. (1980) and related work has been published by Somenkov et al. (1991), Davis et al. (1995a; 1995b) and Ingal and Beliaevskaya (1995). Examples of subsequent experiments have been performed using the analyser-based method to produce a phase-contrast image can be found with Pagot et al. (2003), Bravin (2003), Vine et al. (2007) and Coan et al. (2010). Synchrotron radiation is preferred for analyser-based imaging, which requires the incident radiation to be almost parallel and monochromatic with a particular energy bandwidth for the crystal (Diemoz et al., 2012).

Propagation-based phase contrast imaging (PBI) has the simplest set-up of all phase-contrast methods (Diemoz et al., 2012) as it does not require any additional optical elements between the source and the detector. The act of free-space propagation over a suitable distance produces the desired contrast, rendering phase variations that are accumulated by radiation as it passes from one side of a non-absorbing object to another visible as intensity variations (Wilkins et al., 1996; Cloetens et al., 1996; Kitchen et al., 2008; Beltran et al., 2010). This is the imaging technique used to produce the results in Sec. 4.2, and so it will be described in detail here.

In simulating the forward problem for propagation-based x-ray phase contrast imaging, it is first necessary to employ a method that can predict the phase and amplitude variations introduced upon the passage of light through the object. The projection approximation does this.

Figure 4.1 shows a monochromatic plane wave emanating from an x-ray source on the far left. The plane wave is visualized as a series of parallel arrows that are incident upon a scatterer lying in the space $0 < z < z_0$. The spaces $z < 0$ and $z > z_0$ are assumed to be free of charges and current.

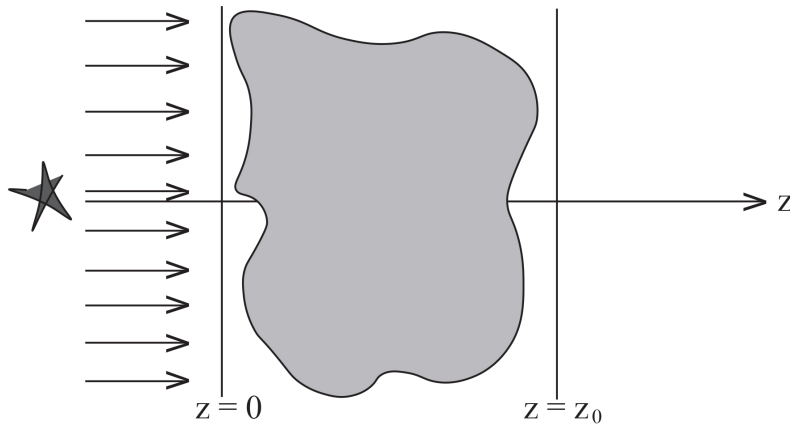


Figure 4.1: A z -directed monochromatic plane wave is incident upon a scatterer which lies between the $z = 0$ and $z = z_0$ planes.

In using the projection approximation, it is assumed that all scatterers that lie in the scattering volume are weak enough so that ray paths visualised in Fig. 4.1 are only perturbed negligibly. Via the projection approximation, the wavefield at $z = 0$ is given by:

$$\tilde{\psi}_\omega(x, y, z = z_0) \approx \exp\left(-ik \int_{z=0}^{z=z_0} [\delta_\omega(x, y, z) - i\beta_\omega(x, y, z)] dz\right) \tilde{\psi}_\omega(x, y, z = 0), \quad (4.1.1)$$

where $\tilde{\psi}_\omega$ is the envelope that, when multiplied by the unscattered plane wave $\exp(ikz)$, giving the total wavefield ψ_ω . The complex refractive index n_ω is given by:

$$n_\omega = 1 - \delta_\omega + \beta_\omega, \quad (4.1.2)$$

where δ_ω and β_ω are real numbers. The phase shift imparted on the wavefunction upon its passage through to the exit surface of the object is given by

$$\Delta\phi(x, y) = -k\delta_\omega T(x, y), \quad (4.1.3)$$

where $T(x, y)$ is the projected thickness of the object, and the intensity of the exit surface wavefunction is given by:

$$I_\omega(x, y, z = z_0) = \exp[-\mu_\omega T(x, y)] I_\omega(x, y, z = 0), \quad (4.1.4)$$

where $\mu_\omega = 2k\beta_\omega$.

For a full derivation of the projection approximation, see Paganin (2006).

The resulting complex analytic expression for the exit-surface wavefunction can be constructed from these phase and intensity expressions, as:

$$\psi_\omega(x, y, z = 0) = \sqrt{I_\omega(x, y, z = 0)} \exp[i\phi_\omega(x, y, z = 0)], \quad (4.1.5)$$

where the phase and intensity of the exit surface wavefunction is taken simply as their variations accumulated via the passage of light through the object.

Obtaining the intensity of the wavefunction at a distance $z = \Delta$ requires the free-space propagation of the exit-surface wavefunction via use of the Fresnel diffraction integral, previously given in Eq. 2.1.6:

$$\psi_\omega(x, y, z = \Delta) = \exp(ik\Delta) \mathcal{F}^{-1} \exp\left[\frac{-i\Delta(k_x^2 + k_y^2)}{2k}\right] \mathcal{F} \psi_\omega(x, y, z = 0), \quad \Delta \geq 0, \quad (4.1.6)$$

where $\psi_\omega(x, y, z = \Delta)$ is the wavefield that results from propagating the initial disturbance $\psi_\omega(x, y, z = 0)$ through a distance of $\Delta \geq 0$. \mathcal{F}^{-1} and \mathcal{F} denote the inverse Fourier transform and the Fourier transform operators, respectively, k is the wavenumber and (k_x, k_y) are the Fourier-space coordinates of the wavefield.

If the propagation distance Δ is small enough, the second exponential term in Eq. 4.1.6 can be approximated to

$$1 - \frac{i\Delta(k_x^2 + k_y^2)}{2k}. \quad (4.1.7)$$

Using the form of the exit-surface wavefield as per Eq. 4.1.5, the propagated wavefield can be expressed as:

$$\psi_\omega(x, y, z = \Delta) = \exp(ik\Delta) \left[1 + \frac{i\Delta\nabla_\perp^2}{2k}\right] \sqrt{I_\omega(x, y, z = 0)} \exp[i\phi_\omega(x, y, z = 0)], \quad (4.1.8)$$

using the Fourier derivative theorem. The transverse Laplacian is denoted by $\nabla_{\perp}^2 = \partial^2/\partial x^2 + \partial^2/\partial y^2$. The desired intensity can be calculated by taking the magnitude squared of the wavefield at $z = \Delta$, and may be manipulated into the following form (Paganin, 2006):

$$I_{\omega}(x, y, z = \Delta) = I_{\omega}(x, y, z = 0) - \frac{\Delta}{k} \nabla_{\perp} \cdot [I_{\omega}(x, y, z = 0) \nabla_{\perp} \phi_{\omega}(x, y, z = 0)], \quad (4.1.9)$$

showing that the intensity of the wavefield at some distance of $\Delta \geq 0$ from the exit surface, recorded as a propagation-based phase contrast image, is related to both the intensity and phase variation accumulated by illuminated radiation upon its passage through the object being imaged. Equation 4.1.9 is a form of the transport-of-intensity equation, which will be discussed in the next section in the context of phase retrieval.

4.1.4 Phase retrieval

The phase problem was defined in Sec. 3.1.2. In Sec. 4.1.3 phase contrast was described as means by which phase shifts on a beam of light can be seen as variations in intensity. The intensity of a phase-contrast image is, in general, a function of both the intensity and the phase of the input wavefield. Phase retrieval goes a step further than phase-contrast imaging, recovering the phase from one or more phase contrast images.

There are several algorithms that can accomplish this task, some of which will be discussed here. The Gerchberg-Saxton algorithm (Gerchberg and Saxton, 1972) is an iterative method involving Fourier transformation back and forth between the object of interest and the Fourier domain, and the application of constraints due to the measured data within each domain (Fienup, 1982). A number of applications are listed in Fienup, 1984. This method is useful in the reconstruction of non-crystalline samples, given a far-field diffraction pattern (Paganin, 2006).

Another method uses the transport-of-intensity (TIE) equation, which describes the flow of intensity along the optical axis of propagation light waves. It outlines the relationship between the phase of the object plane $\phi(x, y, z)$ and the first-order derivative of the intensity $I(x, y, z)$, with respect to the optical axis. The TIE is given by Teague (1983):

$$\nabla_{\perp} \cdot [I(x, y, z) \nabla_{\perp} \phi(x, y, z)] = -k \frac{\partial I(x, y, z)}{\partial z}. \quad (4.1.10)$$

Various methods of phase retrieval using algorithms based on the TIE can be found in (Gureyev and Nugent, 1996; Paganin and Nugent, 1998; Gureyev and Nugent, 1997). Each of these methods employ intensity measurements to estimate the right side of the TIE, as well as I on the left side, leaving a differential equation that has only the desired phase as its unknown. One such method, developed by Paganin et al. (2002), requires a single PBI image, and is the method used throughout the paper in Sec. 4.2. This algorithm assumes that the sample to be imaged is comprised of a single homogeneous material that is imaged under paraxial coherent x-ray radiation. Under these assumptions, the expressions for the phase and intensity variation imparted on light upon passage through such a material, as given by Eqs. 4.1.3 and 4.1.4, can be used together with the TIE to give the equation for single-image phase retrieval, as derived by Paganin et al. (2002):

$$T(\mathbf{r}_{\perp}) = -\frac{1}{\mu} \log_e \left(\mathcal{F}^{-1} \left\{ \mu \frac{\mathcal{F}\{M^2 I(M\mathbf{r}_{\perp}, z = R_2)\}}{R_2 \delta|\mathbf{k}_{\perp}|^2 / M + \mu} \right\} \right), \quad (4.1.11)$$

where R_2 is the distance between the contact image $I(\mathbf{r}_{\perp}, z = 0)$ and the phase contrast image $I(\mathbf{r}_{\perp}, z = R_2)$, $M = (R_1 + R_2)/R_1$ is the magnification of the contact image resulting from illumination of the object by a point source at a distance of R_1 behind the object, and $\mathbf{r}_{\perp} = (x, y)$ are the Cartesian coordinates over a plane perpendicular to the optic axis z .

Beltran et al. (2010) extended the algorithm of Paganin et al. to allow for the tomographic imaging of samples comprised of more than one material, under the condition that the various materials are spatially quantized. This algorithm has been used in numerous studies on phase-contrast imaging, such as Mayo et al. (2003) and Gureyev et al. (2006), and has been shown to be quite robust in the presence of noise, making it a good choice here.

4.1.5 Virtual optics

In the area of x-ray crystallography, the diffraction pattern generated by x-rays falling upon a small crystalline sample can be used to decode the structure of the crystal. The

result is called the ‘image’ of the crystalline sample, even though it is not a direct image. The technique of tomography also uses indirect imaging, building a three-dimensional reconstruction of a sample from two-dimensional projection images, as does in-line holography, generating the full wavefield information from its diffraction pattern.

In all of these instances, a computer forms part of the imaging system, which is a two-step process: First, data is obtained using hardware, and second, the output obtained is used to computationally reconstruct the sample information. This class of imaging systems employ what is known as ‘virtual optics’ (Lichte et al., 1992; Lichte et al., 1993; Paganin et al., 2004). It is so called since the process of forming an image is done using computer software rather than optical hardware. In the example of in-line holography, the full information of the wavefield at the exit surface ($z = z_0$ plane from Fig. 4.1) is desired. Once this information is known, the projected structure of the object can be determined. A three-dimensional refractive index may then be constructed for the object if the object is imaged under a number of different sample orientations (Paganin, 2006).

To go a step further than this, once the full information of the field is obtained, software can be used to simulate the action of some subsequent imaging system that might take such a field as its input. Virtual optics can be used even in cases where the hardware that would correspond to such an imaging system is difficult or impossible to construct. Paganin et al. (2004) coined the term ‘omni optics’ to describe this concept, due to its flexibility, and demonstrated the three-stage method for constructing such a virtual field: (i) Determining the propagation-based phase contrast image of a single material object, (ii) using propagation-based phase-contrast image to reconstruct the wavefield at the exit surface of the object, and (iii) using the reconstructed wavefield information to construct a virtual x-ray field. Guehrs et al. (2009) have used reconstructed holographic information to generate images using this sort of numerical processing in order to achieve particular types of contrast, and similar methods are employed by Li et al. (2008), Schot et al. (2015) and Zuo et al. (2015).

This three-step method described by Paganin is used in Sec. 4.2 in order to achieve the desired phase contrast which was limited by the hardware.

4.2 Generalised Cornu spirals: An experimental study using hard x-rays

On the following pages is inserted the as-published form of the third of three first-author papers arising from this thesis. The paper has been published as:

F. Werdiger, M. J. Kitchen and D. M. Paganin, 'Generalised Cornu spirals: An experimental study using hard x-rays', *Opt. Exp.* **24**, 10620–10634 (2016).

Generalised Cornu spirals: an experimental study using hard x-rays

Freda Werdiger,* Marcus J. Kitchen, and David M. Paganin

School of Physics and Astronomy, Monash University, Victoria 3800, Australia

Abstract: The Cornu spiral is a graphical aid that has been used historically to evaluate Fresnel integrals. It is also the Argand-plane mapping of a monochromatic complex scalar plane wave diffracted by a hard edge. We have successfully reconstructed a Cornu spiral due to diffraction of hard x-rays from a piece of Kapton tape. Additionally, we have explored the generalisation of the Cornu spiral by observing the Argand-plane mapping of complex scalar electromagnetic fields diffracted by a cylinder and a sphere embedded within a cylinder.

© 2016 Optical Society of America

OCIS codes: (260.1960) Diffraction theory; (340.0340) X-ray optics; (070.2580) Paraxial wave optics; (110.3175) Interferometric imaging; (120.5050) Phase measurement; (260.6042) Singular optics; (350.6980) Transforms.

References and links

1. J. B. Keller, "Geometrical theory of diffraction," *J. Opt. Soc. Am.* **52**, 116–130 (1962).
2. K. S. Morgan, K. K. W. Siu, and D. M. Paganin, "The projection approximation and edge contrast for x-ray propagation-based phase contrast imaging of a cylindrical edge," *Opt. Exp.* **18**, 9865–9878 (2010).
3. F. Rothschild, M. J. Kitchen, H. M. L. Faulkner, and D. M. Paganin, "Duality between phase vortices and Argand-plane caustics," *Opt. Commun.* **285**, 4141–4151 (2012).
4. F. Rothschild, A. I. Bishop, M. J. Kitchen, and D. M. Paganin, "Argand-plane vorticity singularities in complex scalar optical fields: an experimental study using optical speckle," *Opt. Exp.* **22**, 6495–6510 (2014).
5. H. S. Green and E. Wolf, "A scalar representation of electromagnetic fields," *Proc. Phys. Soc. A* **66**, 1129–1137 (1953).
6. M. V. Berry and M. R. Dennis, "Topological events on wave dislocation lines: birth and death of loops, and reconnection," *J. Phys. A: Math. Theor.* **40**, 65–74 (2007).
7. M. V. Berry, "Optical currents," *J. Opt. A: Pure Appl. Opt.* **11**, 094001 (2009).
8. M. J. Kitchen, D. M. Paganin, R. A. Lewis, N. Yagi, K. Uesugi, and S. T. Mudie, "On the origin of speckle in x-ray phase contrast images of lung tissue," *Phys. Med. Biol.* **49**, 4335–4348 (2004).
9. S. Goto, K. Takeshita, Y. Suzuki, H. Ohashi, Y. Asano, H. Kimura, T. Matsushita, N. Yagi, M. Isshiki, H. Yamazaki, Y. Yoneda, K. Umetani, and T. Ishikawa, "Construction and commissioning of a 215-m-long beamline at SPring-8," *Nucl. Instr. Meth. Phys. Res. A* **467-468**, 682–685 (2001).
10. A. Momose, T. Takeda, Y. Itai, and K. Hirano, "Phase contrast x-ray computed tomography for observing biological soft tissues," *Nat. Med.* **2**, 473–475 (1996).
11. E. Förster, K. Goetz, and P. Zaumseil, "Double crystal diffractometry for the characterization of targets for laser fusion experiments," *Krist. Tech.* **15**, 133–136 (1980).
12. M. J. Kitchen, D. M. Paganin, K. Uesugi, B. J. Allison, R. A. Lewis, S. B. Hooper, and K. M. Pavlov, "Phase contrast image segmentation using a Laue analyser crystal," *Phys. Med. Biol.* **56**, 515–534 (2011).
13. F. Pfeiffer, O. Bunk, C. David, M. Bech, G. Le Duc, A. Bravin, and P. Cloetens, "High-resolution brain tumor visualization using three-dimensional x-ray phase contrast tomography," *Phys. Med. Biol.* **52**, 6923 (2007).
14. D. M. Paganin, S. C. Mayo, T. E. Gureyev, P. R. Miller, and S. W. Wilkins, "Simultaneous phase and amplitude extraction from a single defocused image of a homogeneous object," *J. Microsc.* **206**, 33–40 (2002).
15. F. Zernike, "Phase contrast, a new method for the microscopic observation of transparent objects," *Physica* **9**, 686–693 (1942).
16. D. M. Paganin, T. E. Gureyev, S. C. Mayo, A. W. Stevenson, Ya. I. Nesterets, and S. W. Wilkins, "X-ray omni microscopy," *J. Microsc.* **214**, 315–327 (2004).

17. E. Gullikson, "X-ray interaction with matter," http://henke.lbl.gov/optical_constants/
18. L. Mandel and E. Wolf, *Optical Coherence and Quantum Optics* (Cambridge University, 1995).
19. M. R. Dennis and J. B. Götte, "Topological aberration of optical vortex beams: Determining dielectric interfaces by optical singularity shifts," *Phys. Rev. Lett.* **109**, 183903 (2012).
20. M. R. Dennis and J. B. Götte, "Beam shifts for pairs of plane waves," *J. Opt.* **15**, 104015 (2013).
21. T. C. Petersen, A. I. Bishop, S. A. Eastwood, D. M. Paganin, K. S. Morgan, and M. J. Morgan, "Singularimetry of local phase gradients using vortex lattices and in-line holography," *Opt. Exp.* **24**, 2259–2272 (2016).
22. O. V. Angelsky, M. P. Gorsky, P. P. Maksimyak, A. P. Maksimyak, S. G. Hanson, and C. Yu. Zenkova, "Investigation of optical currents in coherent and partially coherent vector fields," *Opt. Express* **19**, 660–672 (2011).
23. K. M. Pavlov, D. M. Paganin, D. J. Vine, J. A. Schmalz, Y. Suzuki, K. Uesugi, A. Takeuchi, N. Yagi, A. Kharchenko, G. Blaj, J. Jakubek, M. Altissimo, and J. N. Clark, "Quantized hard x-ray phase vortices nucleated by aberrated nanolenses," *Phys. Rev. A* **83**, 013813 (2011).

1. Introduction

The Cornu spiral is, in essence, an Argand-plane representation of the Fresnel diffraction of light that is normally incident upon an infinite opaque edge. Historically, it was used as a graphical aid for the calculation of the Fresnel integrals associated with this diffraction. Figure 1(a) shows the Argand-plane plot of the complex optical field which results from a plane wave diffracting from a semi-transparent thin aluminium screen. Adopting the perspective of Keller's geometrical theory of diffraction [1], (i) the bottom right lobe of the spiral in Fig. 1(a) corresponds to the phasor associated with cylindrical waves scattered from the diffracting edge into the region of geometrical shadow; while (ii) the top left lobe results from the coherent superposition of the incident plane wave phasor with the scattered cylindrical edge wave.

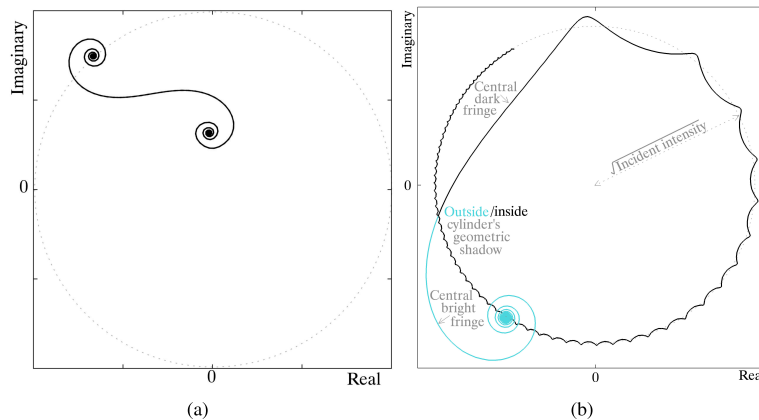


Fig. 1. (a) A Cornu spiral resulting from the Argand-plane mapping of a monochromatic plane wave diffracted by a partially absorbing aluminium half-plane screen (the dotted line is a unit circle that represents the unscattered plane wave), and (b) a hypocycloid resulting from a monochromatic plane wave diffracted by a partially absorbing cylinder, described by Morgan *et al.* [2]. The diffracted light that emerges outside the geometric shadow of the cylinder is indicated in blue.

Morgan *et al.* [2] described such a mapping of diffraction from a cylindrical edge. This is demonstrated in Fig. 1(b), which shows the simulated Argand mapping of a monochromatic plane wave diffracted by a partially absorbing cylinder. The resulting wavefield takes the form of a hypocycloid when mapped to the Argand plane. There, the lobe on the bottom left (blue), representing the outside of the cylinder where the diffraction pattern lies against the unscattered plane wave, is identical to that of a screen. Crossing the edge of the cylinder, however, the changing thickness of the cylinder causes the Argand-plane trace to evolve into a hypocycloid

(black): As the thickness of the cylinder increases, the phase accumulated by passage of the light ray through the cylinder increases in magnitude, causing the one-dimensional trace to rotate in the Argand plane. At the same time, the intensity decreases as more of the incident light is absorbed, causing the Argand trace to spiral in towards the origin. Finally, the light that is scattered from the edge of the cylinder interferes with the light that is incident upon the cylinder, resulting in oscillations in phase and intensity that decrease in amplitude as the distance from the edge increases.

Both the Cornu spiral and the Cornu-come-hypocycloid in Figs. 1(a) and 1(b) are one-dimensional traces embedded in two-dimensional Argand space; while the thickness varies across the cylinder, it retains the one-dimensional nature of the straight edge when projected onto a two-dimensional surface. In order to find a complex function that leaves a two-dimensional image of x - y space in the Argand plane, we need to add a higher degree of spatial complexity to the object of interest. A sphere, when projected onto a surface, has a thickness that varies in both transverse dimensions. However, if the sphere is lying against a homogeneous background, such as the normally incident monochromatic plane wave, that distinction does not translate to a two-dimensional image in the Argand plane. By placing a sphere inside a cylinder, however, we can achieve the varying background necessary to evolve the Argand-plane trace into the sort of two-dimensional Argand-plane image seen in our previous works [3, 4].

Here, we experimentally reconstruct the Cornu spiral and two of its generalisations through the imaging of three objects with increasing complexity: the straight edge, cylinder and sphere-in-cylinder.

Section 2 will provide some background theory, namely Argand-plane mapping theory, including a description of vorticity singularities (Sec. 2.1), and the Geometrical Theory of Diffraction (GTD) (Sec. 2.2). We can use GTD to write down equations for the field downstream of each of the three objects to be imaged and to understand and predict the morphology of the Argand-plane mapping of each field. Section 3 includes the experimental results obtained using hard x-rays. Methods used for capturing images and processing the data are described in Sec. 3.1. Section 3.2 reports on the results of using a piece of Kapton tape to observe x-ray diffraction from a straight edge and subsequent Argand-plane mapping of the reconstructed field. Sections 3.3 and 3.4 do the same for an aluminium cylinder and a spherical bubble trapped in an agar-filled perspex cylinder. Section 4 discusses our results, including possible applications and plans for future work. We conclude with Sec. 5.

2. Theory

Here, we briefly review some relevant background theory, with the reader being referred to Refs [3] and [4] for further detail.

2.1. Argand plane mappings

For an arbitrary two-dimensional differentiable single-valued continuous complex function $\Psi(x, y)$, a mapping \mathcal{M} to the Argand plane is given by

$$\mathcal{M}(\Psi(x, y)) \rightarrow (\Psi_R, \Psi_I), \quad (1)$$

where Ψ_R and Ψ_I are the respective real and imaginary parts of $\Psi(x, y)$, which is here taken to be the boundary value of the spatial part of a forward-propagating three-dimensional monochromatic scalar wavefunction [5], evaluated over a planar surface.

For a complex wavefunction that lies in x - y space, there is in general a loss of information that occurs under a mapping \mathcal{M} to the Argand plane, rendering the mapping essentially non-invertible due to the mapping being many-to-one. In such cases, it is possible for a singularity to form under a mapping to the Argand plane.

In order to locate singularities induced by a many-to-one mapping \mathcal{M} to the Argand plane associated with $\Psi(x,y)$, we can define the Jacobian determinant (“Jacobian”) of \mathcal{M} as [4]

$$J(x,y) = \begin{vmatrix} \partial_x \Psi_R & \partial_y \Psi_R \\ \partial_x \Psi_I & \partial_y \Psi_I \end{vmatrix}. \quad (2)$$

The Jacobian of \mathcal{M} provides valuable information about the transformation of $\Psi(x,y)$. The absolute value of J at a point $P = (x_p, y_p)$ in x - y space gives the factor by which infinitesimal patches at p expand or contract under the transformation from real space to Argand space. The sign of J indicates whether a patch has been inverted ($J < 0$) or not ($J > 0$). A value of $J = 0$ indicates that an infinitesimal patch of space in the xy -plane has collapsed onto a single point under \mathcal{M} and a singularity of the Argand plane has formed for $\mathcal{M}(\Psi(x,y))$. Setting $J(x,y) = 0$ provides the location of all singularities of the mapping. The set \mathcal{S} of all (x,y) points for which $J(x,y) = 0$ maps to a hierarchy of singularities in Argand space, such as the fold, which is induced by, as the name suggests, a fold in the local image of x - y space along a single line of zero vorticity.

One can assign a physical meaning to the “zero lines” of the Jacobian and subsequent singularities in the Argand plane. The vorticity Ω of a three-dimensional complex scalar field $\Psi(x,y,z)$ can be expressed as [6, 7]

$$\Omega = \nabla \times \mathbf{j} = \text{Im}(\nabla \Psi^* \times \nabla \Psi) = \nabla \Psi_R \times \nabla \Psi_I, \quad (3)$$

where ∇ is the gradient operator and $\mathbf{j} = \text{Im} \Psi^* \nabla \Psi$ is the current up to a multiplicative constant, which is set to unity here. The vorticity quantifies the local rotation in the field. The z -component of the local vorticity,

$$\Omega_z = \frac{\partial \Psi_R}{\partial x} \frac{\partial \Psi_I}{\partial y} - \frac{\partial \Psi_I}{\partial x} \frac{\partial \Psi_R}{\partial y}, \quad (4)$$

represents the local current rotation at (x,y) and is equivalent to the Jacobian, as seen from Eq. 2. When the local current rotation changes from clockwise to anti-clockwise, implying that when $\Omega_z = 0$, a singularity will be induced by \mathcal{M} , due to the assumed continuity of the vorticity. Stated alternatively, the Jacobian zero lines are present where the vorticity has vanished.

2.2. Geometrical theory of diffraction

In observing the diffraction of x-rays from the hierarchy of objects defined here, it is necessary to define a theory that describes a diffracted light field. A consequence of the finite wavelength of light, diffraction is not a property described by Geometrical Optics (GO), which uses geometrical rays to calculate light fields accounting for the incidence, refraction and reflection of electromagnetic waves. The Geometrical Theory of Diffraction (GTD), however, adds to this a description of rays that are diffracted around edges and smooth objects. Introduced by Joseph B. Keller in 1953, this theory augmented GO by using geometric rays to describe wave diffraction [1]. GTD, like GO, assumes light travels in rays but introduces diffracted rays, which are produced by incident rays hitting or grazing the edges, corners or vertices of boundaries. Some of these enter the shadow region and others go into the illuminated regions, contributing to the light there. Diffracted rays can be calculated using a modified Fermat’s principle, assigning a phase to each ray and letting the total field at a given point be the sum of all complex rays passing through it.

We can use the geometrical theory of diffraction to describe the field downstream of a semi-opaque phase-amplitude screen illuminated by a monochromatic plane wave. The total field at

a point (x, y) will be the sum of all rays passing through that point, each of which can be placed into one of three categories: Those which have passed through the screen, having picked up a subsequent phase change equal to $-k\delta T$, where k is the wave number, $1 - \delta$ the refractive index of the screen material and T the projected thickness of the screen; those which have passed through uninterrupted, having incurred no phase change; finally, those which have scattered off the boundary of the screen, emanating in the form of a locally cylindrical wavefront, given that the source of the boundary wave is a line.

Thus we can state that for the field $\Psi(x, y)$ over an image plane lying perpendicular to the axis of propagation which is at a distance z from the exit surface of a semi-opaque screen of thickness T which has been illuminated by a rigidly-translating monochromatic plane wave with wavenumber k ,

$$\Psi(x, y) = e^{ikz} e^{-\mu T/2} e^{-ik\delta T} + \mathcal{A} \frac{e^{ikR}}{\sqrt{R}}, \quad (5)$$

where μ is the attenuation coefficient of the material, R is the distance from the point (x, y) in the image plane and the edge of the screen, and \mathcal{A} is the amplitude of the scattered wave. If the thickness of the screen varies in one transverse dimension, say the x - direction, we can write $R = \sqrt{x^2 + z^2}$. The two lobes of the Cornu spiral in Fig. 1(a) are due to the phasor addition of the cylindrical wave with the wavefront passing uninterrupted on the outside of the screen and with the wavefront transmitted through the screen.

In the case of a cylinder with radius R_c , whose axis is perpendicular to the optic axis, we can adjust Eq. (5) to account for two separate line sources for a cylindrical boundary wave, one on either side of the cylinder, and a thickness $T(x) = 2R_c \sqrt{R_c^2 - x^2}$ that varies across the object. Thus,

$$\Psi(x, y) = e^{ikz} e^{-\mu T(x)/2} e^{-ik\delta T(x)} + \mathcal{A} \frac{e^{ikR_1}}{\sqrt{R_1}} + \mathcal{B} \frac{e^{ikR_2}}{\sqrt{R_2}}, \quad (6)$$

where $R_1 = \sqrt{(x + R_c)^2 + z^2}$, $R_2 = \sqrt{(x - R_c)^2 + z^2}$. As x moves closer to the centre of the cylinder, T increases. Referring back to Fig. 1(b), the black lobe of the Cornu spiral unravels in the geometric shadow of the cylinder, due to the change in thickness. The oscillations in phase and intensity are brought about via the addition of phasors, accounting for the cycloidal motion of the Argand-plane trace.

Continuing with the hierarchy of objects investigated for diffraction in this paper, we can adjust Eqs. (5) and (6) to account for a sphere lying within the cylinder. In the event of a sphere normally illuminated by planar complex scalar electromagnetic waves, the source of the diffracted wave would be a ring following the outermost edge around the sphere. Theoretically, a ring source would result in a toroidal wavefront accounting for the diffraction from the edge of the sphere. For a point P lying in the x - y plane at some distance z from the sphere, the diffracted rays that pass through that point are a result of the locally toroidal wavefront emanating from the closest point on the circle. Figure 2.2 demonstrates this point.

Therefore we find that for a sphere of radius R_s lying within in a cylinder that is illuminated by a monochromatic plane wave, the field through a point $P(x, y)$ lying in the image plane at some distance z from the object is given by

$$\Psi(x, y) = e^{ikz} e^{-\mu T(x, y)/2} e^{-ik\delta T(x, y)} + \mathcal{A} \frac{e^{ikR_1}}{\sqrt{R_1}} + \mathcal{B} \frac{e^{ikR_2}}{\sqrt{R_2}} + \mathcal{C} \frac{e^{ik\tilde{R}_3}}{\sqrt{\tilde{R}_3}}, \quad (7)$$

where \tilde{R}_3 is the optical path length of the ray which possesses a geometrical path length given by $R_3 = \sqrt{(\sqrt{x^2 + y^2} - R_s)^2 + z^2}$. If the sphere is a bubble in the cylinder, the entire object

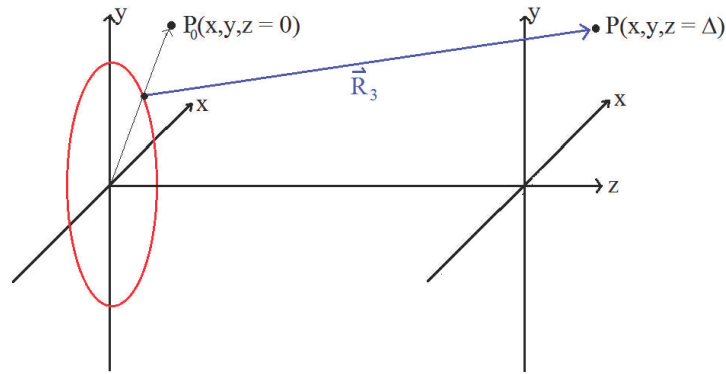


Fig. 2. For a sphere lying in the object plane, the source of the diffracted rays is a ring around the outermost edge (red). To find the contribution of the diffracted rays through point P lying at a distance of $z = \Delta$ from the object plane, we find the shortest distance from P in the image plane to the ring source in the object plane, defined by \mathbf{R}_3 . The diffracted rays through P are a result of a toroidal wavefront emanating from the point where \mathbf{R}_3 meets the ring.

can be a single material with a single refractive index $1 - \delta$ and attenuation coefficient μ , with projected thickness $T(x, y) = 2\sqrt{R_c^2 - x^2} - 2\sqrt{R_s^2 - x^2 - y^2}$.

3. Experimental realisation using hard x-rays

Here we present our experimental results, obtained using hard x-rays. Our reason for choosing this form of radiation is a long-term goal, which lies beyond the scope of the present paper, namely the application of Argand-plane analyses to improve methods for the speckle imaging of lung tissue using coherent x-ray images [8].

3.1. Experimental and analytical methods

The results in this section were obtained via x-ray experiments conducted using a 215m-long beamline (BL20B2) at the SPring-8 synchrotron radiation facility in Hyogo, Japan. The length of the beam allowed for a large field and spatially coherent beam [9]. At the end of the beamline, the distance from source to detector can be adjusted to allow for propagation-based phase contrast imaging (PBI) [9], which is used here to reconstruct the various objects that are featured in the following sections. A schematic of the experimental set-up is shown in Fig. 3. The technique used to obtain images used in this paper is PBI. Unlike other methods that adopt phase contrast, such as x-ray interferometry [10], analyser-based phase-contrast imaging [11, 12], or x-ray diffraction grating methods [13], PBI does not require the use of any additional optical elements between the sample and detector. The act of free-space propagation enables the phase shifts that the sample imposes upon the incident radiation to become visible.

Pertinent to the results presented in this section is the phase retrieval algorithm developed by Paganin et al. [14], which requires a single PBI image per projection. In applying this algorithm, we assume that the sample in question is comprised of a single homogeneous material imaged under paraxial coherent x-ray radiation.

An optical system, such as the system used in the methods described above, can also add specific contrast modes, such as Zernike phase contrast [15]. These techniques have widespread use in light microscopy, particularly for biological specimens, due to their usefulness in defining fine structure in the images. The introduction of certain appropriate optical elements in microscopy serves as a means to generate the desired mode of contrast; this is hard-wired into

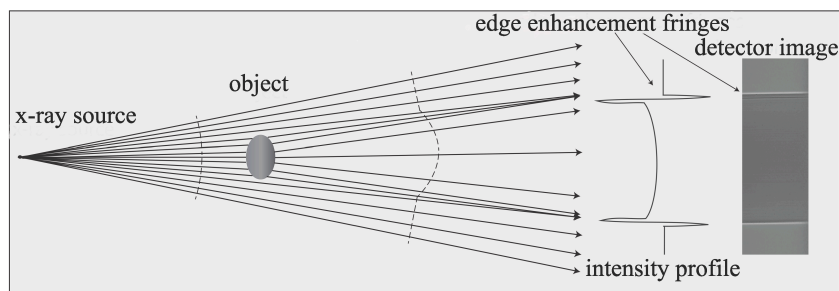


Fig. 3. The general set up of the experiments used to obtain results shown in Secs 3.2 - 3.4. The object to be imaged lies downstream of the x-ray source. The partially coherent light is then allowed to propagate further in order to observe edge enhancement via interference.

the experimental set-up. In holography, however the desired contrast mode can be generated numerically using virtual optics. The appropriate transfer function is used to simulate the analog of any optical element, given the boundary value of a forward propagating complex scalar electromagnetic wave over a given plane perpendicular to the optic axis. Thus, the computer becomes a part of the imaging system. This method was termed omni-microscopy and demonstrated using hard x-rays by Paganin *et al.* [16]. These methods are exploited in the following sub-sections to achieved the desired contrast. The complete wavefield information, obtained using experimental images, is subject to virtual optics, virtually propagated through space to obtain an appropriate amount of phase contrast. In particular, the wavefield derived in Sec. 3.4 is propagated beyond the limits of the particular experimental hardware involved in obtaining the original images.

3.2. Straight edge

In order to reconstruct a Cornu spiral, it was necessary to use an object with a straight edge and illuminate it with electromagnetic radiation to observe diffraction from the edge. A piece of Kapton (polyimide) tape was used for this purpose. The experiment was performed using 30 keV x-rays ($\mu = 35.05 \text{ m}^{-1}$, $\delta = 3.38 \times 10^{-7}$ [17]) to illuminate the sample. Figure 4(a), together with the profile plot in Fig. 4(b), shows the PBI image of the tape that was taken at a distance of 2.0 m from the sample with a 4000×2672 pixel Hamamatsu CCD camera (C9300-124) with a $16.2 \mu\text{m}$ pixel size. Single image phase retrieval [14] was used to construct an image of the tape at the exit surface, seen in Fig. 4(c). The noise is significant in the profile plot in Fig. 4(d). The resolution of the image was increased by a factor of two using cubic interpolation before using the angular spectrum formulation to forward propagate [18], employing virtual optics to observe a diffraction pattern. Figure 4(e) shows a forward propagation to 2.0 m. The profile plots of the original and simulated images at a distance of 2.0 m from the contact surface, Figs 4(b) and 4(f), respectively, closely resemble one another. The central fringe is brighter in Fig. 4(f), presumably a result of the increased resolution.

Figure 5(a) shows the intensity of the field forward-propagated with virtual optics to eight metres, where there are several fringes. This field is mapped to the Argand plane in Fig. 5(b), where the noise obscures the Cornu spiral, which has emerged due to the boundary wave. Integrating the image along 341 columns to produce a field that varies in only one spatial direction, a clean image of the Cornu spiral can be seen in Fig. 5(c). Cropping the image close to the edge of the tape, a clean Argand trace can be obtained.

Figure 6 shows the evolution of the trace with distance through 0.0 m, 2.0 m and 6.0 m. Diffraction fringes multiply upon virtual-optics propagation; oscillations in phase and inten-

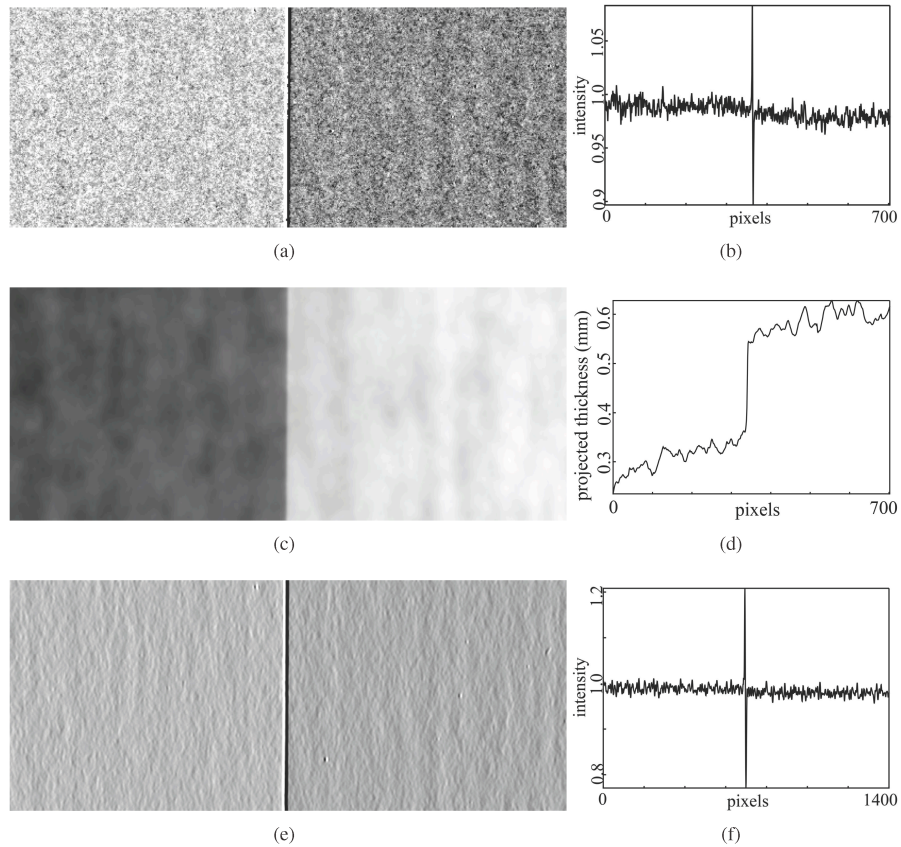
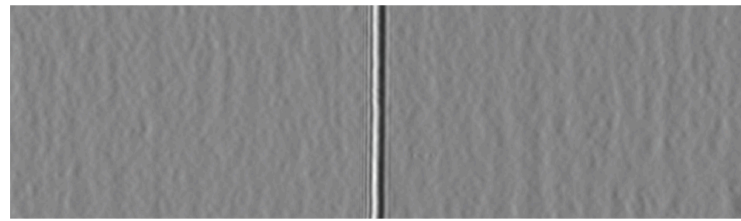


Fig. 4. (a) A $1.10\text{ cm} \times 0.24\text{ cm}$ image 2.0 m from a sample containing a piece of Kapton (polyimide) tape, taken using 24 keV x-rays. A profile plot of the raw image is shown in (b), wherein lies a single bright phase contrast fringe pair. Note as well the highly transmissive quality of the tape; (c) An image of the projected thickness of the tape, with a profile plot shown in (d), highlighting the low signal-to-noise ratio; (e) For comparison, a simulated image of the tape at 2.0 m is shown, along with a profile plot (f) showing the previously noted single bright fringe. The fringe in (f) appears brighter than the one in (d) as the pixel size was halved for the purpose of the simulation.

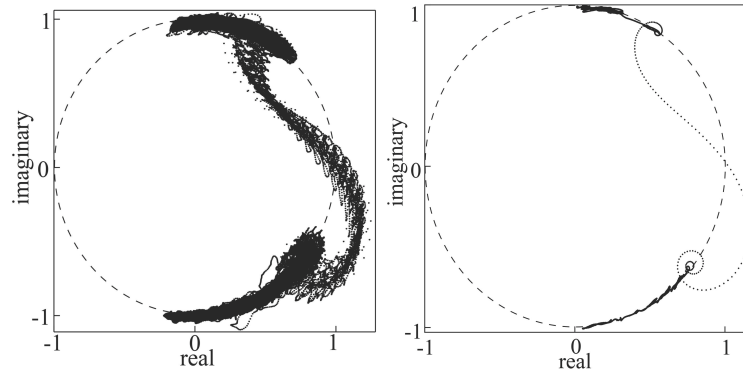
sity manifest at each end of the Cornu spiral. The characteristic bright central fringe becomes prominent in Fig. 6(b), at 2.0 m from the contact surface. Propagating further to 6.0 m , there are several fringes which are apparent in oscillations seen in Fig. 6(c). The arm that extends outside of the unit circle (dashed line) represents the outside of the Kapton tape which is occupied by the uninterrupted plane wave. Due to the low absorption coefficient and thickness (see Fig. 4(d)) of the material, only a very small amount of radiation is absorbed by the tape; both the uninterrupted and transmitted waves are close to unity and the Cornu spiral clings to the unit circle in each image.

3.3. Cylindrical edge

Further to the goal of generalising the Cornu spiral, we sought to observe its evolution upon the straight edge being replaced with a cylindrical one. Under these conditions, one side of the object would experience a varying phase and intensity, due to the changing thickness of



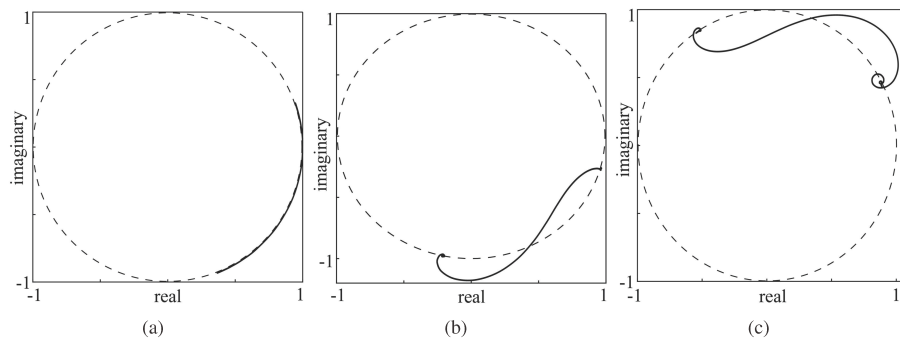
(a)



(b)

(c)

Fig. 5. (a) Intensity of the field forward propagated to 8.0 m, where several fringes are visible; (b) Argand mapping of the field propagated to 8.0 m, where the spiral is obscured by noise; (c) Argand mapping of the field after being summed and averaged along the vertical axis, showing a clean Cornu spiral.



(a)

(b)

(c)

Fig. 6. The evolution of the Cornu spiral with propagation distance: (a) 0.0 m, (b) 2.0 m and (c) 6.0 m. The spiral clings to the unit circle (dashed line) in each instance due to the low absorption of the Kapton tape. The field in (a) traces out an arc due to its smooth and continuous nature, rather than two discrete points representing either side of the tape.

the cylindrical object, which would deform the corresponding arm of the Cornu spiral. Figure 7(a) shows an image of a 3 mm aluminium cylinder taken with 24 keV x-rays using the Hamamatsu ORCA Flash C11440-52U fibre optic detector with a pixel size of $6.5 \mu\text{m}$. The sample-to-detector distance is 35 cm. At 24 keV, aluminium has an absorption coefficient of $\mu = 464.48 \text{ m}^{-1}$ and refractive index decrement $\delta = 9.398 \times 10^{-7}$ [17]. Observing a profile plot of the raw image, Fig. 7(b), a single fringe is seen on each side of the cylinder. Note as

well the effects of the point spread function (PSF) in the field as it approaches the edges of the cylinder. Using single-image phase retrieval, the projected thickness of the cylinder was reconstructed (Fig. 7(c)). Looking at the profile plot in Fig. 7(d), the fringes have been suppressed, as would be expected at the contact surface. The reconstructed image shows a cylinder diameter of approximately 3.25 mm. For comparison, the field at the exit surface was interpolated by a factor of four and then forward-propagated to 35 cm using the angular spectrum formula [18]. The intensity at 35cm is shown in Fig. 7(e), and a profile plot in Fig. 7(f). The noise has been suppressed and there is a single sharp peak at each boundary. The peak in Fig. 7(f) is higher than that in Fig. 7(b) due to the process of cubic interpolation whereby the number of pixels across the peak has been inflated by a factor of four. Note as well that there is no smearing of the point spread function.

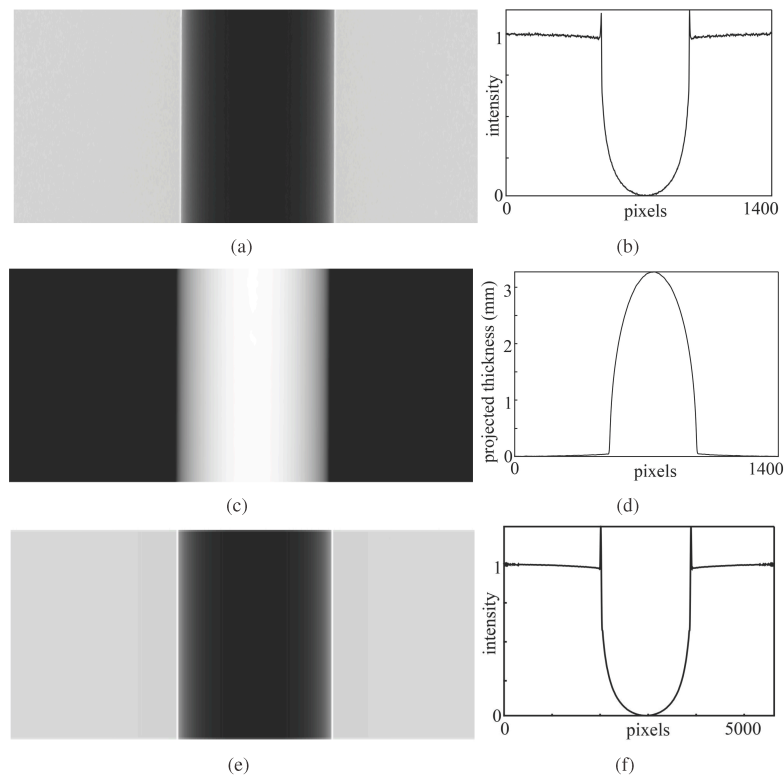


Fig. 7. (a) A $9.1 \text{ mm} \times 1.6 \text{ mm}$ image taken 35 cm downstream of an aluminium rod illuminated by 24 keV x-rays with a plot profile (b) showing a single bright fringe at the edge of the highly absorptive cylinder; (c) a reconstruction of the projected thickness of the rod and profile in (d); (e) forward propagation to 35 cm for comparison (the intensity is shown) and profile in (f) showing a brighter central fringe due to the interpolation as part of the simulation.

Figure 8 shows the Argand-plane mapping of the propagated field at various distances; 0.35 m, 1.0 m and 4.0 m. Diffraction fringes multiply as propagation distance increases, as with the Kapton tape in Sec. 3.2. Oscillations in phase and intensity on the outside of the cylinder manifest in the same way as with the straight edge of Fig. 6, spiraling in towards the value of the uninterrupted plane wave. Crossing the edge, the thickness of the sample increases, resulting in changes in phase and intensity, due to the subsequent refraction and absorption of the incident

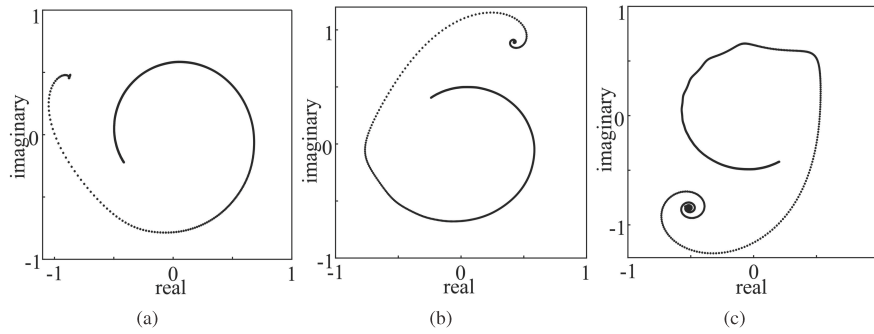


Fig. 8. Evolution of the Argand-plane mapping of the aluminium cylinder with propagation distance: (a) 35 cm, (b) 1.0 m and (c) 4.0 m. The spiral in each image represents the outside of the cylinder, where the intensity and phase oscillate against the unscattered plane wave. Within the cylinder, the varying phase causes the trace to move around the Argand plane as the thickness increases and the intensity falls to a minimum. The hypocycloid, as described in Fig. 1(b), is noticeable in (c).

radiation. This causes the trace to travel around the Argand plane, instead of being fixed around a constant background. This ultimately results in the hypocycloid that manifests in Fig. 8(c), at a distance of 4.0 m from the contact surface. At this distance, there is significant diffraction and the resulting phase and intensity oscillations stand out against a rapidly varying background.

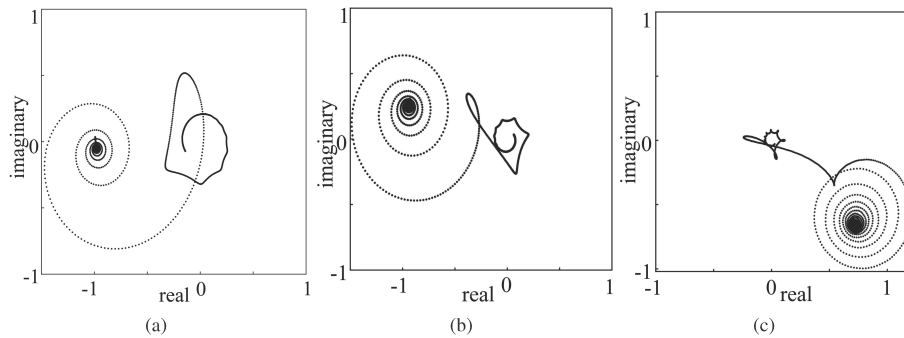


Fig. 9. The projected thickness is forward propagated using x-rays with reduced energy. (a) 18 keV x-rays propagated to 4.0 m; (b) 16 keV x-rays at 4.0 m; (c) 15 keV x-rays at 6.0 m. The retrograde motion of the Argand trace can be seen in (c). The lower energy rays have a higher absorption coefficient and diffract more heavily.

In order to observe the evolution of the hypocycloid under circumstances where there is significantly more diffraction, the energy of the x-rays used in the angular spectrum formula was reduced. For Fig. 9(a), the energy has been reduced to 18 keV ($\mu = 1132.0 \text{ m}^{-1}$, $\delta = 1.67 \times 10^{-6}$ [17]) and the wavefield allowed to propagate to 4.0 m before being mapped to the Argand plane. Drawing comparison with Fig. 8(c), which is also at 4.0 m from the contact surface, there are considerably more revolutions in the lobe at the bottom-left of Fig. 9(a) than in the corresponding lobe for Fig. 8(c), signifying more diffraction. Additionally, the hypocycloid noted in Fig. 8(c) is more dramatic in Fig. 9(a) due to the increased absorption at the energy. Decreasing the energy to 16 keV ($\mu = 1622.98 \text{ m}^{-1}$, $\delta = 2.12 \times 10^{-6}$ [17]) heightens this effect. Reducing again to 15 keV ($\mu = 1974.14 \text{ m}^{-1}$, $\delta = 2.41 \times 10^{-6}$ [17]) and propagating further to 6.0 m from the contact surface, increasing the diffraction from the edge of the cylinder, results in the retrograde motion of the Argand-plane trace described by Morgan *et al.* [2], seen in Fig. 9(c) [17].

3.4. Sphere-in-cylinder

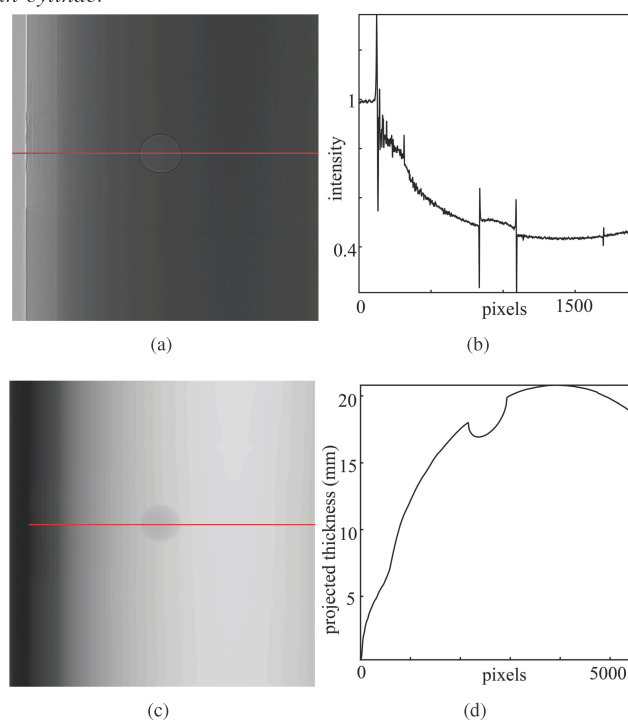


Fig. 10. (a) A $1\text{ cm} \times 1\text{ cm}$ image taken 2.0 m from a bubble trapped in a perspex cylinder filled with agar illuminated by 24 keV x-rays. A plot profile (b) taken along the red line in (a) shows the three distinct regions: air, perspex and agar. The reconstruction uses μ and δ for the latter; (c) The projected thickness is shown, with plot profile (d) taken along the red line in (c), within the boundary of the cylinder. Noise and fringes are suppressed.

In order to observe the evolution of the Argand-plane mapping from a one-dimensional trace to the fully-realized two-dimensional Argand mapping, we imaged a sphere embedded in a cylinder. A perspex cylinder was filled with a solution of 2% agar and a spherical air bubble was trapped in the solution as it set. The sample was then illuminated by 24 keV x-rays and a PBI image was captured using the ORCA Flash detector, as used to obtain the images in Sec. 3.3. Placing the detector at a distance of 2.0 m from the sample, the image in Fig. 10(a) was obtained. A profile plot in Fig. 10(a) shows some contrast at the boundaries between air, perspex and agar. As the aim was to obtain the Argand mapping of a sphere against a cylindrical background, the properties of the agar solution ($\mu = 46.95\text{ m}^{-1}$, $\delta = 4.00 \times 10^{-7}$ [17]) were used for single-image phase retrieval. The resulting projected thickness is shown in Fig. 10(c), and corresponding profile plot taken across the inside of cylinder in Fig. 10(d), where the fringes have been suppressed. The pixel size was reduced by a factor of four using cubic interpolation.

The field was numerically forward-propagated to 50 m to observe stark contrast between the bubble and its surroundings. The intensity at this distance is shown in Fig. 11(a). Figure 11(b) shows the profile plot across the mid-section of the bubble, showing some fringes at the boundary of the bubble. The Argand mapping of the bubble is shown in Fig. 11(c), where two small but distinct spiral-like structures are seen, separated due to the varying cylindrical background as well as the noise. Figure 11(d) shows a close-up image of the lower spiral-structure. This structure is the Argand mapping of a field normally incident on a sphere that is

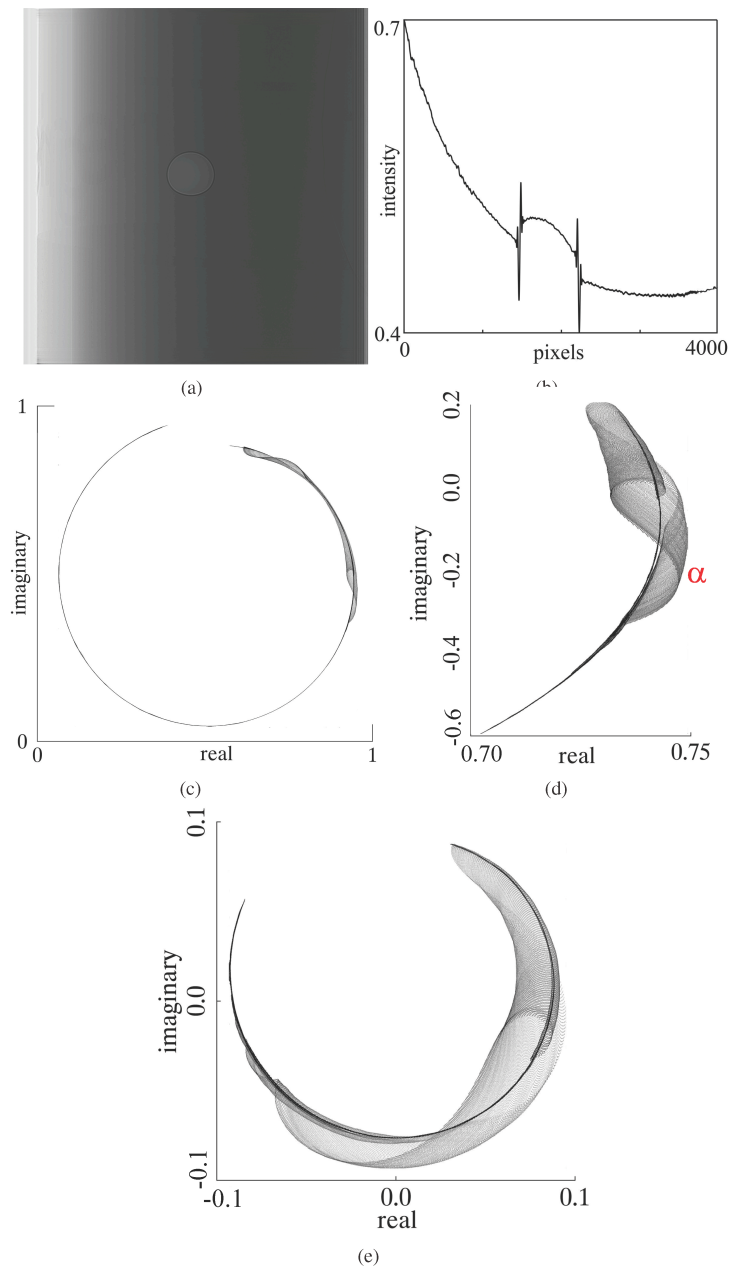


Fig. 11. (a) Image of the cylinder propagated to a distance of 50 m; (b) profile across the mid-section of the bubble, which has a strong signal at this distance; (c) Argand mapping of the bubble; (d) Close-up image of (c), with behaviour seen in fully-realized two-dimensional vorticity singularities, such as the fold singularity indicated by α ; (e) With energy halved to 12 keV, the x-rays diffract more strongly and are absorbed heavily, resulting in some hypocycloid behaviour seen on the left side of the image.

lying within a cylinder. It is effectively the Argand mapping resulting from light incident upon a series of infinitesimally flat cylinders, with varying radii, lying against a varying background that together map to the Argand plane in the form of this two-dimensional structure consisting of a continuous infinity of Cornu spirals.

In order to observe some hypocycloidal behaviour, the energy of the x-rays was halved to 12 keV for the angular spectrum formula. The result in Fig. 11(e) shows some such behaviour due to more extreme diffraction that is expected at this lower energy level. There is also greater absorption, with this spiral having a magnitude of approximately one tenth of that in Fig. 11(c).

It is with Figs. 11(c), 11(d) and 11(e) that we finally obtain Argand-plane singularities associated with configuration-space vorticity zeros. These structures, reminiscent of the caustics of geometric optics, are exemplified by the fold-type singularity marked α in Fig. 11(d). As previously explained, all such Argand-plane singularities correspond to the image of points (x, y) with both zero vorticity and zero Jacobian.

4. Discussion

Our previous works [3, 4] focused on vortical behaviour in continuous two-dimensional complex scalar wavefunctions and noted the existence of singularities induced by the associated mapping \mathcal{M} to the Argand plane – coined “vorticity singularities” as they correspond to lines of zero vorticity in the xy -plane. We have so far used singularities induced by \mathcal{M} to make general and particular observations about the behaviour of screw-type phase defects in complex scalar wavefunctions – such as the behaviour of the wavefield in and around vortex pairs.

At the same time, the field of “singularimetry” (a term coined recently by Dennis and Götte [19, 20]), is emerging as an important result of modern singular optics. The locality and stability of zeroes of an optical field makes them useful in measuring beam shifts to subwavelength-accuracy. More recent work by Petersen *et al.* [21] demonstrates the use of vortex lattices to determine small phase shifts imparted on the field by various spherical and cylindrical specimens. One also has recent experimental work on optical currents, such as that of Angelsky *et al.* [22] and Pavlov *et al.* [23].

Our work in this paper shifts the focus away from exclusively vortical fields, namely those with screw-type phase defects. The Cornu spiral, the Argand-plane mapping of the diffraction of a field by a straight edge, is a convenient platform for the study of Argand-plane maps, having already been somewhat generalized by Morgan *et al.* [2]. Mirroring the work of Petersen *et al.* [21], we have looked beyond the straight edge to explore phase shifts imposed on a field by cylindrical and spherical objects, which manifest as generalized Cornu spirals in the Argand plane. The evolution of the Cornu spiral from a one-dimensional trace (albeit embedded in a two-dimensional plane) for a straight edge to the fully-realized two-dimensional Argand-plane map is in our view an interesting tool that is worthy of further investigation in the future.

5. Conclusion

We have presented a study of generalised Cornu spirals, which are a series of Argand-plane mappings of monochromatic wavefields that are incident upon objects with varying degrees of complexity. Here we have focused on a hierarchy of three objects: a straight edge, a cylinder and a sphere embedded within a cylinder. Each object was imaged using propagation-based phase contrast imaging with hard x-rays. After phase retrieval, generalised Cornu spirals were then constructed for each object.

Acknowledgments

FR acknowledges the assistance of Genevieve A. Buckley, Katie L. Lee and Rhiannon P. Murrie in obtaining the images used here. FR also thanks Dr. Kaye S. Morgan for useful discussions. MJK acknowledges financial support from the Australian Research Council. MJK is an Australian Research Fellow (DP110101941).

Chapter 5

Future work

There are numerous possible future applications of the work presented in this thesis, and here I outline a few applications.

With regards to the study of Argand-mappings induced by vortical fields, particularly the presence of vorticity singularities, a natural extension would be to continue this exploration to a greater hierarchy of vorticity singularities. So far, the fold and cusp vorticity singularities have been described and attributed to vorticity singularity lines lying between various combinations of vortices and antivortices, exemplified by the experimental study of Chapter 3. The elliptic umbilic vorticity singularity was reconstructed and linked to the presence of vorticity singularities in the form of a Jacobian ellipse, but no physical explanation was provided. Future work would involve continuing to experimentally observe the possible infinite hierarchy of vorticity singularities, connecting each to some unique formation of singularity lines in the physical field and investigation their physical significance. Such work may improve our understanding of the vorticity in the context of a complex scalar wavefield littered with optical vortices.

The study of vorticity singularities has the potential to go beyond complex scalar wavefields to more general wavefields, such a partially coherent fields, which are described by multi-dimensional coherence functions. Furthermore, a study of vorticity singularities in the context of spinor fields, which are described by multiple complex wavefields, would extend this work to fields that possess multiple sets of singularity lines.

The experimental set-up described in Chapter 3 for reconstructing vorticity singularities could provide a context for the study of topological reactions associated with time-varying fields, such as vortex-antivortex annihilation and saddle points. The Argand plane could also be used to study various fields with topological defects, such as Bose-Einstein condensates, which are naturally vortical two-dimensional objects that change over time.

The study of visible-light speckle fields featured in Chapters 2 and 3 could be extended into x-ray speckle, which has multiple interesting and important applications. Garson et al. (2013) generated a speckle field in an x-ray phase contrast image (PCI) of animal lungs using a bench-top imaging system. The study of lung x-ray speckle is particularly interesting due to its ability to provide further understanding about the structure of lungs. For example, Leong et al. (2014) have shown a method of measuring alveolar size and Kitchen et al. (2015) have shown that lung speckle patterns can be used to measure the dimensions of lung airways. Extending the work described in Chapter 4 by replacing the geometric objects with lung samples may have ramifications in the study of lungs, which are, in essence, cylindrical cavities containing thousands of air-filled spheres. It is not presently clear whether speckle is simply a geometrical phenomenon or whether it is a wave phenomenon. Simulations by Kitchen et al. (2015) show wave behaviour resulting in optical vortices, but their experimental reconstructions, specifically phase retrieval, are based on the geometrical approximation of light. Studying the Argand-plane mappings induced by an optical speckle field, and its associated vorticity singularities, could help clarify the essence of such a field and improve reconstruction procedures.

Chapter 6

Conclusion

In this thesis, I have presented a study of Argand-plane mappings induced by complex scalar wavefields, reported over three separate bodies of published papers as first author. The first publication is a theoretical study of a two-dimensional optical speckle fields littered with vortices. The Argand-plane mappings induced by those wavefields revealed caustic-like Argand-plane singularities that were shown to be a results of lines of zero vorticity in the physical field, proving the Argand-plane to be an interesting domain for the study of such fields. The second publication presents a study that is exemplified by an experimental validation of that theoretical work, utilising visible light. Various vorticity singularities were successfully reconstructed, namely the fold, cusp and elliptic umbilic vorticity singularities, and connected to lines of zero vorticity in the physical field. Moving beyond visible light, the third publication presents a study that is focused on x-ray fields, studying the Argand-plane mappings induced by propagation-based x-ray phase contrast images. Various objects with increasing spatial complexity were imaged - a straight edge, a cylinder, and a sphere embedded within a cylinder. The diffraction of the incident radiation upon coming into contact with these objects resulted in generalised Cornu spirals present in the induced Argand-plane mappings. Through these bodies of published work, the usefulness of the Argand-plane in the analysis of two-dimensional complex scalar wavefields was made apparent. There are numerous possible extensions to this work, such as the study of x-ray lung speckle and the analysis of time-varying fields.

Bibliography

- Aksenov, V., V. Banakh, and O. Tikhomirova (1998). Potential and vortex features of optical speckle fields and visualization of wave-front singularities. *Appl. Opt.* **37**, 4536–4540.
- Ali, J. (1995). “Geometric control of planar curves”. PhD thesis. University of Birmingham, School of Manufacturing and Mechanical Engineering.
- Ali, J. M., R. M. Tookey, J. V. Ball, and A. A. Ball (1999). The generalised Cornu spiral and its application to span generation. *J. Comp. Appl. Math.* **102**, 37–47.
- Allen, L., M. W. Beijersbergen, R. J. C. Spreeuw, and J. P. Woerdman (1992). Orbital angular momentum of light and the transformation of Laguerre-Gaussian laser modes. *Phys. Rev. A* **45**, 8185.
- Allen, L. J., M. P. Oxley, and D. M. Paganin (2001a). Computational aberration correction for an arbitrary linear imaging system. *Phys. Rev. Lett.* **87**, 123902.
- Allen, L. J., H. M. L. Faulkner, M. P. Oxley, and D. M. Paganin (2001b). Phase retrieval and aberration correction in the presence of vortices in high-resolution transmission electron microscopy. *Ultramicroscopy* **88**, 85–97.
- Anton, H. and C. Rorres (2005). “Euclidean vector spaces”. In: *Elementary linear algebra*. 9th. NJ: Wiley, pp. 181–209.
- Bazhenov, V. Yu., M. V. Vasnetsov, and M. S. Soskin (1990). Laser beams with screw dislocations in their wavefronts. *JETP Lett.* **52**, 429–431.
- Bedrosian, E. (1962). The analytic signal representation of modulated waveforms. *Proc. IRE* **50**, 2071–2076.
- Beijersbergen, M. W., L. Allen, H. E. L. O. Van der Veen, and J. P. Woerdman (1993). Astigmatic laser mode converters and transfer of orbital angular momentum. *Opt. Commun.* **96**, 123–132.

- Beijersbergen, M. W., R. P. C. Coerwinkel, M. Kristensen, and J. P. Woerdman (1994). Helical-wavefront laser beams produced with a spiral phaseplate. *Opt. Commun.* **112**, 321–327.
- Bekshaev, A., O. Orlinska, and M. Vasnetsov (2010). Optical vortex generation with a fork hologram under conditions of high-angle diffraction. *Opt. Commun.* **283**, 2006–2016.
- Bekshaev, A. Ya., A. S. Bekshaev, and K. A. Mohammed (2014). Arrays of optical vortices formed by "fork" holograms. *Ukraine J. Phys. Opt.* **15**, 123–131.
- Beltran, M. A., D. M. Paganin, K. Uesugi, and M. J. Kitchen (2010). 2D and 3D X-ray phase retrieval of multi-material objects using a single defocus distance. *Opt. Exp.* **18**, 6423–6436.
- Berry, M. V. (1981). Singularities in waves and rays. *Phys. Defects* **35**, 453–543.
- Berry, M. V. (2009). Optical currents. *J. Opt. A: Pure Appl. Opt.* **11**, 094001.
- Bobrov, B. D. (1991). Screw dislocations of laser speckle fields in interferograms with a circular line structure. *Soviet J. Quan. Electr.* **21**, 802.
- Boivin, A., J. Dow, and E. Wolf (1967). Energy Flow in the Neighborhood of the Focus of a Coherent Beam. *JOSA* **57**, 1171–1175.
- Born, M. and E. Wolf (1999). *Principles of Optics*. 7th (expanded). Pergamon.
- Bravin, A. (2003). Exploiting the X-ray refraction contrast with an analyser: the state of the art. *J. Phys. D: Appl. Phys.* **36**, A24.
- Cloetens, P., R. Barrett, J. Baruchel, J. P. Guigay, and M. Schlenker (1996). Phase objects in synchrotron radiation hard x-ray imaging. *J. Phys. D: Appl. Phys.* **29**, 133.
- Coan, P., A. Wagner, A. Bravin, P. C. Diemoz, J. Keyriläinen, and J. Mollenhauer (2010). In vivo x-ray phase contrast analyzer-based imaging for longitudinal osteoarthritis studies in guinea pigs. *Phys. Med. Biol.* **55**, 7649.
- Crewe, A. V., D. N. Eggenberger, J. Wall, and L. M. Welter (1968). Electron gun using a field emission source. *Rev. Sci. Instr.* **39**, 576–583.
- Cross, B. and R. J. Cripps (2015). Efficient robust approximation of the generalised Cornu spiral. *J. Comp. Appl. Math.* **273**, 1–12.
- Davis, T. J., D. Gao, T. E. Gureyev, A. W. Stevenson, S. W. Wilkins, et al. (1995a). Phase-contrast imaging of weakly absorbing materials using hard X-rays. *Nature* **373**, 595–598.

- Davis, T. J., T. E. Gureyev, D. Gao, A. W. Stevenson, and S. W. Wilkins (1995b). X-ray image contrast from a simple phase object. *Phys. Rev. Lett.* **74**, 3173.
- Davisson, C. J. and L. H. Germer (1928). Reflections of electrons by a crystal of nickel. *Proc. Natl. Acad. Sci. USA* **14**, 317–322.
- Dennis, M. R., K. O'Holleran, and M. J. Padgett (2009). Singular optics: optical vortices and polarization singularities. *Prog. Optics* **53**, 293–363.
- Diemoz, P. C., A. Bravin, and P. Coan (2012). Theoretical comparison of three X-ray phase-contrast imaging techniques: propagation-based imaging, analyzer-based imaging and grating interferometry. *Opt. Exp.* **20**, 2789–2805.
- Dirac, P. A. M. (1927). The quantum theory of the emission and absorption of radiation. In: *Proceedings of the Royal Society of London A: Mathematical, Physical and Engineering Sciences*. Vol. 114, pp.243–265.
- Doak, R. B., R. E. Grisenti, S. Rehbein, G. Schmahl, J. P. Toennies, and Ch. Wöll (1999). Towards realization of an atomic de Broglie microscope: helium atom focusing using Fresnel zone plates. *Phys. Rev. Lett.* **83**, 4229–4232.
- Donati, O., G. P. Missiroli, and G. Pozzi (1973). An experiment on electron interference. *Am. J. Phys.* **41**, 639–644.
- Evans, W. R. (1948). Graphical analysis of control systems. *Trans. Am. I. Electric. Eng.* **67**, 547–551.
- Evans, W. R. (1950). Control system synthesis by root locus method. *Trans. Am. Inst. Elect. Eng.* **69**, 66–69.
- Faraday, M. (1852). “On the physical character of the lines of magnetic force”. In: *Experimental Researches*. 3 vols. London: Taylor and Francis, pp. 407–437.
- Faulkner, H. M. L., L. J. Allen, M. P. Oxley, and D. M. Paganin (2003). Computational aberration determination and correction. *Opt. Commun.* **216**, 89–98.
- Fienup, J. R. (1982). Phase retrieval algorithms: a comparison. *Appl. Opt.* **21**, 2758–2769.
- Fienup, J. R. (1984). Reconstruction and synthesis applications of an iterative algorithm. In: *Transformations in Optical Signal Processing*. International Society for Optics and Photonics, pp.147–160.
- Förster, E, K Goetz, and P Zaumseil (1980). Double crystal diffractometry for the characterization of targets for laser fusion experiments. *Kristall und Technik* **15**, 937–945.

- Gabor, D. (1946). Theory of communication. Part 1: The analysis of information. *J. Instn. Elect. Engrs.* **93**, 429–441.
- Gao, Y., K. Liu, Z. Sun, L. Guo, and Y. Gan (2015). Beam shaping with vortex beam generated by liquid crystal spatial light modulator. In: *International Symposium on Precision Engineering Measurement and Instrumentation*, pp.94463Z–94463Z.
- Garson, A.B., E. W. Izaguirre, S. G. Price, and M. A. Anastasio (2013). Characterization of speckle in lung images acquired with a benchtop in-line x-ray phase-contrast system. *Phys. Med. Biol.* **58**, 4237.
- Gerchberg, R. W. and W. O. Saxton (1972). A practical algorithm for the determination of phase from image and diffraction plane pictures. *Optik* **35**, 237–246.
- Gilbert, W. (1600). *De Magnete*. translated into English by Brother Arnold (1974, Harvard University Press). London: Peter Short.
- Goodman, J. W. (2005). *Introduction to Fourier optics*. Roberts and Company Publishers.
- Green, H. S. and E. Wolf (1953). A scalar representation of electromagnetic fields. *Proc. Phys. Soc. A* **66**, 1129–1137.
- Guehrs, E., C. M. Günther, R. Könnecke, B. Pfau, and S. Eisebitt (2009). Holographic soft X-ray omni-microscopy of biological specimens. *Opt. Exp.* **17**, 6710–6720.
- Gureyev, T. E. and K. A. Nugent (1996). Phase retrieval with the transport-of-intensity equation. II. Orthogonal series solution for nonuniform illumination. *JOSA A* **13**, 1670–1682.
- Gureyev, T. E. and K. A. Nugent (1997). Rapid quantitative phase imaging using the transport of intensity equation. *Opt. Commun.* **133**, 339–346.
- Gureyev, T. E., D. M. Paganin, G. R. Myers, Ya. I. Nesterets, and S. W. Wilkins (2006). Phase-and-amplitude computer tomography. *App. Phys. Lett.* **89**, 034102.
- Hadamard, J (1923). *Lectures on Cauchy's problem in linear partial differential equations*. New Haven: Yale University Press.
- Hecht, E. (2002). *Optics*. fourth. Addison Wesley.
- Heckenberg, N. R., R. McDuff, C. P. Smith, and A. G. White (1992). Generation of optical phase singularities by computer generated hologram. *Opt. Lett.* **17**, 221–223.
- Herman, G. T. (2009). *Fundamentals of computerized tomography: image reconstruction from projections*. Springer Science & Business Media.

- Hettwer, A., J. Kranz, and J. Schwider (2000). Three channel phase-shifting interferometer using polarization-optics and a diffraction grating. *Opt. Eng.* **39**, 960–966.
- Hitachi, A. (2012). Cornus spiral in the Fresnel regime studied using ultrasound: A phase study. *J. Acoust. Soc. Am.* **131**, 2463–2471.
- Huang, S., C. He, and T. Wang (2014). Generation of sidelobe-free optical vortices utilizing object-oriented computer generated holograms. *J. Opt.* **16**, 035402.
- Ingal, V. N. and E. A. Beliaevskaya (1995). X-ray plane-wave topography observation of the phase contrast from a non-crystalline object. *J. Phys. D: Appl. Phys.* **28**, 2314.
- Janicijevic, L. and S. Topuzoski (2016). Gaussian laser beam transformation into an optical vortex beam by helical lens. *J. Mod. Opt.* **63**, 164–176.
- Kapoor, A., M. Kumar, P. Senthilkumaran, and J. Joseph (2016). Optical vortex array in spatially varying lattice. *Opt. Commun.* **365**, 99–102.
- Karp, S. N. and J. B. Keller (1961). Multiple Diffraction by an Aperture in a Hard Screen. *Optica Acta: Intntl. J. of Opt.* **8**, 61–72.
- Keller, J. B. (1957). Diffraction by an Aperture. *J. Appl. Phys.* **28**, 426–444.
- Keller, J. B. (1959). How Dark is the Shadow of a Round-Ended Screen? *J. Appl. Phys.* **30**, 1452–1454.
- Keller, J. B. (1962). Geometrical Theory of Diffraction. *JOSA* **52**, 116–130.
- Kitchen, M. J., D. M. Paganin, R. A. Lewis, N. Yagi, K. Uesugi, and S. T. Mudie (2004). On the origin of speckle in x-ray phase contrast images of lung tissue. *Phys. Med. Biol.* **49**, 4335.
- Kitchen, M. J., R. A. Lewis, M. J. Morgan, M. J. Wallace, M. L. Siew, K. K. W. Siu, A. Habib, A. Fouras, N. Yagi, K. Uesugi, et al. (2008). Dynamic measures of regional lung air volume using phase contrast x-ray imaging. *Phys. Med. Biol.* **53**, 6065.
- Kitchen, M. J., G. A. Buckley, A. F. T. Leong, R. P. Carnibella, A. Fouras, M. J. Wallace, and S. B. Hooper (2015). X-ray specks: low dose in vivo imaging of lung structure and function. *Phys. Med. Biol.* **60**, 7259.
- Kouyoumjian, R. G., P. H. Pathak, and W. D. Burnside (1981). A uniform GTD for the diffraction by edges, vertices and convex surfaces. *Theoretical Methods for Determining the Interaction of Electromagnetic Waves with Structures*, Ed. JK Skwirzynski.

- Kouznetsov, D. and H. Oberst (2005). Reflection of waves from a ridged surface and the Zeno effect. *Opt. Rev.* **12**, 363–366.
- Kuo, B. C. (1987). 2nd. Prentice Hall PTR.
- Lefevre, H. and M. M. Turpin (1990). *Measuring device for the measurement, in a wide range, of a non-reciprocal phase shift generated in a ring interferometer, and measuring method.* US Patent 4,969,017.
- Leong, Andrew F. T., G. A. Buckley, D. M. Paganin, S. B. Hooper, M. J. Wallace, and M. J. Kitchen (2014). Real-time measurement of alveolar size and population using phase contrast x-ray imaging. *Biomed. Opt. Exp.* **5**, 4024–4038.
- Levy, B. R. and J. B. Keller (1959). Diffraction by a smooth object. *Commun. on Pure and Appl. Math.* **12**, 159–209.
- Li, T. T., H. Li, and L. H. Diao (2008). Cone-beam tomography of propagation-based imaging. *Appl. Phys. Lett.* **93**, 221114.
- Lichte, H., E. Vlk, and K. Scheerschmidt (1992). Electron holography. *Ultramicroscopy* **47**, 231–240.
- Lichte, H., P. Kessler, F. Lenz, and W-D Rau (1993). 0.1 nm information limit with the CM30FEG-special Tbingen. *Ultramicroscopy* **52**, 575–580.
- Lin, Y. C., T. H. Lu, K. F. Huang, and Y. F. Chen (2011). Generation of optical vortex array with transformation of standing-wave Laguerre-Gaussian mode. *Opt. express* **19**, 10293–10303.
- Lo, Y. H., A. R. D. Somervell, and T. H. Barnes (2005). Wavefront measurement with a phase-shifting lateral-shearing Sagnac interferometer operating in broadband light. *Opt. Las. Eng.* **43**, 33–41.
- Lucas, J. D., M. J. O’Doherty, B. F. Cronin, P. K. Marsden, M. A. Lodge, P. H. McKee, and M. A. Smith (1999). Prospective evaluation of soft tissue masses and sarcomas using fluorodeoxyglucose positron emission tomography. *Br. J. Surg.* **86**, 550–556.
- Mandl, F. and G. Shaw (2010). *Quantum Field Theory*. 2nd. West Sussex, UK: Wiley.
- Masi, M., M Mancinelli, P. Bettotti, and L. Pavesi (2012). Light Combining for Interferometric Switching. *Intnl. J. Opt.* **2012**, 130517.
- Maxwell, J. C. (1890). *Scientific papers*. Vol. 1. J. Hermann.

- Mayo, S., T. Davis, T. E. Gureyev, P. Miller, D. M. Paganin, A. Pogany, A. Stevenson, and S. Wilkins (2003). X-ray phase-contrast microscopy and microtomography. *Opt. Exp.* **11**, 2289–2302.
- Messiah, A. (1961). *Quantum mechanics*. 1 and 2 vols. Amsterdam: North-Holland.
- Morgan, K. S. (2011). “Studies in phase contrast x-ray imaging of biological interfaces”. PhD thesis. Monash University.
- Morgan, K. S., K. K. W. Siu, and D. M. Paganin (2010). The projection approximation and edge contrast for x-ray propagation-based phase contrast imaging of a cylindrical edge. *Opt. Exp.* **18**, 9865–9878.
- Neuhäusler, U., G. Schneider, W. Ludwig, M. A. Meyer, E. Zschech, and D. Hambach (2003). X-ray microscopy in Zernike phase contrast mode at 4 keV photon energy with 60 nm resolution. *J. Phys. D: Appl. Phys.* **36**, A79–A82.
- Newton, I. (1962). *Principia*. Vol. 1. Berkley: University of California Press.
- Ng, I., D. M. Paganin, and A. Fouras (2012). Optimization of in-line phase contrast particle image velocimetry using a laboratory x-ray source. *J. Appl. Phys.* **112**, 074701.
- Novak, M., J. Millerd, N. Brock, M. North-Morris, J. Hayes, and J. Wyant (2005). Analysis of a micropolarizer array-based simultaneous phase-shifting interferometer. *Appl. Opt.* **44**, 6861–6868.
- Nye, J. F. (1999). *Natural focusing and fine structures of light: Caustics and wave dislocations*. CRC Press.
- Paganin, D. M. (2006). *Coherent x-ray optics*. NY: Oxford University Press.
- Paganin, D. M. and K. A. Nugent (1998). Noninterferometric phase imaging with partially coherent light. *Phys. Rev. Lett.* **80**, 2586.
- Paganin, D. M., S. C. Mayo, T. E. Gureyev, P. R. Miller, and S. W. Wilkins (2002). Simultaneous phase and amplitude extraction from a single defocused image of a homogeneous object. *J. Microsc.* **206**, 33–40.
- Paganin, D. M., T. E. Gureyev, S. C. Mayo, A. W. Stevenson, Ya. I. Nesterets, and S. W. Wilkins (2004). X-ray omni microscopy. *J. Microsc.* **214**, 315–327.
- Pagot, E., P. Cloetens, S. Fiedler, A. Bravin, P. Coan, J. Baruchel, J. Hartwig, and W. Thomlinson (2003). A method to extract quantitative information in analyzer-based x-ray phase contrast imaging. *Appl. Phys. Lett.* **82**, 3421–3423.

- Pascucci, M., G. Tessier, V. Emiliani, and M. Guillon (2016). Superresolution Imaging of Optical Vortices in a Speckle Pattern. *Phys. Rev. Lett.* **116**, 093904.
- Pathak, P. H. (1982). Uniform geometrical theory of diffraction. In: *26th Annual Technical Symposium*. International Society for Optics and Photonics, pp.47–63.
- Pathak, P. H., G. Carluccio, and M. Albani (2013). The uniform geometrical theory of diffraction and some of its applications. *IEEE Antennas Prog. Mag.* **55**, 41–69.
- Peele, A. G., P. J. McMahon, D. Paterson, C. Q. Tran, A. P. Mancuso, K. A. Nugent, J. P. Hayes, E. Harvey, B. Lai, and I. McNulty (2002). Observation of an x-ray vortex. *Opt. Lett.* **27**, 1752–1754.
- Planck, M. (1900). On the theory of the energy distribution law of the normal spectrum. *Verh. Deut. Phys. Ges.* **2**, 237–245.
- Press, W. H., B. P. Flannery, S. A. Teukolsky, and W. T. Vetterling (1992). *Numerical recipes in FORTRAN*. Cambridge Univ. Press.
- Rayleigh, J. W. S. B. (1871). *On the scattering of light by small particles*.
- Rickenstorff, C. and A. S. Ostrovsky (2013). The perfect vortex and its realization by the liquid crystal spatial light modulator. In: *8th Ibero American Optics Meeting/11th Latin American Meeting on Optics, Lasers, and Applications*. International Society for Optics and Photonics, pp.8785AU–1–8785AU–6.
- Roman, P. (1959). A scalar representation of electromagnetic fields: III. *Proc. Phys. Soc.* **74**, 281.
- Schmahl, G., D. Rudolph, B. Niemann, P. Guttman, G. Schneider, and J. Thieme (1991). X-ray microscopy experiments at the BESSY storage ring. *Synch. Rad. News* **4**, 10–11.
- Schmahl, G., P. Guttman, G. Schneider, B. Niemann, C. David, T. Wilhein, J. Thieme, and D. Rudolph (1994). Phase contrast studies of hydrated specimens with the x-ray microscope at BESSY. *X-Ray Microsc. IV*, 196–206.
- Schot, G. Van Der, M. Svenda, F. R. N. C. Maia, M. Hantke, D. P. DePonte, M. M. Seibert, A. Aquila, J. Schulz, R. Kirian, M. Liang, et al. (2015). Imaging single cells in a beam of live cyanobacteria with an X-ray laser. *Nat. Commun.* **6**, 5704.
- Schreiber, H. and J. H. Bruning (2006). Phase shifting interferometry. *Optical Shop Testing, Third Edition*, 547–666.

- Schuetze, S. M., B. P. Rubin, C. Vernon, D. S. Hawkins, J. D. Bruckner, E. U. Conrad, and J. F. Eary (2005). Use of positron emission tomography in localized extremity soft tissue sarcoma treated with neoadjuvant chemotherapy. *Cancer* **103**, 339–348.
- Serway, R., C. Moses, and C. Moyer (2004). *Modern physics*. 3rd. Cengage Learning.
- Shimizu, F. and J. Fujita (2002). Reflection-type hologram for atoms. *Phys. Rev. Lett.* **88**, 123201.
- Shvartsman, N. and I. Freund (1994). Vortices in random wave fields: nearest neighbor anticorrelations. *Phys. Rev. Lett.* **72**, 1008.
- Silva, M., S. Brandão, M. Parente, T. Mascarenhas, and J. R. M. Natal (2016). Establishing the biomechanical properties of the pelvic soft tissues through an inverse finite element analysis using magnetic resonance imaging. *Proc. Inst. Mech. Eng. H, J. Eng. Med.* **230**, 298–309.
- Somenkov, V. A., A. K. Tkalic, and S. S. Shil'shtein (1991). Refraction contrast in x-ray introscopy. *Sov. Phys. Tech. Phys.* **36**, 1309–1311.
- Staliunas, K., A. Berzanskis, and V. Jarutis (1995). Vortex statistics in optical speckle fields. *Opt. Commun.* **120**, 23–28.
- Teague, M. R. (1983). Deterministic phase retrieval: a Greens function solution. *JOSA* **73**, 1434–1441.
- Thom, R. (1975). *Structural stability and Morphogenesis: An outline of a general theory of models*, trans. DH Fowler. Mass.: Reading.
- Thomson, W. (1851). On the theory of magnetic induction in crystalline and non-crystalline substances. *Philosophica Magazine* **2**, 177–186.
- Vine, D. J., D. M. Paganin, K. M. Pavlov, J. Kraeusslich, O. Wehrhan, I. Uschmann, and E. Förster (2007). Analyzer-based phase contrast imaging and phase retrieval using a rotating anode x-ray source. *Appl. Phys. Lett.* **91**, 254110.
- Vyas, S. and P. Senthilkumaran (2010). Vortices from wavefront tilts. *Optics and Lasers in Engineering* **48**, 834–840.
- Watson, J. J., J. D. Stevenson, P. Cool, G. L. Cribb, J. P. R. Jenkins, M. Leahy, and J. J. Gregory (2016). Whole-body magnetic resonance imaging in myxoid liposarcoma: A useful adjunct for the detection of extra-pulmonary metastatic disease. *Eu. J. Sur. Onc.* **42**, 574–580.

- Wilkins, S. W., T. E. Gureyev, D. Gao, A. Pogany, A. W. Stevenson, et al. (1996). Phase-contrast imaging using polychromatic hard X-rays. *Nature* **384**, 335–338.
- Williamson, S. E. (1969). Accurate root locus plotting including the effects of pure time delay. Computer-program description. *Proc. IEEE* **116**, 1269–1271.
- Wolf, E. (1959). A scalar representation of electromagnetic fields: II. *Proc. Phys. Soc.* **74**, 269–280.
- Xin, J., K. Dai, L. Zhong, Q. Na, and C. Gao (2014). Generation of optical vortices by using spiral phase plates made of polarization dependent devices. *Opt. Lett.* **39**, 1984–1987.
- Yu, P., G. Xue-Tao, J. Pei, W. Ya-Dong, and Z. Jian-Lin (2015). Measuring topological charges of optical vortices with multi-singularity using a cylindrical lens. *Chinese Phys. Lett.* **32**, 024201.
- Zernike, F. (1942). Phase contrast, a new method for the microscopic observation of transparent objects. *Physica* **9**, 686–698.
- Zuo, C., Q. Chen, L. Tian, L. Waller, and A. Asundi (2015). Transport of intensity phase retrieval and computational imaging for partially coherent fields: The phase space perspective. *Opt. Las. Eng.* **71**, 20–32.